Improving Positioning Capabilities for Automated Pipe Inspection

Engineering Doctorate Thesis

A. McGregor

Centre for Ultrasonic Engineering

Electrical and Electronic Engineering

University of Strathclyde, Glasgow

May 4, 2022

Abstract

Industrial pipework requires routine inspection and maintenance to ensure integrity and avoid potentially catastrophic failure. Automated solutions are providing more consistent positioning and mapping capabilities compared to manual inspection, which relies heavily on the ability of the inspector. This Thesis describes a method of positioning probes on a pipe surface considering the system geometry and the output of a 3-axis accelerometer. Positional drift is a common disadvantage in many onboard positioning systems, an advantage of the method developed is the ability to obtain a measure of the position and orientation which is not subject to drift over time. Another key advantage is that the system can be completely placed on the rig or robot holding the probe, negating the need for systems such as cameras or beacons to track the position of the probe.

A general analytical Forward Model which simulates the accelerometer readings at a given position and orientation has been developed. This provides an insight into how the accelerometer readings change as a function of the position, orientation, and system geometry. It also allows for the simulation of ideal accelerometer readings at any combination of position and orientation on a pipe surface. An Inverse Model combined with a numerical optimisation method is then detailed to obtain the position and orientation from the accelerometer readings. This was experimentally validated. These results show a $4.17°$ error in the circumferential angle around the pipe, and a $3.40°$ error in the orientation angle for a pipe diameter of 502mm. Error analysis detailing how the error in ovality and pitch of the pipe and error in accelerometer readings affects the optimisation was carried out. An Extended Kalman Filter was designed

to incorporate this novel positioning method. Simulations fusing the sensor output from a combination of wheel encoders, indoor positioning systems and accelerometers show that fusing this novel method of processing accelerometer data provides an 57.5% increase in accuracy compared to dead reckoning using encoders. This work is being commercialised by the engineering team at the industrial partner Eddyfi Technologies, where work is being done to build on and implement the outcomes of this research into a range of its product lines.

Contents

List of Figures

xii

List of Tables

Acknowledgements

Chapter 1

Introduction

Methods of automating repetitive tasks are increasingly being explored and implemented in industry. Robotics and automation are examples of this and are being employed to help make tasks easier, more efficient, quicker, more consistent and more cost effective [**james˙smarter˙2012**]. These advances can be found in homes, warehouses, agriculture and are increasingly deployed in industrial settings to aid with engineering challenges. In industrial settings, automation can be used to compliment people in their day to day work by helping them complete repetitive tasks [1]. Robots can also be employed to complete tasks which would be considered dangerous or not easily completed, such as exploration or decommissioning of radioactive sites [2], hazardous areas [3], the rail industry [4], and even in space [5].

A task where automation is being increasingly considered is for the inspection of critical assets to assess remaining lifespan and determine if an asset is in need of maintenance or repair. Properly determining and recording the location of an inspection measurement is paramount for accurate and meaningful inspection, and is not considered a trivial task [6, 7]. Without this, monitoring of a defect over time and applying a suitable repair become less meaningful and less cost effective. Inaccurate positioning can also lead to errors in sizing of defects and reduce the reliability of inspection [8]. One type of asset which needs to be inspected on a regular basis on many different industrial sites

are pipes. These can be safety and production critical assets which need to function in order to protect the safety of people and the environment, while also ensuring that a plant remains operational for commercial purposes. This thesis aims to improve positioning capabilities for inspection of pipe assets using commercially viable means for both manual and robotic inspection. This is achieved using an onboard sensor to obtain the position and orientation of an inspection probe on the surface of a pipe.

1.1 Non-Destructive Evaluation

In industrial settings, such as electric power systems, petrochemical sites or nuclear facilities, assets are subject to several mechanisms which affect their structural health. Examples of these include corrosion of metal surfaces, cracks forming in welds or delamination on composite wind turbine blades. These structural flaws or defects can cause catastrophic failure of the asset and may result in asset downtime, revenue loss and in some cases loss of human life. For these reasons it is essential that inspection of these assets be carried out at regular intervals to find defects and monitor them in order to determine an appropriate repair to prevent failures, monitor defect growth and predict remaining asset life. This process is known as NDE (Non-Destructive Evaluation), sometimes also referred to as NDT (Non-Destructive Testing). There are a number of different techniques which are used for NDE purposes. These include Ultrasonic Testing (UT) and (PEC) Pulsed Eddy Current, where a probe is used to send and receive signals which are then processed to give information of the structure of the inspected material. The scans can be represented in a number of ways, ranging from a single A scan or spot measurement which can give the thickness reading at a single point, a B-scan which gives the thickness reading over a line, a C-scan, which is a thickness map over a 2D area and a D-scan, which shows the cross-section perpendicular to the scanning surface. Inspections can be performed manually, where an inspector moves the sensor by hand, or automatically by a scanner. In some cases, large areas of magnitude greater than $100m^2$ may need to be inspected with millimetre accuracy to create accurate defect maps and correctly size defects [9] [10]. This can lead to positioning errors due to inspector fatigue and operator bias [singh˙three˙2000].

Usually, assets are inspected multiple times throughout their life cycle to monitor any defects and their growth. This requires accurate defect maps to be created with each inspection to allow engineers to determine if the growth rate and size of a defect is acceptable. There can be large areas that need to be covered in a single inspection and doing so in a consistent manner over multiple inspections with potentially years separating each inspection. All of these factors can lead to human errors in positioning and operator fatigue can lead to incomplete coverage which can result in failure of an asset which can pose health and safety risks, environmental damage and lost revenue for the asset owners. Therefore, increasing the positional accuracy of inspections a vital prerequisite for ensuring that defects are mapped accurately and consistently over sequential inspections.

1.2   Localisation of NDE Sensors

Positioning of probes for NDE is important as it allows for accurate maps of defects to be constructed. Probes can be positioned on surfaces manually by human inspectors, however, as mentioned above, there are many drawbacks to this. Another alternative to positioning a probe by hand is to use a robotic system. This can increase the repeatability of the inspection and removes many of the drawbacks associated with human inspectors.

Even though robot positioning is a broad and widely researched topic, there are still many difficulties associated with the implementation of mobile robotic solutions in various industries and applications. One of the main challenges faced by mobile robotics is accurate position and orientation estimation [11], commonly referred to as pose. Accurate positioning is critical for reliable robot navigation and for placement of NDE sensors in general. Position and orientation can be measured using a range of sensors. These sensors are subject to inherent errors and uncertainties that can compound over time which leads to inaccurate localisation. Fusion of local sensory data, such as odometry data (data taken from wheel encoders) and global positioning measurements (such as Global Positioning System (GPS) [12]), through approaches

such as probabilistic filters, can enhance the position estimation and have been widely investigated in previous works. This is mainly for applications in open spaces where GPS is easily accessible, for example in the agricultural robotics space [13], or open air mining applications [14]. For many NDE applications GPS is not sufficient due to its large inaccuracies, which at any given time could be in the meter range. GPS is not available on many industrial sites due to large structures obstructing the signal, or being located underground where GPS signals do not penetrate. In these 'GPS-denied' areas other sensing means are needed to ascertain a fixed reference frame where intricate positional measurements can be referenced from.

Position and orientation measurements can be used either in real time or post processing. This information can be used in real time for better dynamic control of the system. In post processing applications position and orientation information can be used to create a map of where the robot has travelled. An example of a robot using real time processing is a robot using path finding algorithms to determine where to go. Post processing can be used to determine where the robot has been and can be used to compare the ideal robot path to the actual robot path. Examples of mobile robots being used in industry include agricultural robots, which usually employ GPS to navigate in large open fields to harvest crops [13]. The positional accuracy required for these applications can be in the meter range. Another example of global positioning system being used for robots used to transport goods in warehouses [15]. These warehouses have local positioning systems set up on site which can include indoor GPS systems such as Ultra-Wide Band (UWB) systems, or strategically placed QR (Quick Response) codes that can be scanned by a robot's vision system to identify their current location. Unfortunately, for mobile NDE applications, neither of these methods on their own are suitable for NDE inspection purposes.

There are two main kinds of measurement types in mobile robotics, relative and absolute measurements. Relative measurements rely on previous states to determine the current position of the robot. An example of this is counting wheel rotations using encoders. Relative measurements are subject to integral error which increases with time. This

4

integral error is a result of the inherent uncertainty with each encoder measurement compounding but can also be a result of wheel or encoder slippage not being taken into account while moving. Absolute measurements, such as GPS, are a measure of the position regardless of any historical information and therefore do not have integral error associated with them.

Local absolute positioning systems exist which can accurately measure the position and orientation of an object in 3D space with millimetre accuracy, such as photogrammetry [16] and LiDAR systems [17]. These measure absolute position in a "global" reference frame, as opposed to a relative robotic reference frame, which means that the error associated with the measurement does not increase with time. They are usually placed external from the robot, require extra site preparation where the tracking needs to take place, training for people operating the system and are costly. Practically, these can be difficult to deploy, require significant training and long set-up times. These systems also typically require line of sight of the object being tracked, which becomes an issue when attempting to achieve full coverage of an asset such as a pipe where there are areas out of line-of-sight, such as the underside of the pipe.

An alternative to using external sensors is to use onboard sensors where there is no external equipment required. This reduces the amount of work needed to setup and prepare the an environment. One of the main disadvantages of onboard sensors is that they tend to use relative measurements and therefore have time integral error. This becomes a significant problem for continuous periods of inspection using a mobile or autonomous system as the positioning error will become greater over time [18]. One common type of onboard sensor which is becoming more prevalent in mobile robotics is an Inertial Measurement Unit (IMU), typically consisting of an accelerometer to measure the force of acceleration, a gyroscope to measure the change in orientation and a magnetometer to measure the heading. IMUs have been utilized in other robotic research to obtain more accurate position and orientation measurements with the aim of making systems more autonomous [19, 20, 21, 22]

A common practice in mobile robotic positioning is to use measurements from multiple sources to acquire a better positional estimate compared to using a single source, this is known as sensor fusion. A widely used fusion method in robotics is an extension to the probabilistic Bayesian Filter, known as the Kalman Filter [23]. Sensor fusion can help systems maintain more accurate pose estimates, which is seen as a vital part of autonomous robotic systems.

1.3   Automated Non-Destructive Evaluation

Automated inspection with robotics is playing an increased role in industry as automation can increase the inspection speed, decrease risk to operator health and safety and can have financial benefits in terms of reduced training and site preparation costs [24]. The use of mobile robotics is becoming increasingly prevalent due the remote on-site inspection requirements to evaluate fitness for service of assets [25]. Automation of NDE can improve overall accuracy by reducing human error, which can be categorised as a weak point in the NDE process [26]. This has been helped by the availability and reducing in size of electrical components and MEMS (Micro-Electrical-Mechanical Systems) [27]. This increase in use and interest in robotics for the inspection field is due to greater working loads as a result of higher operational demands and longer expected asset life cycles [28]. There is also the reduced exposure of personnel to confined spaced. These are considered hazardous as they are not designed as areas for people to work [29].

There are many kinds of mobile robotic crawlers. This thesis concentrates on 3-wheeled differential drive robots for automated inspection. Using automation can allow the inspection process to be conducted in a repeatable manner which can aid with defect monitoring over time. In many NDE procedures there is a need to deploy systems and sensors to remote locations with accuracies in the mm range to precisely size defects and to accurately map an asset. It can also increase probability of detection and accuracy of defect localisation while omitting the disadvantages associated with human operators, such as fatigue and variation in operator experience and training. Therefore,

repeatability and increased safety are two advantages to employing mobile robotics for NDE.

Preparing a site for inspection using human operators can require a longer period and more resources to ensure that the site meets health, safety and environment (HSE) regulations [30]. In some industries there are many guidelines in place to protect inspectors from hazards which inevitably increases the cost of inspection as training and preparation costs increase. Often, manual inspection requires scaffolding with operators handling heavy equipment and tools, or the site will require isolation for safety reasons [31]. This poses an HSE risk and requires necessary training and site preparation. Using a portable robot can remove the need for this extra site preparation, therefore reducing personnel training, time, and costs. Using an automated system can also increase precision and accuracy of defect localisation and increase probability of detection (POD) while omitting the typical disadvantages associated with human operator inconsistencies [**singh˙three˙2000**].

1.4 Inspection of Pipes in Industry

Pipes are commonly inspected in the petrochemical industry for corrosion or erosion defects. On any given site there could be hundreds of kilometres of pipes which need to be inspected or monitored. Locating and sizing defects in pipes allows asset owners to maximise the lifetime of the pipe while removing the need for unnecessary repairs and downtime. Accuracy and precision of defect localisation is critical as it can reduce the overall time taken for the maintenance process by increasing repair accuracy and ascertaining the correct location for monitoring defect growth through subsequent pipe inspections. Accurate corrosion rate estimation for pipe defects allows engineers to more accurately carry out fitness for service assessments, extending equipment run time between shutdowns and ultimately increasing equipment life cycles.

It is possible to inspect a pipe from the inside or the outside. Internal inspection can require pipes to be isolated, emptied and cleaned which increases total inspection time.

PIGs (Pipe Inspection Gauges) are another option for in pipe inspection, however this is expensive and positioning accuracy can vary. External pipe inspection can be quicker, however there are other challenges, including inspection of areas under supports and saddle welds [32]. This thesis concentrates on external inspection of pipes.

1.5   Project Sponsor

Eddyfi Technologies is the industrial sponsor of this Engineering Doctorate who develop and integrate various NDE sensors into portable manual and robotic inspection equipment. They offer several NDE instruments, sensors, software and robotic solutions for the inspection of critical components and assets in key industries. The main industries which are covered by Eddyfi products and services include aerospace, oil & gas and power generation. Eddyfi Technologies are at the forefront of robotic integration in NDE inspection, as well as supplying manual hand held probes for various inspection needs, such as Pulsed Eddy Current (PEC) and Ultrasonic wheel probes. This research was conducted in collaboration with Eddyfi Technologies and their Silverwing brand, who developed the Magnetic Flux Leakage (MFL) technique to detect corrosion under the floor of liquid storage tanks. The brand also hosts several automated and robotic solutions including the RMS and Scorpion platforms for Ultrasonic Testing (UT) inspection as well as the Floormap for MFL inspection.

1.6   Aims and Objectives

Previous research and industrial work in NDE have highlighted the constraints of using automated solutions in an indoor or industrial setting [33, 34, 22]. Current solutions to localisation challenges do exist, for example, photogrammetry and LiDAR systems for sub millimetre absolute position measurement and tracking for both hand held probe and robotic applications. However, there is little commercial justification for using such solutions in many industrial settings. This is mainly due to the high cost, from $£5K - £150K$, and impracticality of setting up the systems, particularly in a remote and hostile environment. Photogrammetry systems tend to require long set up times

and calibration procedures which make it unfeasible as moving the setup to another inspection area is very time consuming. As mentioned, absolute measurement systems tend to require external beacons to be set up, limiting their use in industry. Therefore, using an onboard sensor which gives an absolute measure of the position and orientation while remaining commercially viable is a sought-after objective within the industry.

One aim of this work includes the development of a low-cost on-board system to quickly and accurately measure real time location and orientation on pipework with minimal input from the inspector. The key requirements are listed below:

- **Pipe and Probe Geometry Constraints:** The solution should be able to inspect a range of pipe diameters from $100mm - 800mm$ as specified by Eddyfi Technologies. The solution should be able to be incorporated into miniature robotic crawlers and should only require slight modification to the existing Eddyfi Technologies hand held probe range.

- **Location and Orientation Information:** The solution must provide a measure of the location on the pipe as well as the orientation of the sensor on the cylindrical surface.

- **Low Cost:** The solution must be viable from a business perspective. A solution should not add significant cost to the overall platform, with a viable solution costing less than £500.

- **Onboard:** The solution should be on-board to avoid increasing setup and usage time of a product. This will also ensure that transport cost and total setup time are kept to a minimum.

- **Quickly and Accurately:** The position measurements should be quick enough so that they can be used for real time localisation and accurate enough to be a viable positioning system. An accuracy of below 5° error for the circumferential angle and the orientation angle of the robot on the pipe was deemed acceptable

by Eddyfi Technologies.

- **Minimal Inspector Work:** Having minimal inspector work will reduce human error and save time in the inspection process.

  The onboard device that was used in this research was an Inertial Measurement Unit (IMU), more specifically an accelerometer. This was chosen over other onboard sensors, such as a camera, due to the nature use cases for Eddyfi products which are discussed further in the thesis.

1.7 Contributions

The contributions made in this thesis focus on finding an economically feasible solution to obtain absolute measures of position and orientation of a sensor on pipework in on-site industrial setting with minimal inspector input. One use for the work developed is for automatic positioning for manual hand held probes, removing the need for manual marking out the inspection area, such as gridding. This method is also suitable for mobile robotic positioning.

As a result of this research a positioning system has been developed which uses only knowledge of the robot geometry, pipe radius and the output of an onboard accelerometer. This can be further broken down to contributions to the research field of automation in the context of NDE as follows:

- **Accelerometer Forward Model:** A mathematical model to simulate the 3-axis accelerometer readings of an accelerometer placed on a 3-point-of-contact probe, given an initial position and orientation, has been developed. The model allows for the accurate simulation of the accelerometer readings for any given combination of position and orientation on a pipe surface for a 3-point-of-contact device.

- **Optimised Inverse Model:** An inverse model consisting of an analytical approximation

followed by a least-means squared optimisation method to take 3-axis accelerometer readings and estimate the position and orientation of a 3-wheeled robot on a pipe surface has been created. The model allows for an absolute measure of the position and orientation using only an onboard sensor and knowledge of the system geometry. This novel use of an accelerometer proves that it is possible and commercially viable to use an onboard sensor to measure the absolute state of the robot.

- **Model Error Analysis:** An in-depth error analysis of the solution has been conducted to show how discrepancies between the ideal model created and real-world conditions affect the output of the optimised solution. The analysis covers the effects of the ovality of the pipe, error in each of the 3 accelerometer sensor axes and how error in the assumption that the pipe is perfectly horizontal introduce inaccuracy in the model.

- **Probabilistic Sensor Fusion Filter Design:** Custom Extended Kalman Filters (EKF) have been designed using the output of the optimised inverse model to combine different sensor inputs, including encoder, ultra-wide band (UWB) and the angles calculated from accelerometer outputs, to overcome incremental dead reckoning error over time when compared to using a single relative sensor. This further increases the accuracy and reliability of the measurements obtained though the optimised inverse model mentioned above. Simulations show a 57.5% increase in positional accuracy when compared to just using encoders for a single revolution around a pipe circumference.

These contributions show the development of a method for probe positioning which has a relatively low cost and can quickly determine the position and orientation of a sensor on a pipe surface with minimal inspector work. The models and methods developed only require the 3-axis readings of an accelerometer and knowledge of the system geometry to obtain an absolute measurement. Simulations show this absolute measurement can then be further enhanced using a probabilistic sensor fusion algorithm

with already established measurement methods such as wheel encoder values or indoor GPS. A flow diagram illustrating how the contributions in this thesis are linked together are shown in Figure 1.1. At the time of writing, Eddyfi Technologies is in the process of commercialising this research. There are efforts to further integrate the work conducted during this EngD into multiple product lines, with prototypes and proof of concept being tested.
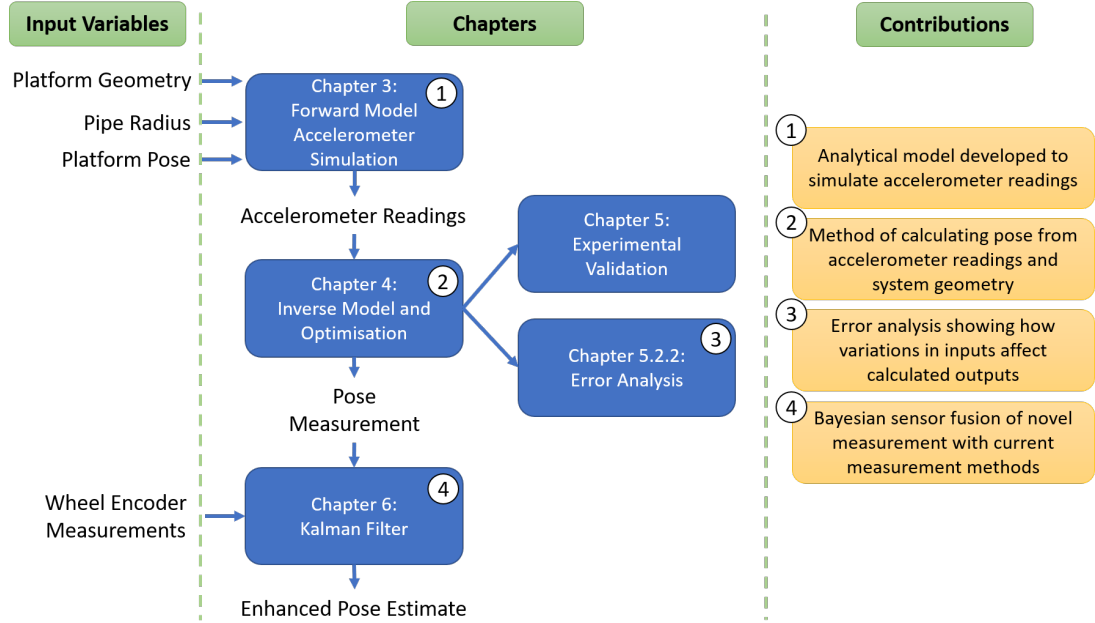
Figure 1.1: Flow diagram relating thesis chapters and contributions

1.8 Thesis Structure

This thesis is structured as follows:

- Chapter 2 - Background: This chapter describes the challenge in depth and reviews relevant work in the field of robotics for NDE as well as explores current industrial solutions for semi-automated and automated inspection of assets, focusing on pipes.

- Chapter 3 - Mathematical Forward Model: This chapter discusses the mathematical

analytical model used to simulate the 3-axis accelerometer readings.

- Chapter 4 - Inverse Model and Optimisation: The Inverse Model and Optimisation work takes the accelerometer readings and determines the position and orientation angle of the robot. This chapter describes these methods as well as the limitations and use cases.

- Chapter 5 - Experimental Setup and Validation: The experimental setup and validation procedures of the work carried out in the previous chapters is presented. This includes the calibration of the relevant equipment and the results of the solution.

- Chapter 6 - Kalman Filter: This chapter illustrates how the values calculated in the previous chapters can be fused with existing methods of measurements to obtain a more accurate estimate of the position and orientation of a robot over time.

- Chapter 7 - Productisation at Eddyfi Technologies: A summary of the productisation of this work currently being undertaken by engineers at Eddyfi Technologies is presented as well as an overview of how Eddyfi is planning on commercialising this research.

- Chapter 8 - Conclusion and Future Work: A summary of the work and its potential applications in industry. Future streams of research based on the output of this thesis are also presented.

1.9   Publication Arising from this Thesis

A. McGregor, G. Dobie, N. Pearson, C. Macleod, and A. Gachagan "Mobile Robot Positioning Using Accelerometers for Pipe Inspection", 45th Annual Review of Progress in Quantitative Non-Destructive Evaluation, Vermont, 2019.

A. McGregor, G. Dobie, N. R. Pearson, C. N. MacLeod and A. Gachagan, "Determining

Position and Orientation of a 3-Wheel Robot on a Pipe Using an Accelerometer" in IEEE Sensors Journal, vol. 20, no. 9, pp. 5061-5071, 1 May1, 2020.

Chapter 2

Background

2.1 Pipe Inspection

Pipe inspection is essential in many industries such as the water, energy and petrochemicals industries [34, 35, 36]. Pipes are critical components and their failure can cause catastrophic damage to both assets and human safety, therefore, their integrity must be monitored and inspected regularly [37]. Pipes are considered to be one of the most important assets that need to be inspected [30].

Pipes can have a variety of geometries, diameters, lengths and also produced from different materials. Here we focus on ferrous materials to allow the robotic crawler to utilise magnetic adhesion to traverse around pipes. They can also be situated underground and be considered inaccessible, or be above ground and accessible. Being accessible generally means that the pipe can be inspected from the outside, whereas underground pipes tend to be inspected from the inside. The positioning method developed here can be used for localisation from both the inside and outside of a pipe, however the focus has been on external inspection. Figure 2.1 show a typical horizontal pipe being inspected from the outside using a hand held probe.

Figure 2.1: Image showing manual inspection of a horizontal pipe[1]

Complex geometries of pipes also present inspection challenges. Common examples of these are saddle welds (Figure 2.2) and pipe supports (Figure 2.3). Assets such as these still need to be inspected to ensure they are safe, and are areas which tend to have corrosion and crack development. Possible pipe inspection methods are discussed below.

---

[1]Eddyfi Technologies: eddyfi.com/en/industry/pipeline-integrity-solutions
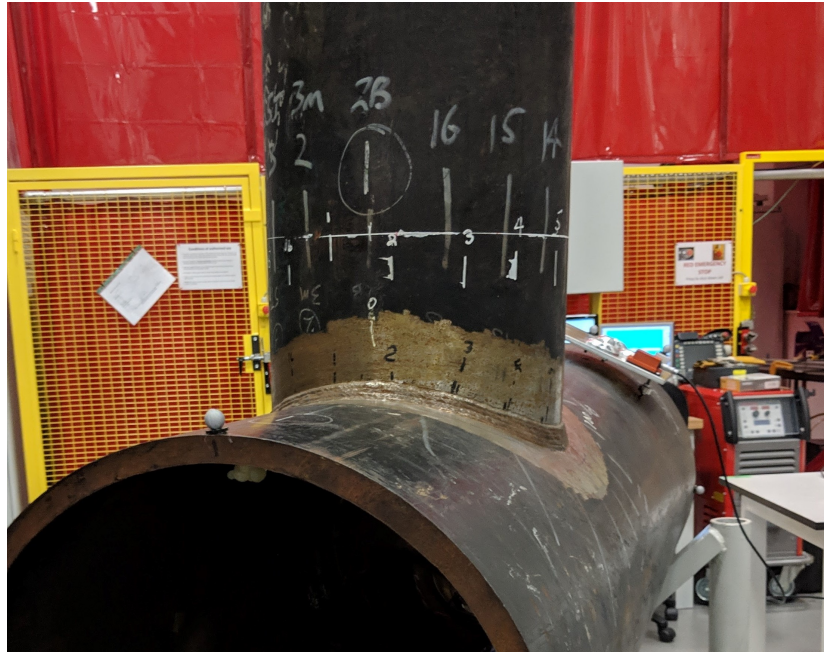
Figure 2.2: Example of saddle weld

Figure 2.3: Example of corrosion at pipe supports[2]

---

[2]Deepwater: stoprust.com

2.1.1 NDE Inspection Methods

Formation of the defects reduces the integrity of the material and can reduce the service life of the asset [38]. These defects can lead to failure of the pipe, especially when the pipe is transporting high pressure mediums, and loss of product though leaks. An example of corrosion is shown in Figure 2.4 and an example of the different potential corrosion defects are shown in Figure 2.6. The different crack defects which need to be monitored are shown in Figure 2.5. These issues need to be addressed for safety and commercial reasons. In some industries, an small amount of corrosion or cracking is acceptable, however the growth of these defects needs to be observed over time to determine when and if they become a risk to the assets integrity.

Figure 2.4: Example of corrosion on a pipe at a saddle weld[3]

---

[3]Coolabah Water: coolabahwater.com.au/stop-pipe-corrosion

Figure 2.5: Example of different types of crack on a pipe[4]
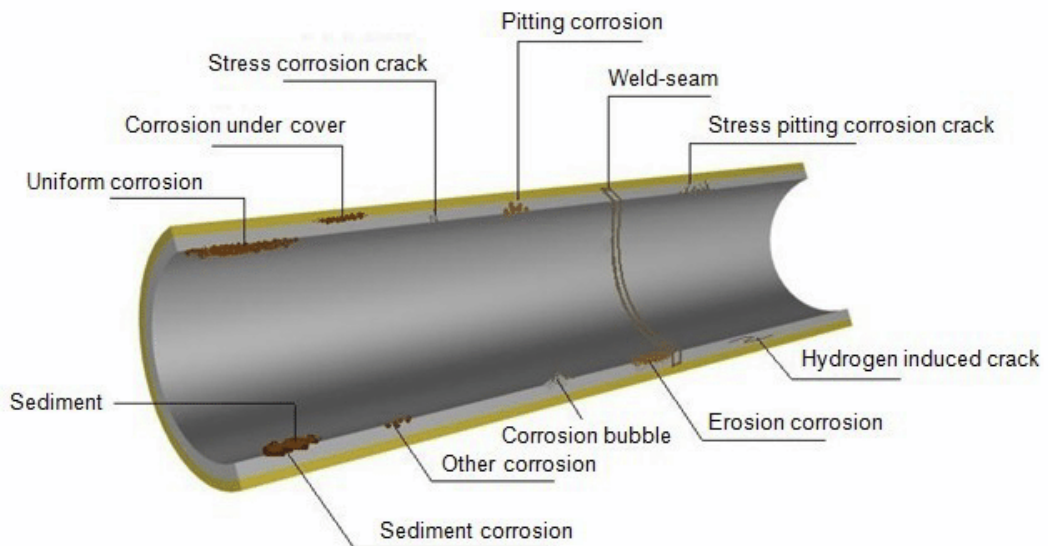
Figure 2.6: Example of different types of corrosion on a pipe [39]

One of the most common methods of pipe inspection is visual inspection. This can be achieved by inserting a camera into the pipe and looking for defects. There are many systems available for this depending on size of the entrance cavity and the inner

---

[4]Rosen Group: rosen-group.com/global/solutions/services/pipeline-cracks

diameter of the pipe. Manual video scopes, such as the Olympus IPLEX NX[5] are flexible and can provide a clear view of the state of the inside of the pipe, however localisation is limited. For larger openings Eddyfi Technologies, through their Inuktun brand, offers a wide range of robotic platforms for increased manoeuvrability. These are mainly the Veratrax 50, 100 and 150 models for visual inspection, which are discussed in more detail in Section 2.4.2. However, visual inspection does not quantify the degree of degradation and is therefore mostly used as a screening method. Other inspection methods are then required to determine the extent of the defect, such as Eddy Current (EC) or Ultrasonic Testing (UT).

Another screening method used for the detection of wall thickness loss is Pulsed Eddy Current (PEC). This is usually done with a handheld probe operated by an inspector. The inspector follows a grid pattern which is typically drawn on the asset to try and achieve good coverage in order to create a wall loss map. This is also a screening method, usually a quicker inspection to find areas which may be of interest, and when significant wall loss is detected, further inspection is necessary. An example setup from Eddyfi for this method is shown in Figure 2.15.

Phased Array Ultrasonic Testing (PAUT) is usually used once an area of interest has been determined (such as around welds) as it is comparatively more time consuming compared to screening methods. Manual inspection involves pushing a probe, sometimes with the aid of encoders to create a map of the inspection area.

Inspection methods for pipes structures and pipelines are dependant on many factors. These factors include;

- Material: Some materials are less suitable for certain inspection methods due to the materials physical properties. For example, stainless steel or titanium alloys can be difficult to inspect with ultrasound due to the noise generated by the grain structure [40].

---

[5]Olympus: www.olympus-ims.com

- Defect detection: Inspection methods are not suitable for all defect types. For example, Magnetic Particle Inspection (MPI) and Dye Penetrant Testing are mostly suitable for surface breaking defects.

- Insulation or coating: If coating or insulation can not be removed, methods such as ultrasound which need to be in contact with the surface are not viable.

Figure 2.7 shows an example of a corrosion map using PAUT data showing isolated corrosion on a pipe. One of the requirements for automated and semi-automated NDE is to obtain a map similar to this which accurately represents the real conditions so that defects can be sized and monitored precisely and accurately.
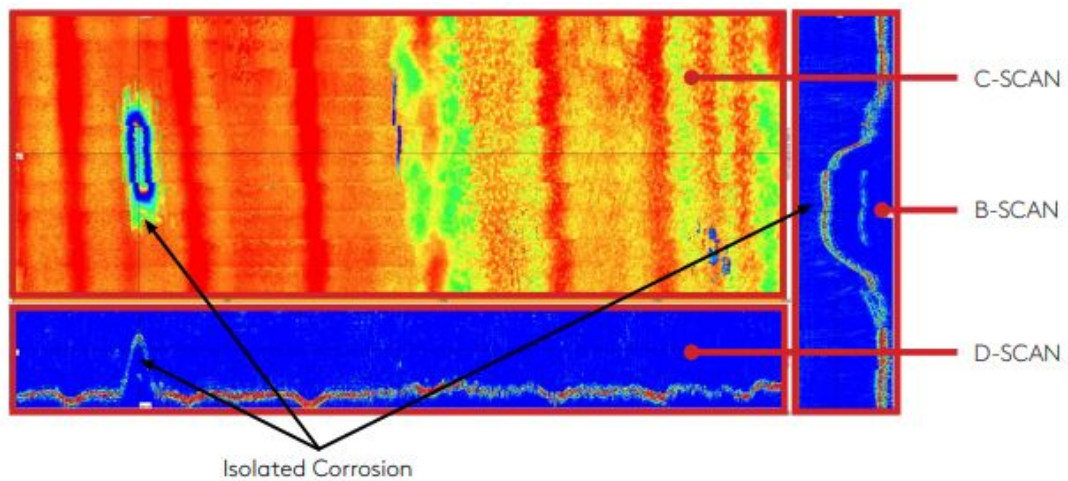
Figure 2.7: Example corrosion map[6]showing the multiple different kinds of scans indicating an isolated corrosion defect

2.1.2 Typical Automated Pipe Inspection

Manual inspection of pipes and pipelines can be time consuming, hazardous and operator bias and fatigue can play a role in inaccurately mapping defects. A common automated solution for inspection of pipelines are Pipe Inspection Gauges (PIGs) [37]. PIGs usually rely on the flow of the fluid inside the pipe to propel themselves forward and

---

[6]Eddyfi technologies: www.eddyfi.com/doc/Pdf/NII-Non-Intrusive-Inspection-Vessel-Pipework-01.pdf

are usually used for corrosion mapping. They are typically used for inspection of long sections of pipeline in the km range. PIGs can be equipped with different sensing capabilities, including ultrasonic guided waves [41], ultrasound [42], or magnetic flux leakage [43]. An example of a PIG is shown in Figure 2.8
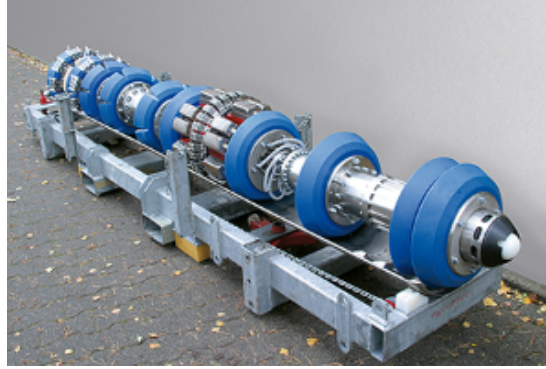
Figure 2.8: ROSEN Pig [44] inserted into a pipe and used for inspection of long sections of pipeline

While pigging and internal inspection of a pipe are commonplace and suited to inaccessible underground or underwater pipelines [45], there are also many pipes which are considered unpiggable. This can be for a number of reasons including:

- Low Pressure or Flow: The flow may not be sufficient enough to propel the PIG though the pipe.

- Changing diameter and Complex Geometry: Changing of diameters in pipelines means that robots may not be able to fit or inspect.

- Physical Barriers: Barriers such as grates will stop inspection robots going through.

- Reduced Flow: The asset operator may not want the flow to be reduced by a PIG.

For these reasons above, Pigging is not the only possible method of inspecting pipes. Robotic systems to deliver more specialised, qualitative and precise measurements

are also needed to give a complete picture of the health of critical parts of a pipe, particularly in scenarios where PIG inspection is not viable or practical.

2.2 Mapping and Positioning Methods

To make a map of defects and corrosion, the location of the inspection needs to be referenced and recorded. If the location of the defect is mapped incorrectly, as shown in Figure 2.9, finding the correct location to do a repair or track the size of a defect over time, becomes more difficult. This makes positioning for defect mapping a significant issue for defect monitoring and repair. There are many setups and sensors which are used to try and combat this issue, with environmental characteristics and inspection requirements dictating which method is suitable.
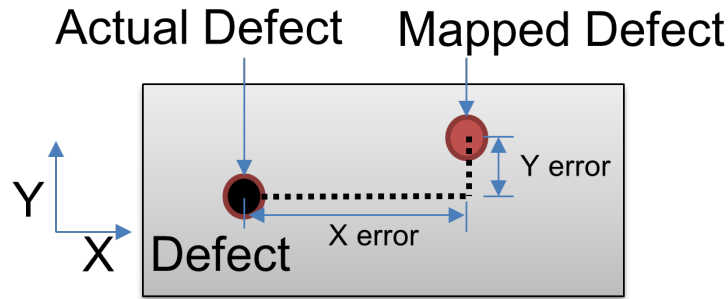
Figure 2.9: Defect Mapping Error

2.2.1 Position Sensor Types

There are a number of different methods of categorising positioning sensors and the measurements obtained from them. Table 2.1 summarises the main advantages and disadvantages of these types which are detailed below:

External Sensors: Sensors which are not attached to the robot body or require devices external to the robot platform. Examples include GPS and photogrammetry systems. These tend to be absolute measurements which is a measure of the position within a fixed global reference frame. The main disadvantages are that external sensors

require increased set-up time, tend to be costlier and are bulky due to the extra external equipment required.

Internal Sensors: Sensors which are attached to the robot. These tend to be relative measurements which rely on the previous measurements to obtain the current estimate and are therefore subject to time dependant integral error that increases over time. Examples include wheel encoders and accelerometers. They can be very accurate over short periods of time and do not require external apparatus to be set-up. Traditionally, using wheel encoders or accelerometers for positioning incurs unworkable integral error as the acceleration signal is double integrated to obtain a change in position [46, 47].

Absolute Measurements: Measurements which do not rely on previous measurements to obtain the current estimate. Each measurement is independent of previous measurements. Examples include Laser Range Finders and GPS.

Relative Measurements: Measurements which rely and build on the previous measurements to obtain the current estimate. The new latest position measurement is based on the previous estimate. Examples include encoders and accelerometers.

Table 2.1: Describing the advantages and disadvantages of different sensor types
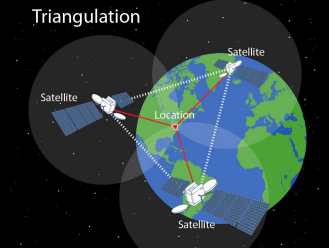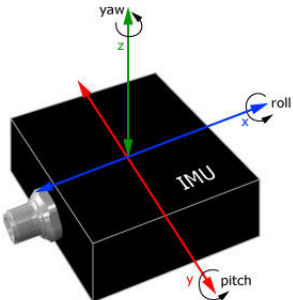
	Advantages	Disadvantages	Example
External Sensors	• Tend to be absolute measurements	• Increased Setup time • Tend to be more costly • Bulky	Figure 2.10: GPS is an example of an external sensor setup[7]
Internal Sensors	• No external equipment	• Tend to be relative measurements	Figure 2.11: An IMU is an example of an internal onboard sensor[8]

Table 2.2: Describing the advantages and disadvantages of different measurement types

	Advantages	**Disadvantages**
Absolute Measurements	• No integral error	• Tend to be external sensors
Relative Measurements	• Tend to be accurate over short periods	• Error which accumulates over time

2.2.2 Mobile Robotic Positioning Methods

The main challenge faced by mobile robotics, especially when considering autonomous systems, is accurate localisation and position estimation [48]. Probabilistic estimation of a robot's position through fusion of multiple sensor outputs is a strongly researched area in robotics. It is a long-standing problem in the field and is considered a fundamental requisite of autonomous systems [49].

Position is measured using a range of sensors and accurate positioning is critical for both reliable robot navigation and defect mapping. These sensors are subject to errors and uncertainties which can compound over time which leads to inaccurate localisation of defects found using the system. Fusion of local sensory data, such as odometry data, and global positioning measurements, such as GPS, through approaches such as the Kalman Filter can enhance the position estimation. Position and orientation measurements can be used for both real time and post processing. This information can be used in real time for better control of the system. For post processing, position information can be used for mapping of defects.

Traditional outdoor GPS systems are not practical in most of the industrial situations where crawler robots are utilized as the GPS signal can be disrupted by the surroundings, referred to as multi pass error [50]. GPS can have an error in the meter range, which is

26

unusable on its own for inspection positioning applications. However, there are Indoor Positioning System (IPS) variants which can be used in place. Examples of methods which can be used for IPS include:

- Odometry: Wheel Encoders

- Trilateration: Ultra Wide Band (UWB), indoor GPS (iGPS)

- Optical Methods: QR Codes, Photogrammetry, Visual Odometry

- Inertial: Inertial Measurement Units (IMUs)

A summary of sensors is provided in Table 2.3 with the subsequent subsections discussing in further detail.

Table 2.3: Summary of indoor positioning types

Type	Examples	Advantages	Disadvantages
Odometry	• Encoders • Visual Odometry	• Onboard system • Can be low cost • Simple • Accurate over short time periods	• Integral Error
Trilateration	• Ultra Wide Band (UWB) • Indoor GPS (iGPS)	• Absolute positioning	• Requires line of sight • External
Optical	• Photogrammetry • QR Codes	• Can give accurate orientation and position measurements	• Can be complicated to setup and process data • Can require external setup
Inertial	• Accelerometer • Gyroscopes • Magnetometers	• Onboard system	• Magnetometers not viable • Gyroscopes have integral error

Odometry

Odometry, sometime refereed to as dead-reckoning, is an approach whereby information from sensors, such as encoders, are used to estimate the change in position over time and therefore can be used determine the past trajectory of the robot. These changes are summated though integration methods and provide the robot position relative to its starting position, therefore, odometry methods based on the summation if incremental measurements and are sensitive to unbounded integral error over time [51]

Encoders are the most commonly used movement sensor for robotic systems [52]. There are many types of encoders, such as magnetic, mechanical and optical, with optical. A review of different encoder types is given in [52]. For mobile robotics, encoders are usually used to determine the distance traversed by a wheel or track and can be used for odometry purposes. Encoders are used to calculate the distance moved in each time step. While the increasing nature of the error associated with odometry methods are well known, it is commonly agreed that odometry is an important part of robotic navigation and position estimation. This is because it provides good short-term accuracy, is relatively inexpensive and allows for high sampling rates [53].

The main causes of error when using wheel encoders can be separated out into systematic errors, such as unequal wheel diameters, and non-systematic errors, such as wheel slippage. Systematic errors can be taken into account through the commonly used University of Michigan Benchmark (UMBMark) method [54]. However, non-systematic errors such as surface condition and profile can be unpredictable in nature, thus they will still be present.

Trilateration Methods

Trilateration measures the distance from 3 or more known points (beacons) to calculate the position of a mobile beacon. This is usually done using time of flight calculations and can be quite precise. The trilateration method is described in further detail in [55].

Examples of methods that use this trilateration are:

29

- iGPS: 20-60kHz range, also known as ultrasonic GPS. An example is the Marvel Mind [56] system claiming positional accuracy of $\pm 2cm$.

- UWB: 3-10GHz range, uses radio waves. An example is the Pozyx [57] system claiming positional accuracy of $\pm 10cm$.

These systems need to be calibrated and the position of each of the beacons needs to be known to have accurate measurements. Investigative work conducted in conjunction with Eddyfi Technologies to characterise the aforementioned systems found that the accuracy claims were only upheld in very specific conditions, such as having a stationary mobile beacon with no obstructions in the line of sight. Temperature also needs to be constant and known as significant variations in temperature can affect the measurement for iGPS systems. Line of sight is required as obstructions cause noise which make measurements more inaccurate. While UWB can penetrate some materials, concrete, walls and metal are not penetrable.

Optical Methods and Machine Vision

Cameras and Machine vision is being increasingly used in robotic manipulation and localisation [2, 21, 58, 59]. One method of using machine vision to help solve the localisation problem is by using and tracking landmarks.

There are two kinds of landmarks, natural and man-made landmarks. Natural landmarks have the advantage that they do not need to be placed manually into the environment, instead, the system recognises the landmarks automatically. However, determining what is a natural landmark can be difficult [60] and tend to only work well in structured environments such as indoor corridors. Alternatively, man made landmarks, such as Quick Release (QR) codes can be applied to the environment and used to gauge the absolute position of the system [61]. These are much easier to detect as they are designed to have high contrast which can easily be found by the optical system [59]. Some industrial examples of robotics systems which use visual QR-like codes are Kiva Robots which are most commonly known as being used by Amazon in their warehouses

[62] , and Boston Dynamics Spot system [63].

The main advantages of using QR codes are that they can be used to gain an absolute reading of position. They are also have a relatively low cost. However, the QR codes need to be manually placed in the environment. For inspection of pressure vessels, hard to reach areas or hazardous areas, this can be impractical if the QR landmarks are not a permanent fixture in the environment.

Visual odometry is also possible, whereby a camera is used to determine the distance moved by tracking or matching features in subsequent frames to estimate the motion of the camera [64]. As with wheel odometry, estimates of position obtained using visual odometry are subject to integral error [65]. However, visual odometry is not subject to wheel slippage and studies have shown that over longer periods visual odometry can be more reliable and accurate compared to wheel odometry [66].
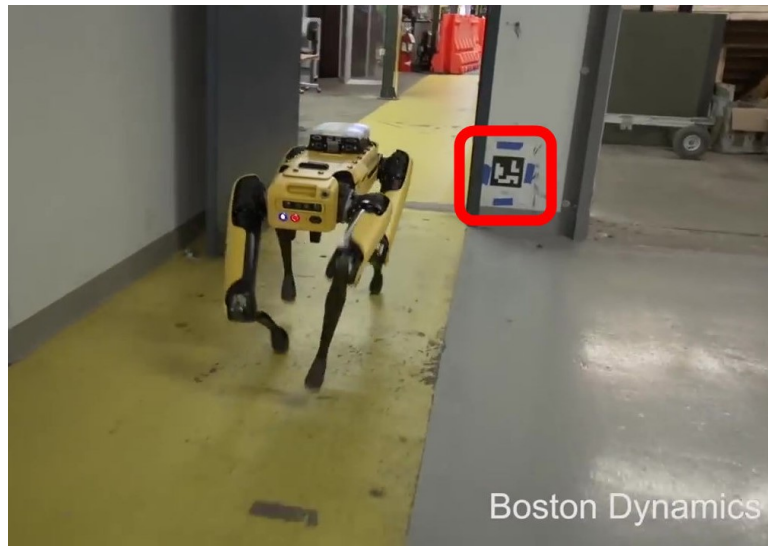
Figure 2.12: Boston Dynamics Spot using QR codes for localisation

Inertial Measurement Units

An Inertial Measurement Unit (IMU) has become an affordable and viable onboard robotic sensor. This is due to advances in Micro-Electro-Mechanical Systems (MEMS)

manufacture reducing manufacturing cost and size of the component [18]. As a result, these devices are now used in every day electronic devices, such as mobile phones.

IMUs can be used to estimate the orientation, velocity or position of a robot. A typical set-up for 9 Degree of Freedom (DOF) IMU is a 3-axis accelerometer, a 3 axis gyroscope and a 3-axis magnetometer. An IMU sensor is a proprioceptor, it senses changes within the robotic system rather than sensing changes or movement from the outside world. This reduces the inaccuracies that are associated with the surrounding environment which occur with exteroceptor (external sensing) sensors such as ultrasonic and laser range finders.

IMUs are well suited to determining the orientation of an object. However, they are not very reliable at determining displacement due to the double integration of accelerometer readings and therefore is subject to integral error [13, 67]. Using accelerometers for robot navigation have generally given poor results due to poor signal-to-noise ratios, sensitivity to uneven terrain and extensive drift [53].

Orientation estimation is usually achieved by fusing outputs of a 9 DOF IMU. However, in many industrial environments, the magnetic field vector cannot be taken as constant as there are local ferrous objects which may interfere with the local magnetic field [68], as well as magnetic interference from permanent magnets and magnetic wheels from a climbing robot. Gyroscopes are also subject to integral error as the angular acceleration is integrated to determine the angular change. A previous work uses used a 3-axis accelerometer for tilt sensing of a stationary object which , has no drift over time due to there being no integration step [69] and relies on the 3-axis accelerometer output only. However, this only gives the roll and pitch of the accelerometer, and the yaw component is necessary to calculate the orientation using this method.

In industry, IMUs are used for both orientation and position estimation. IMUs are currently used as part of a localisation system. However, they are not used specifically for localisation on pipe surfaces. Examples of IMUs utilized in positioning include [22,

70, 71], where accelerometer data is used to determine distance travelled. However due to the relative measurement, these works include a correction method which attempts to reduce drift. This correction is usually a post capture filter in the form of a Kalman filter [23] or Particle Filter [72] which are common data fusion algorithms used in off the shelf IMUs and general robotics. Though not investigated here, they will be considered in future work. This work only considers the accelerometer output of an IMU.
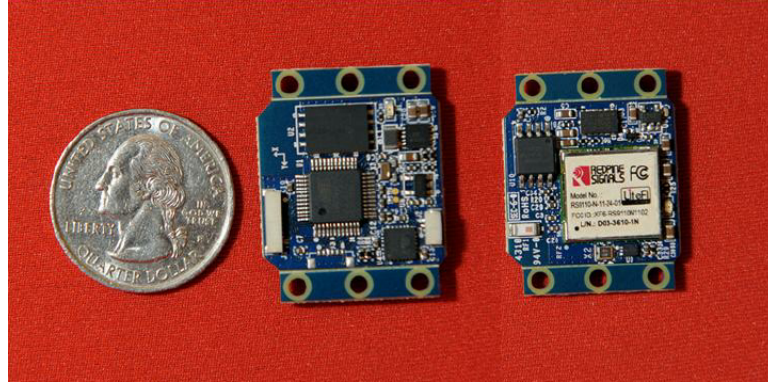
Figure 2.13: Example of the size of an IMU [73] showing the small size of the devices

2.2.3 Hand Held Probe Positioning Methods

There are significant synergies in the systems and methods that can be used to position both manual hand held probes and robotic platforms. Many of the positioning methods used for robotic positioning can be deployed for manual probe localisation. These applications are rediscussed below.

Gridding

Gridding is the process of marking out the inspection area into a grid system for the inspector to follow with a probe. An example of this is illustrated in Figure 2.14. This process is very reliant on the individual inspector to accurately create and follow the grid. There are options to try and reduce the reliance on the operator, such as plastic sheets with pre-drawn grids or setups such as the one in Figure 2.15. While these remove the uncertainty associated with drawing the grids, this method is still heavily reliant on the inspector following the grid correctly to gain full coverage. Encoders can

be used to ascertain the movement along the grid, or positioning can assumed in the software, where the inspector places the probe in each section of the grid and tells the software which section is currently being scanned.

Figure 2.14: PEC Grid Setup Example

Figure 2.15: PEC Grid Setup Example 2

Encoders

Complex pipe geometries pose a challenge for manual probe positioning. Obstructions such as pipe supports or saddle welds need to be inspected in a consistent manner to ensure the integrity of the inspection.

3D encoder systems are anchored to the asset and utilise encoders in 3 axes to record the 3 dimensional movement. An example of such as system is the Phoenix SWIS scanner shown in Figure 2.16. The scanner also limits the movement of the probe to help ensure that the path of the probe is optimal.

There are a few disadvantages associated with using these types of devices. One drawback is that these systems are very specific in they geometry which they can be used to inspect. They are also bulky and need to be set up and calibrated before inspection

Figure 2.16: Phoenix SWIS Saddle Weld Scanner [9]

Drawstring encoder systems are also used in industry. These systems usually use multiple string encoders to determine the distances moved in the given axes. Figure 2.17 shows an example of a 2 axis string encoded attachment which gives the X and Y position of the probe.

[9]Phenix ISL: phoenixisl.com/product/swis

Figure 2.17: NDT Systems StringScan II [10]

Volumetric Tracking Methods

Volumetric tracking systems, such as photogrammetry or laser systems, can be used to track a probe in 3D space. These systems tend to be used in areas where the asset being inspected can be bought to a fixed location, negating the need to assemble and setup the complete system for each inspection. Inspection industries where this is the case include the aerospace industry, for example, inspection of plane wings. An example of this kind of setup is shown in Figure 2.18 and Figure 2.19, using multiple IR (Infrared) cameras to track a hand held probe being operated by an inspector in real time.

A major drawback of these systems for pipe inspection is the lack of portability. Usually these systems have to be set up in the inspection area and calibrated, which can require training and can be time consuming. Cost is another issue as systems can range from the £5K − £100K price range. Line of sight of at least 3 cameras are needed to obtain a 3D position, which can cause issues for non-flat inspection surfaces. These systems are not deemed suitable for on-site hand held pipe inspection for the reasons stated above, however they are discussed here for completeness.

---

[10]NDT Systems: ndtsystems.com/product/stringscan-ii
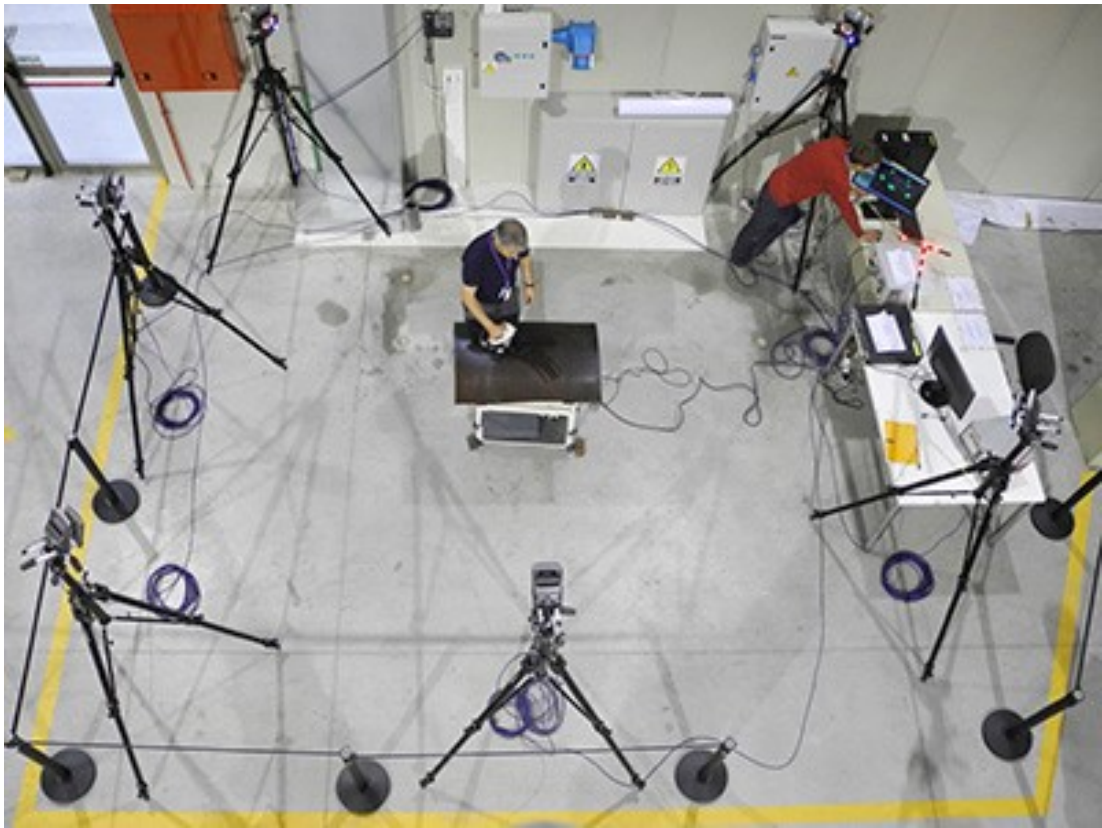
Figure 2.18: WiiPa: Wireless Positioning Technology using IR Cameras to track the position of a probe being handled by an inspector[11]

Figure 2.19: WiiPa: Wireless Positioning Technology using IR Cameras Close Up[12]

2.3 Robotic Crawlers and Adhesion Types

There are a several types of robotic solutions which can be used for inspection of various assets in the petrochemicals industry. These are generally classified into two types; fixed robots and mobile robots. Mobile crawler type robotics can further be separated based on their type of motion which is used to navigate. These are:

- Wheeled Crawlers

- Walking Crawlers

---

[12]Tecnatom NDT: tecnatom.es

- Sliding Crawlers

- Inchworm Crawlers

Wheeled crawlers make up the vast majority of crawler robots. They tend to use simple rotary encoders to determine position and orientation of the crawler and wheel slippage leads to positioning error. Walking crawlers employ a complex kinematic model and the position along the inside of a pipe is usually determined though wheel encoders. Sliding crawlers, or collar robots offer a mechanical solution to the positioning problem by using a fixed frame of reference from the pipe. They have limited degrees of freedom and the sensors follow a fixed path around the pipe [74]. Collar robots tend to rely on encoders to determine their circumferential position on a pipe with the orientation of the sensor being fixed. Wheeled crawler robotics have and increased degree of freedom and this allows for the manoeuvre around obstacles such as supports or valves which are not usually possible without human intervention with sliding or inchworm crawlers.

Mobile crawler robots can also be classified by the mechanisms which they employ to adhere to a surface. Due to the different material that a robot may need to adhere to, some methods are more suited to specific applications than others. For example, magnetic adhesion methods are suitable for ferromagnetic materials, however if there is insulation covering the surface, this method will not be suitable and a different method must be used. Bio inspired and suction methods are included in the Appendix for completeness, although not discussed in the body of this thesis. Each of the relevant climbing types presented have advantages and limitations and may be appropriate for different applications. These are discussed below.

2.3.1 Magnetic

Magnetic traction uses the magnetic force between strong magnets attached to the body of the robot and a ferromagnetic surface. In general, the size of the magnet dictates the magnitude of this force. The main limitations of this traction method is that it requires the asset being inspected to be ferromagnetic, meaning insulated pipes

and pipes made of material such as non-magnetic stainless steel are not suitable for this. Another drawback is that due to the large concentration of force, if the magnets are in direct contact with the surface, the surface can be damaged and coating can be removed as the magnets move over the surface.

Magnetic Wheels

Magnetic Wheels are typically used for locomotion for magnetic traction. Wheels allows the robot to reach relatively high speeds when compared to other locomotion methods [75]. To overcome the issue of coating being damaged due to the strong concentration of magnetic force, thin rubber coverings for the wheels can be used [76]. Wheeled systems have the advantage of being less complicated and tend to be lighter weight compared to tracked systems [77]. For mobile locomotion on cylindrical surfaces, such as pipes, wheeled systems have the advantage that they are more manoeuvrable compared to track systems [78]. An example of a system which uses magnetic wheels is the Scorpion 2 by Eddyfi Technologies shown in Figure 2.20.

Figure 2.20: Scorpion 2 using Magnetic Wheels with Rubber Coverings[13]

---

[13]Eddyfi Technologies: eddyfi.com/en/product/scorpion-2

Tracks

Tracks add more friction compared to just using wheels, although there are constraints with navigation associated with this [79]. This makes control of the robot more difficult and having more friction requires higher power consumption in order to cope with the friction between the tracks and surface. The adhesion force is present due to belly magnets on the body of the robot. Track robots tend to be used where there is less of a manoeuvrability requirement. An example of this is for ship hull inspection [80], where the curvature of the surface is not significant. Large adhesion area created by the tracks allows for greater payload [81]. An example of a system which uses tracks is the Magg 480 by Eddyfi Technologies shown in Figure 2.21.

Figure 2.21: Magg 480 using Magnetic Tracks[14]

2.4   Current State of Inspection Technology

There are inspection solutions in both industry and research which have varying degrees of automation. An overview of what is considered to be at the forefront in the field of automated NDE from industry, academia and various collaborations are presented below.

---

[14]Eddyfi Technologies: eddyfi.com/en/product/magg-magnetic-inspection-robotic-crawler

41

2.4.1   Hand Held Probe Literature Review

Silverwing - RScan:

The Rscan, shown in Figure 2.22, is hand held manual scanner which uses a dry coupled ultrasonic wheel probe. It is designed to be used in remote locations. The dry coupled wheel probe eliminated the need for a constant supply of couplant. The probe is capable of measuring material thickness from 2.5mm to 100mm. Real time A-scan and B-scan data can be displayed using the Swift system. The minimum pipe diameter which can be inspected is 50mm.

Positioning of the Rscan is done using optical encoders to determine the distance travelled by the probe. The magnetic wheels of the system help to ensure that the optical encoders remain in contact with the surface and reduces the chance of slippage on ferrous materials.

Figure 2.22: Silverwing Rscan[15]

Eddyfi - PEC Probes:

Eddyfi offers a range of PEC probes for different applications, including underwater environments. PEC is an electromagnetic inspection technique which detects reductions in wall thickness in ferromagnetic structures which is a volumetric measurement that is converted into an average thickness measurement [82]. A magnetic field is created by an electrical current though coils to generate PEC. These probes can be used to inspect under insulation and come in a variety of sizes. A single encoder can be attached to the probe to determine the distance travelled to create a map. The previously mentioned gridding process is also used to generate a thickness map of the inspection area and is reliant on the accuracy of the inspector to place the probe in the relevant areas.

---

[15]Eddyfi Technologies: eddyfi.com/en/product/rscan-manual-ultrasonic-system

Figure 2.23: Eddyfi PEC Probe with Encoder[16]

PEC Arrays (PECA), including the Sharck and Spyne, are another family of probes available from Eddyfi. The Sharck is designed for depth sizing of surface breaking defects found in steel pipes. The minimum detectable crack is 1.5mm in length and can inspect pipes with a diameter upwards of 254mm. It uses an embedded spring loaded encoder for positioning. The Spyne is a flexible PECA. It also uses embedded spring loaded encoders for positioning. It incorporates a "Grid-as-U-Go" system, which draws lines with markers on each side of the area which has just been scanned, allowing the inspector to check if full coverage has been achieved.

---

[16]Eddyfi Technologies: eddyfi.com/en/product/pulsed-eddy-current-pec-probes

Figure 2.24: Eddyfi PECA Sharck Probe[17]

Figure 2.25: Eddyfi PECA Spyne Probe[18]

---

[17]Eddyfi Technologies: eddyfi.com/en/product/sharck-hr-eca-crack-detection
[18]Eddyfi Technologies: eddyfi.com/en/product/spyne-array-pipeline-crack-assessment

Zetec: Paintbrush

The Zetec NDT Paintbrush is a hand held device used for corrosion mapping. It can operate on both curved and flat surfaces. It has two encoded wheels which track the position of the device in real time, which allows the inspector to see which areas need to be inspected to achieve full coverage. The two wheel encoders allow for basic differential drive kinematics to be calculated, showing the position and trajectory of the device based on the wheel movements. The wheels are magnetic to reduce the chance of slippage The NDT Paintbrush uses Phased Array UT to determine the wall thickness and to create a C-map of the inspected area. The NDT Paintbrush is shown in Figure 2.26. The use of only wheel encoders exposes this device to integral error, and therefore it will not be reliable over long inspection periods.
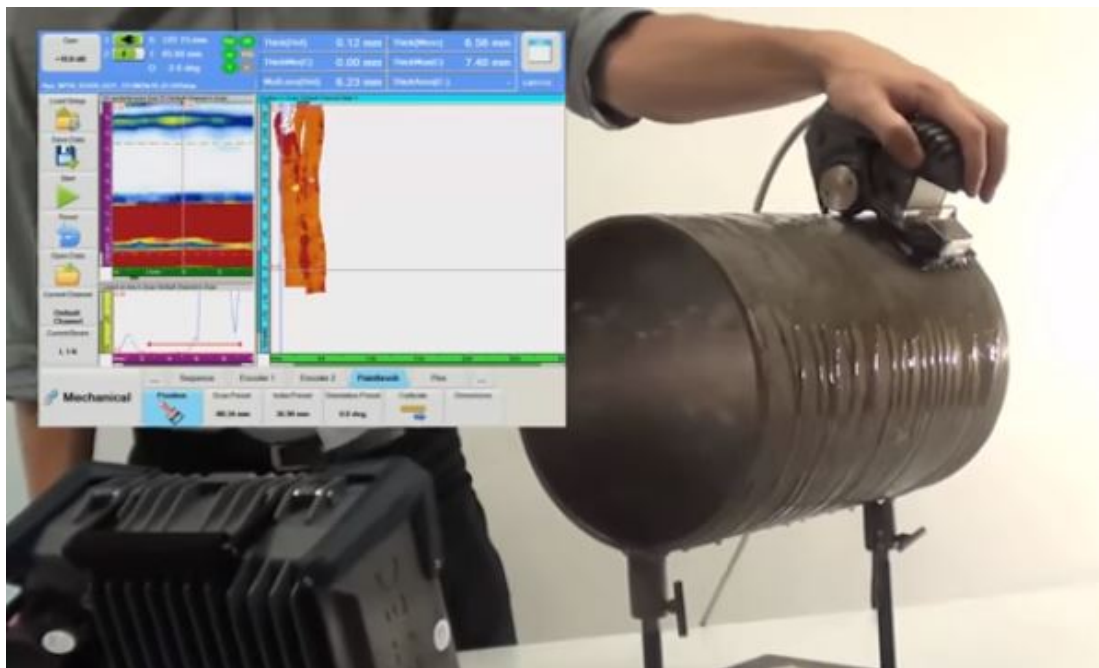
Figure 2.26: Zetech NDT Paintbrush[19]

---

[19]Zetech: zetec.com/products/mechanical-systems/scanners/ndtpaintbrush

Limitations with Current Systems

All of the hand held positioning systems discussed rely on the inspector to accurately and precisely determine the starting position and reference for the defect map. With the system which rely on the encoders, the initial position of the scan is chosen by the inspector and marked in the map. There is no way to ensure that the actual initial position and the position input into the software is the same as this relies on the inspector correctly choosing and marking out starting reference point. All of the systems use encoders, which is a relative measurement type. This is not a major problem with regards to accuracy over the short inspection lengths expected from using handheld probes, however there is still the possibility of wheel or encoder slippage, which will affect the positional accuracy of the system.

2.4.2 Automated and Robotic Inspection Literature Review

Eddyfi

Over the past 4 years Eddyfi has increased its presence in the automated NDE solutions field, mainly though its acquisition of both Silverwing and Inuktun. A summary of current capabilities is detailed below.

Scorpion 2:

The Eddyfi Technologies Scorpion 2 [83] , shown in Figure 2.27 is a crawler robot fitted with a dry-coupled remote-access ultrasonic wheel probe for inspection of tank shells and other similar structures. The system consists of 4 magnetic wheels in a differential drive setup with the wheels on the left hand side and right hand side being controlled independently. This allows for two wheeled differential drive kinematics to be used to describe the movement of the robot in most cases, however this is not the case for turning. This is because the wheels are required to slip to rotate the robot.

The dry coupled wheel probe eliminates the need for traditional couplant which allows the system to be lighter and more manoeuvrable. The wheel probe can measure

thickness between 2.5mm – 100mm. The Scorpion 2 has a scan speed of $125mms^{-1}$.

The Scorpion is controlled using a joystick and the crawler is able to drive in a straight line with mechanisms in place to correct the direction of the robot should it slip. Spring loaded encoders are attached on either side of the Scorpion to help ensure that the Scorpion is driving straight and to generate B-Scans. Another key advantage of the Scorpion is that it minimises maintenance and inspection costs as it eliminates the need for scaffolding on the tanks and therefore reduces safety risks by reducing the amount of time personnel spend in dangerous conditions or time taken to prepare the site to be safe.

Figure 2.27: Silverwing Scorpion 2

Silverwing - RMS:

The RMS [84], show in Figure 2.28, is a differential drive robot equipped with a high resolution Phased Array probe attached to a sweep arm to cover larger areas quickly. It can be operator controlled, or programmed create automatic corrosion maps. The RMS has a scan resolution of 1mm, compared to more traditional course corrosion

scanning with resolutions of 3-5mm. The capability to collect high-resolution scans at fast speeds improves the probability of detection and characterisation of defects. The RMS is designed to inspect pipelines, pressure vessels, storage tanks, ship hulls among others. Positioning and localisation of the RMS is done though encoder readings. Localisation is limited to 1D position as the rotation is not recorded due to skid steer operation.

Figure 2.28: Silverwing RMS

Inuktun - MaggHD:

The MaggHD [85], show in Figure 2.29 is a miniature crawler robot which offers remote visual inspection. It uses tracks instead of magnetic wheels to manoeuvre around. it can travel distances up to 100m in air, or 60m underwater. Its small size allows the MaggHD to be used to inspect spaces where the entry is small or for confined spaces. The MaggHD is designed to eliminate the need to personnel to enter confined spaces or scaffolding requirements for visual inspections. it has a relatively low payload of 4.5kg due to its small size with a maximum speed of 9m per min.
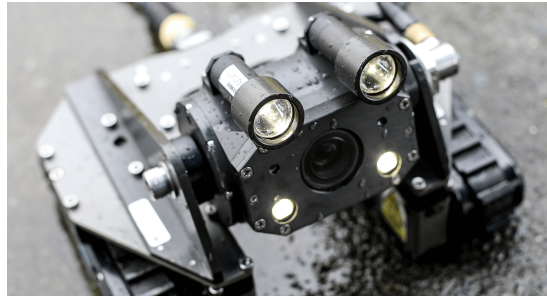
Figure 2.29: Inuktun MaggHD

Inuktun - Versatrax 50,100,150:

The Versatrax 50 [86], shown in Figure 2.30a is remotely controlled and is designed to inspect tight confined spaces. Its small size allows it to be used in confined access areas where other larger devices can not reach. It is able to enter spaces as small as 50mm. It has a camera attached for real time visual inspection and can travel up to 100m. Its small size is ideal for inspection of heat exchangers, coiled tubing and small diameter pipes. It can operate in both air and water. it has a max payload of 4.5kg and a max speed of 1.9m per min.

The Versatrax 100 [87], Figure 2.30b is designed to fit into openings of 100mm or more. it has a payload of 4.5kg and a max speed of 9m per min.

The Versatrax 150 [88], Figure 2.30c, is a more sophisticated robotic crawler which can travel up to 1km. It can be fitter with fibre optic cables for high bandwidth payloads and can operate in openings of 150mm or greater. The attached camera is motorised so that the operator has more control over the remote inspection. It has a max speed of 6.4m per min with a payload of 91kg.

(a)

(b)

(c)
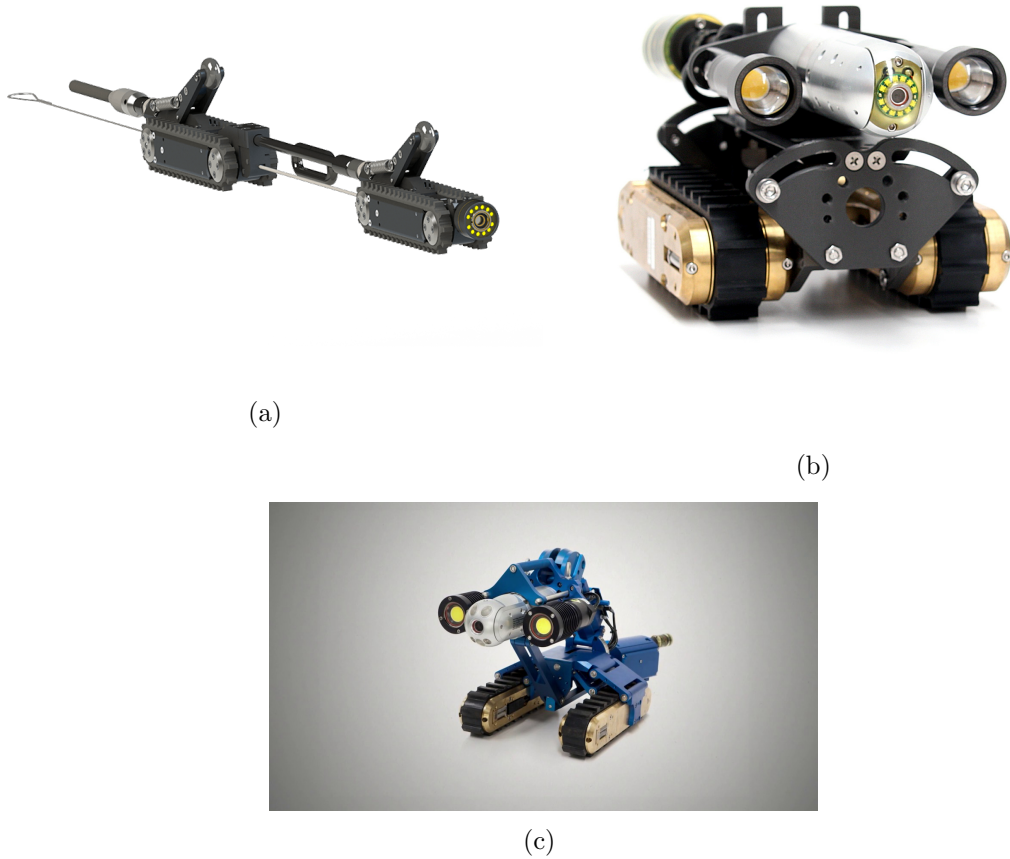
Figure 2.30: (a): Versatrax 50, (b): Versatrax 100, (c): Versatrax 150

Petrobot Project

Petrobot

The Petrobot project is a consortium of companies throughout the NDE value chain which aims to develop a series of robots to conduct remote inspection of various assets, including tanks and pressure vessels. The main objectives of the project are to minimise exposure of personnel to hazardous conditions, reduce operational downtime and decrease the total expenditure of the inspection process. This collaboration between industrial players highlights the importance that the industry has put on finding feasible

solutions to the challenges faced when employing robotic inspection platforms.

A number of robotic solutions were developed as a result of this R&D collaboration. The most relevant have been described below.

GE Bike:

The Bike platform started development as an industry research project at the Swiss Federal Institute of Technology (ETH Zurich) [89] and is now part of Waygate Technologies. It is a light weight crawler robot with a high degree of manoeuvrability. As a consequence of this, the total payload of the system is relatively small and lighter tools have to be used in order to reduce the weight of the platform. The Bike can be equipped with an operator camera or NDE sensors.

The Bike has the ability to climb vertical walls as well as overcome ledges and weld obstacles though the use of a unique magnetic wheel design. The total weight of the system is less than 10kg and can be deployed though a 12" (300mm) opening.

The Bike also comes with 3D spatial awareness and mapping capabilities. Inspection data can be automatically tagged with a position and then mapped onto a digital twin. Assuming that an accurate model of the asset being inspected in available, the system can localise itself with accuracies of around $\pm 25mm$.

Figure 2.31: Petrobot GE Bike [89]

Fast Crawler:

The Fast platform [90] is a magnetic crawler which is designed to enter confined spaces. It has a rotating laser which generates a 3D image of the environment using a point cloud. This allows the operator to know where the robot is in the tank/pressure vessel. With this information, operators can revisit a location for further future inspection. The system height is below 15cm, which allows the platform to move under many obstacles.

The Fast can be mounted with various inspection tools. For Visual Inspection, high resolution cameras can be attached. An eddy current system is also available. UT and cleaning modules are also available.

Situational awareness of the robot is constructed though three methods; Laser based 3D point cloud, IMU data and odometry data. These together help with Simultaneous Localisation and Mapping (SLAM). This situational awareness allows operators to plan routes and the Fast platform can run independently along these predefined paths.

Figure 2.32: Petrobot GE Fast Platform [90]

Other Examples

Robotic crawlers are a topic of interest for research due to the previously mentioned advantages they can bring to industry. As a result, there has been research in this field at other institutions.

SAIR (Saudi Aramco):

The Saudi Aramco Inspection Robot (SAIR) [91] is an industrial inspection robot developed by Saudi Amramco and the King Abdullah University of Science and Technology (KAUST). It is a fully contained wireless system that uses magnetic wheels to conduct either ultrasonic or visual inspections and can also be fitted with gas detection sensors. The system utilises a magnetic holonomic wheel for increased manoeuvrability, allowing it to navigate complex curved surfaces. The system can be operated on curved surfaces of down to a radius of 8 inches to a flat plate. The system weighs less than 10kg. A and B scans can be collected from the sensors. Its dimensions are; length; 325mm, width; 180mm, height; 215mm. It has a max driving speed of 140mm/s. The lack of cables increases the area that can be inspected as there is no wires to be tangled.
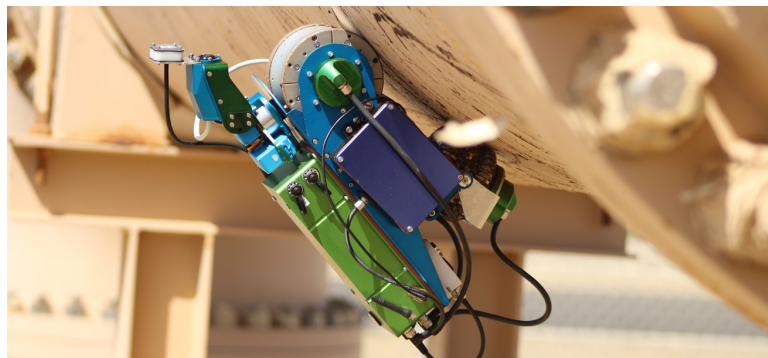
Figure 2.33: Saudi Aramco Inspection Robot [91]

Navic 2 (Jireh):

The Navic 2 [92] is a modular magnetic crawler robot which is steerable and designed to incorporate multiple different attachments for different inspection applications. The

system is water tight and has a low profile of 70mm, allowing for low clearances. attachments include various probe holders and a raster scan arm. The positioning of the Navic 2 is uses spring loaded encoders to help ensure contact to the surface.
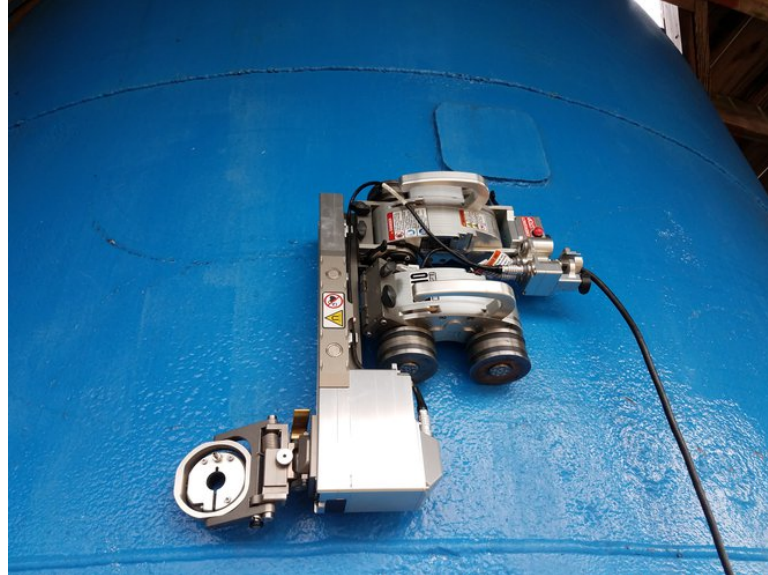
Figure 2.34: Navic 2 Modular Crawler [92]

MINOAS

The MINOAS (Marine Inspection Robotic Assistant) platform [93] is a lightweight crawler robot is wirelessly operated and has a wireless camera mounted on it. The total weight of the crawler is 700g in total, encompassing the camera and the batteries. M. Eich et al [77] used a 3D camera based tracker was designed and built to capture the positional information of the crawler. This was done by tracking bright LED on the robot. This tracked position was then translated onto a 3D model of the component being inspected. Each wheel contains 50 neodymium magnets and is a differential drive setup.

Limitations with this system include:

- Low Payload: The low payload of the system limits the types of sensors which can be attached.

- External Positioning System: An external tracking system needs to be setup and the transformation between the tracker frame and the component frame needs to be known for accurate positioning.

- 3D CAD Model: An accurate 3D model is needed for accurate positioning

Figure 2.35: MINOAS Crawler [77]

Research at Strathclyde

Research at The University of Strathclyde has been conducted in the field of mobile robotics and robotic positioning. A Remote Sensing Agent (RSA) [24], shown in Figure 2.36 was previously developed at the University. The RSA is a 3-wheeled differential drive robot with a passive castor wheel and magnetic drive wheels for traction.

Figure 2.36: Remote Sensing Agent (RSA) [24]

There has also been previous work relating to mobile robotic positioning systems and methods. These include:

- Guided Waves: Work is being conducted in CUE, in conjunction with Warrick University, to use Guided Waves and Electro-Magnetic Acoustic Transducers (EMATs) to position mobile robotic crawlers on metal surfaces while screening to check for reduction in wall thickness [94, 95, 96]. The idea is to use multiple EMAT readings at different positions to triangulate between the guided wave response from artefacts to determine the robots position in a 2D plane with reference to these artefacts.

- Cricket: IPS systems, specifically the Cricket system, have been used to position mobile robotics in previous studies [24, 97]. Trilateration was used to determine the position of the robot from multiple beacons which is a method used for similar IPS systems.

- Visual Odometry and Image Stitching: Work on using cameras to determine the motion of the robotic platform has been done in the department as well. A single

camera can be can be positioned to monitor the the surface of the structure under the robot as is moves [33]. Tracking features from the camera allows the path of the robot to be determined. Image mosaicking has also been used for visual odometry for pipe inspection.

- Photogrammetry: CUE has a Vicon photogrammetry volumetric measurement system which has been used in multiple studies in the field of robotic positioning. The system has been characterised [98] and used as ground truth in subsequent studies [97, 99].

- Sensor Fusion: Beysian filters, specifically the Kalman and Particle filters, have been investigated for sensor fusion purposes [6]. Encoder measurements were fused with IPS measurements. Both the filters tested were found to significantly reduce the robot path error for a typical raster scan. The study found that differential drive robotic kinematics are sufficiently linear so that the EKF yields better results compared to the particle filter.

2.4.3 Limitations with Current Solutions

Current readily available mobile robotic platforms lack appropriate positioning solutions. Typically, there is no system in place to determine the position and orientation of the vehicle inspecting a pipe, or it is of low quality [34]. For current absolute positional measurements, external setups, such as a laser tracker, need to be used as with the Minoas system [93]. CAD models are also used, for example with the BIKE system, where it is assumed that the system is traversing over the model. However, if the CAD model is not accurate and does not represent the reality of the asset, positioning becomes less accurate, particularly with changes over time, such as changing ovality of a pipe under constant load. Other systems, such as the Scorpion 2 and SAIR platform rely simply on encoders which do not make them suitable for applications were the operator does not have line of sight of the inspection or for autonomous use over long periods of time. None of these systems have positioning methods that are suitable for continuous or long periods of autonomous inspection.

Research has been conducted regarding the mechanical design of a mobile robotic platform for manoeuvrability in order to access hard to reach areas, for example, the GE Bike platform [89], however current platforms lack methods of obtaining accurate position readings. This is especially the case when external positioning systems cannot be utilised due to industrial and space constraints. This thesis aims to demonstrate how an onboard sensor can be used to obtain absolute position measurement for pipe inspection robotics, circumventing the need to rely on external positioning systems.

2.5   Problem Outline

As stated previously, robotic positioning in the field of NDE is a vital aspect which needs to be addressed if automated solutions are to play a larger role in industry. There are many aspects relating to the positional accuracy, system setup and cost which need to be considered.

In an ideal situation, the inspector using an inspection system would need to do minimal amount of work setting up and calibrating the equipment. Current systems and procedures, as described previously, require the inspector to do work setting up the system or prepare the site for inspection.

There are many different wheel setups for crawler robots for pipe inspection. The robot setup modelled in this work is a 3 wheel differential drive robot which consists of 2 drive wheels powered by motors and a single castor wheel. There are many advantages of using 3 wheeled systems compared to 4 wheeled differential drive systems. 3-wheel robots are more manoeuvrable on pipes in particular [48]. In rotational manoeuvres, 4-wheel differential drive systems are required to skid or slip in order to turn, whereas 3-wheel systems are not. This slipping makes pose estimation difficult while using wheel encoders as the encoders are unlikely to register the slip. These reasons make 3 point of contact rig or robots simpler kinematically compared to setup with more contact points.

With regards to curved surfaces, it is physically possible for a rigid 4 wheeled system

to have only 3 points of contact with the surface as one of the 4 wheels can come off the surface as the robot changes orientation on curved surfaces [78]. This is mathematically impractical to consider. Conversely, with a 3-point of contact systems, the 3 points can always be in contact with the surface, as such, only a 3 point of contact system is considered.

This thesis presents a method of measuring the position and orientation of a 3-wheeled mobile robot on the outer surface of a horizontal pipe by calculating the circumferential clock face angle (ω) and the orientation (α), shown in Figure 2.37. This is achieved using a relatively low cost, onboard acceleration sensor and knowledge of both the pipe and robot geometry to produce an absolute measurement of these angles without time integral error from an onboard sensor.
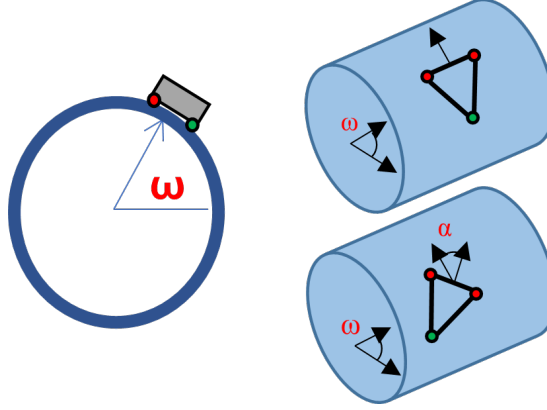
Figure 2.37: Robot pipe localisation problem diagram showing the position angle of the pipe (ω) and the orientation angle (α) of a 3-wheeled robot on a pipe

In this setup, the acceleration force due to gravity is taken to be a constant value and in a constant direction which does not change with time. For the reasons mentioned above regarding the challenges associated with using other IPS systems, including gyroscopes and magnetometers, this work only utilizes the 3-axis accelerometer output from an accelerometer to calculate absolute measures of the ω and α angles.

2.5.1 Applications for Automated NDT

There are many factors which are pushing industry to adopt robotic and automated NDE solutions. These include:

- Increasing Regulations: Governments and regulating bodies are increasingly applying more stringent rules that companies need to comply with [**singh˙three˙2000**].

- High Downtime Costs: Inspections can require operational plants to be shut down for the duration of an inspection. This will lead to loss of production and use of the plant, causing operators to lose money.

- Health and Safety: Many inspections take place in hazardous environments and may require additional safety measures to be put in place. An example of this would be scaffolding.

- High Training Costs: Ensuring that inspectors are able to collect the necessary data requires training. Training may also be necessary for inspections at height or in confined spaces.

- Shortfalls of Manual NDE: Well documented phenomena such as operator fatigue reduces the reliability NDE inspections.

Hand Held NDE Application

Gridding is the process of marking out sections of an asset to be systematically inspected manually. This manual process can be used for inspection methods such as PEC or PAUT testing to try and ensure full coverage of the desired inspection area. However, this process can be time consuming as inspectors must measure out and draw the grids on the surface. For applications such as PEC, it is possible to have a ready made grid which can be placed on the inspection surface. This is possible because of the non-contact nature of PEC inspection, however, this methods is not possible for contact inspection methods such as PA. Another issue with manual inspection is relying on the

inspector to accurately follow the grid to ensure full coverage. Over time, inspector fatigue can become apparent and full coverage may not be obtained.

Chapter 3

Mathematical Forward Model

An analytical mathematical model for simulating the 3-axis accelerometer readings from a given ω (clock-face position angle) and α (orientation) was developed. This allows for the ideal accelerometer output to be calculated from any combination of orientation and position inputs. This model uses the intersection points between 2 perpendicular cylinders and the intersection of a sphere and a cylinder to model the 3 points-of-contact. From these points, the 3-axes of an accelerometer can be modelled and the expected acceleration output can be determined. This process is outlined in this chapter.

3.1 Variable Definitions

A method using the geometry of the robot and pipe is used which preserves the dimensions of the 3 points of contact and maps the contact positions onto the curved surface at any α and ω angle. The relationship between these variables is shown in Figure 3.1. The 3 contact points are D1, D2 and C; for a mobile robotic application, D1 and D2 represent the two drive wheel contact points and C is the castor wheel contact point. The required geometry knowledge is the distance between the robot drive wheels (b), the length from the drive wheel axis to the castor wheel (l) and the radius of the pipe r_p. This setup is shown in Figure 3.1.

The following assumptions were made to simplify the model:

- The pipe is perfectly cylindrical with no grooves or ovality

- Only horizontal pipes are considered initially

- Castor wheel is perpendicular to the drive wheel axis

- Contact geometry is symmetrical

- The 3 points are always in contact with the pipe surface

- Contact can be represented as single points

- Plane of the accelerometer is parallel to the plane created by the 3 points of contact
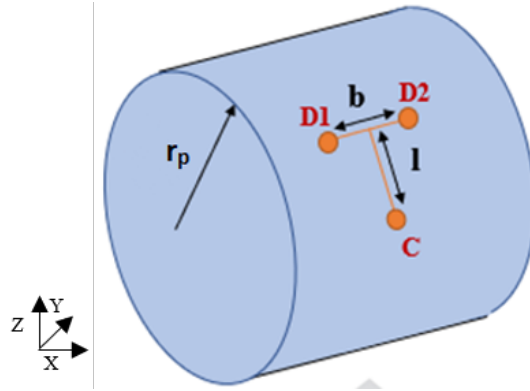
Figure 3.1: Describing the required geometry knowledge for the proposed algorithm. b is the distance between the two drive wheels (D1 and D2), l is the distance between the drive wheel axis and the castor wheel (C) and r_p is the radius of the pipe.
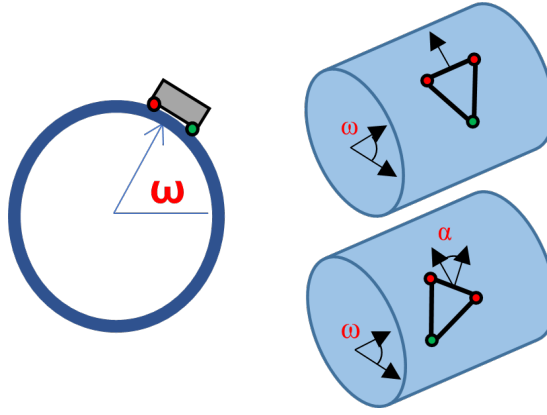
Figure 3.2: Robot pipe localisation problem diagram showing the position angle of the pipe (ω) and the orientation angle (α) of a 3-wheeled robot on a pipe repeated here fint1or convenience

The problem effectively becomes the challenge of fitting a triangle of known dimensions and orientation on a cylindrical surface. There has been work to describe the surface of a cylinder as a number of triangles in the computational geometry and and computer graphics sectors [100, 101, 102]. However, these works look at drawing lines between points of known positions on curved surfaces. These works also look at representing the entire cylinder surface as a group of triangles, whereas the research in this EngD focuses on fitting a single triangle of a known dimensions at a given position and orientation on the cylinder surface.

Using the aforementioned assumptions a method for mathematically describing the pose of a robot for pipes and cylindrical assets is derived. This model allows the wheel positions to be calculated at any ω and α angle on the pipe. This method also ensures that the wheels of the robot are in contact with the surface of the pipe. Grounding the points to the curved surface allows for a more accurate estimation of the wheel positions as this more accurately reflects reality. An analytical model also allows for faster computation and real-time deployment compared to numerical methods which may take much longer to process. Figure 3.3 shows a flow diagram of the relationship between the angles (α and ω) and the accelerometer readings from the X, Y and Z axes respectively A_x, A_y, A_z where the Forward model is highlighted green. This chapter

details the construction of the Forward Model going from predetermined α and ω angles calculating the corresponding 3-axis accelerometer readings.
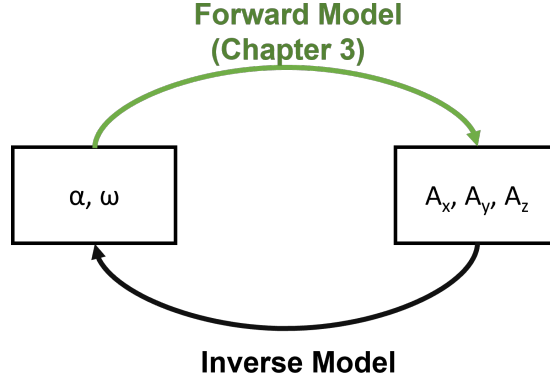
Figure 3.3: Schematic showing the relationship between the Forward Model and Inverse Model, where the Forward Model has inputs of (α, ω) and outputs (A_x, A_y, A_z) and vice versa for the Inverse Model.

3.2 Front Point of Contacts Derivation

The front point of contact positions (D1 and D2 in Figure 3.1) are modelled as points of the curve of intersection of two perpendicular cylinders, where one cylinder is the pipe and the other cylinder is used to determine the positions of the wheels as shown in Figure 3.4. The equations for this curve of intersection are shown in (Equation (3.1)), (Equation (3.2)) and (Equation (3.3)), where; r_c is the radius of the small cylinder, r_p is the radius of the pipe and α is the circumferential angle of the smaller cylinder. Figure 3.4 shows 2 cylinders intersecting and the curves of their intersection. The curves represent a drive wheel position as the robot is rotated 360° in α on the top of the pipe.

$$X = b\sin(\alpha) \tag{3.1}$$

$$Y = b\cos(\alpha) \tag{3.2}$$

$$Z = \sqrt{r_p^2 + b^2\sin^2(\alpha)} \tag{3.3}$$
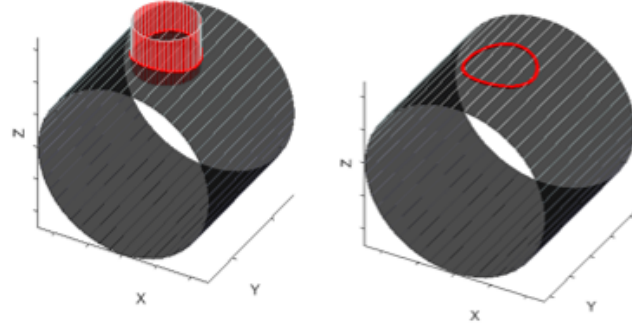
(a) Intersecting cylinders where the smaller red cylinder has a diameter equal to the wheel base (l)

(b) The curve of intersection between the two cylinders

Figure 3.4: a) Two cylinders intersecting b) Curves of intersection of cylinders showing possible wheel positions.

Assuming rotation around the centre of the drive wheels, this model holds for the drive wheel positions. At any rotation around the centre of the curve, the distance between the two drive wheels will always have an equal displacement. Therefore this ensures that the wheelbase geometry is conserved at all rotations. Equations (3.4), (3.5) and (3.6) calculate the X, Y and Z coordinates of each drive wheel, where n is 0 for the first drive wheel and 1 for the second.

$$D_Y = \frac{b}{2}\cos(\alpha + n\pi) \tag{3.4}$$

$$D_X = \frac{b}{2}\sin(\alpha + n\pi) \tag{3.5}$$

$$D_Z = \sqrt{\left\| r_p^2 - D_X^2 \right\|} \tag{3.6}$$

3.3 Rear Point of Contact Wheel Derivation

3.3.1 Sphere Cylinder Intersection Model

The cylinder-cylinder model does not hold for the rear contact position. This is due to the pitch changing as the points rotate around α. Figure 3.5 shows this by using a cylinder of constant radius is not an accurate representation of the real world. This is due to the cylinder-cylinder approach modelling the rear contact point as always being a fixed lateral length away from the centre of the front points. This is not the case as shown in Figure 3.5. The length of the robot is defined as the distance from the centre of the drive wheels and the castor wheel, and the curvature of the pipe means that the robot has a changing pitch as it rotates which is illustrated in Figure 3.5.

Figure 3.6 shows how the distance between the centre of the drive wheels and castor wheels (Y-axis) changes though a 360° α rotation (X-axis) using this cylindrical model, shown by the red line with he green line representing the actual fixed length. In the example shown in Figure 3.6 the maximum error of 4.6mm for a robot length of 125mm represents a 2.7% maximum error, however this error will propagate through to the simulation of the accelerometer measurements. Figure 3.7 shows the results of 3 different lengths and demonstrates that the percentage error in the length increases with the length. Initially, an attempt to vary the radius of the cylinder used to calculate the wheel position using sine functions was employed, however these still do not ensure that the length of the robot was conserved.
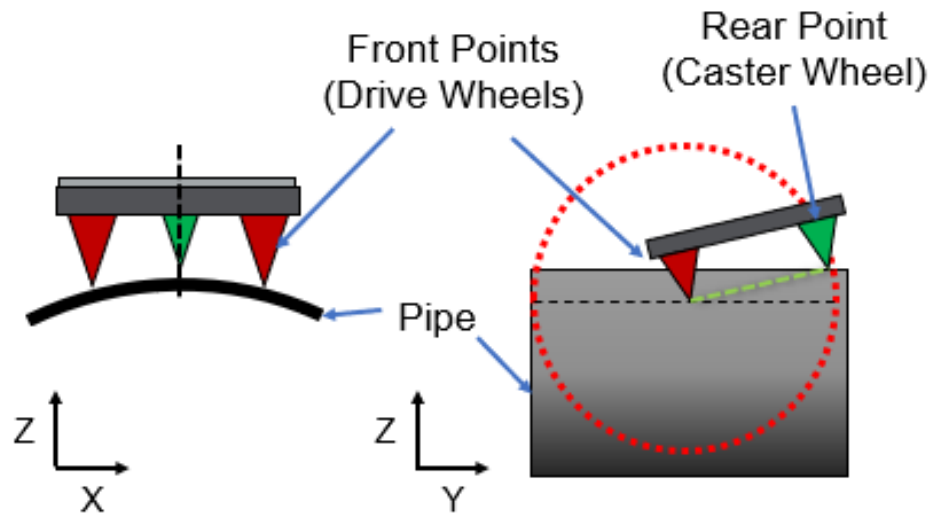
Figure 3.5: Castor wheel problem where a) Is looking down the axis of the pipe and shows the robot in line with the axis of the pipe b) show a side view of a).
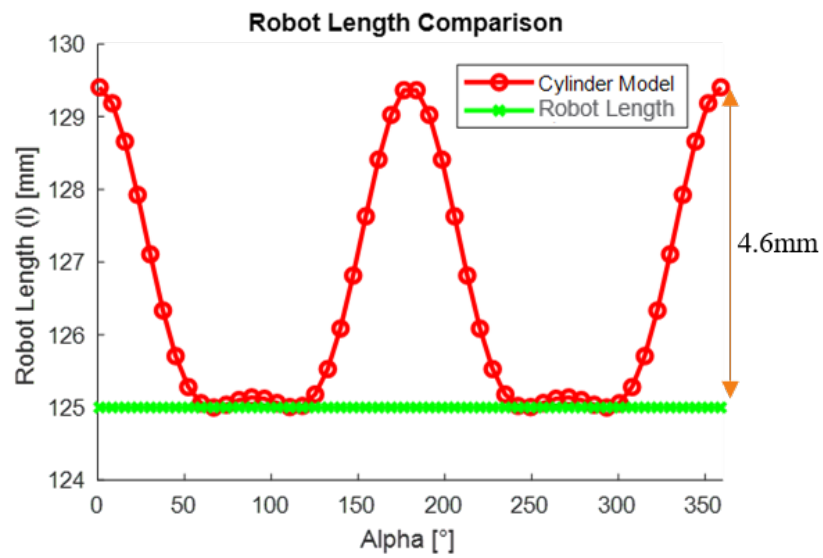
Figure 3.6: Graph showing how the length of the robot modelled by the cylinder model changes as the α angle is changed.
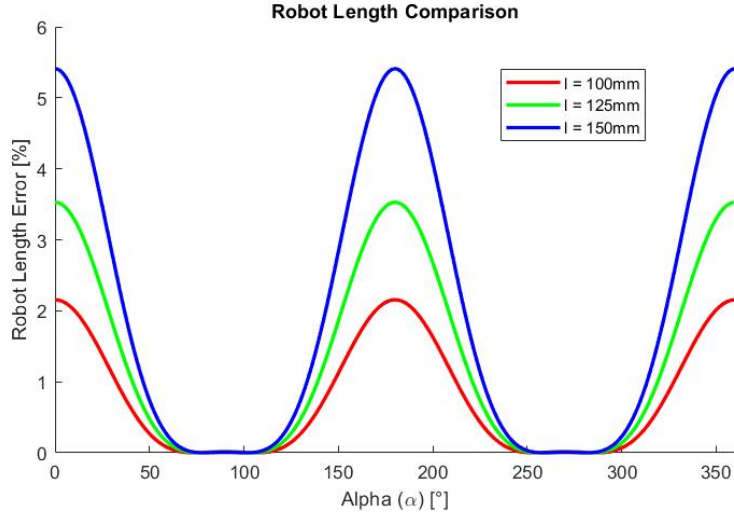
Figure 3.7: Graph showing the percentage error with varying length for a pipe radius of $250mm$

It should also be noted that the centre of the front points changes as a function of α as shown in Figure 3.5. To overcome this error a method of simulating the position of the castor while respecting the rigid body of the robot is presented. Placing a sphere [103] with a radius the same as that of the length at the centre of the drive wheels shows all the points which are equidistant from the drive wheel centre. Therefore, the length is conserved and the intersection between this sphere and the pipe represents the castor wheel positions as the robot rotates around α.

The first step in this method is to determine the position of the centre of the sphere shown in Figure 3.5. This was done taking the centre point between the two drive wheels. The α angle was set to find the circle of constant longitude of the sphere (great circle illustrated in Figure 3.8, shown in Figure 3.9a and takes into account the changing drive wheel centre position. There are four solutions for the intersection of the great circle of a sphere, shown in Figure 3.9b, and cylinder. Two of the solutions are real, representing the physical intersection points. The other two solutions are imaginary, however if the sphere is large enough so that the great circle intersects the cylinder four times, all four solutions become be real are represent the 4 physical intersection points.

70

The intersection points in Figure 3.9c and Figure 3.9d are found by calculating the latitudinal (ϕ) angle of the great circle at a given longitudinal angle (α) at the point of intersection. The equation for ϕ is (Equation (3.8)). This is then substituted into the parametric equations for a sphere shown in Equation (3.15), Equation (3.16) and (Equation (3.17)). The α and ϕ of a sphere are demonstrated in Figure 3.8 where all points with a constant α make up the great circle and (Equation (3.8)) calculates the ϕ angles at the intersection points. Equation (Equation (3.8)) is obtained by rearranging Equation (Equation (3.7)) for ϕ. This was achieved using both the Symbolic Python package (symPy) and the mathematical Maple software package. By setting the RHS of the equation to equal the radius of the pipe, the points of the sphere which are l distance from its centre which lie on the pipe surface can be determined.

$$r_p^2 = (l \sin(\varphi) \cos(\alpha))^2 + (l \cos(\varphi) + d)^2 \tag{3.7}$$

Rearranging for φ:

$$\varphi = \arctan2(A, B) \tag{3.8}$$

Where:

$$A = \pm \frac{1}{U} \sqrt{2d \sqrt{Q} + S} \tag{3.9}$$

$$B = \frac{1}{U}(-d \mp \sqrt{Q}) \tag{3.10}$$

$$U = l \sin(\alpha)^2 \tag{3.11}$$

$$S = V \sin(\alpha)^2 - 2d^2 \tag{3.12}$$

$$V = l^2 + d^2 - r_p^2 \tag{3.13}$$

$$Q = l^2 \sin(\alpha)^4 - V \sin(\alpha)^2 + d^2 \tag{3.14}$$

Parametric Equations of a Sphere:

$$X = l\cos(\alpha)\sin(\varphi) \tag{3.15}$$

$$Y = l\sin(\alpha)\sin(\varphi) \tag{3.16}$$

$$Z = l\cos(\alpha) + d \tag{3.17}$$

Where:

- d is the radial offset of the sphere centre from the centre of the cylinder defined by the position of the centre point between the drive wheels.

- l is radius of the sphere defined by the length of the triangle representing the 3 points of contact

- r_p is the radius of the cylinder/pipe

- α is the longitudinal angle of a point on the sphere determined by the orientation of the robot

- φ is the latitudinal angle of the great circle which at the intersection with the cylinder shown in Figure 3.8
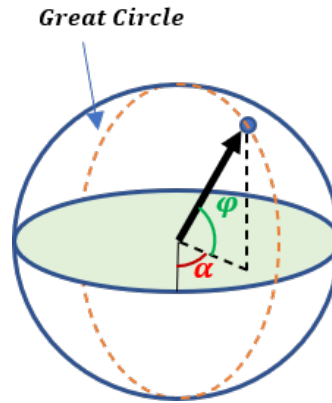
Figure 3.8: Angles of a Sphere
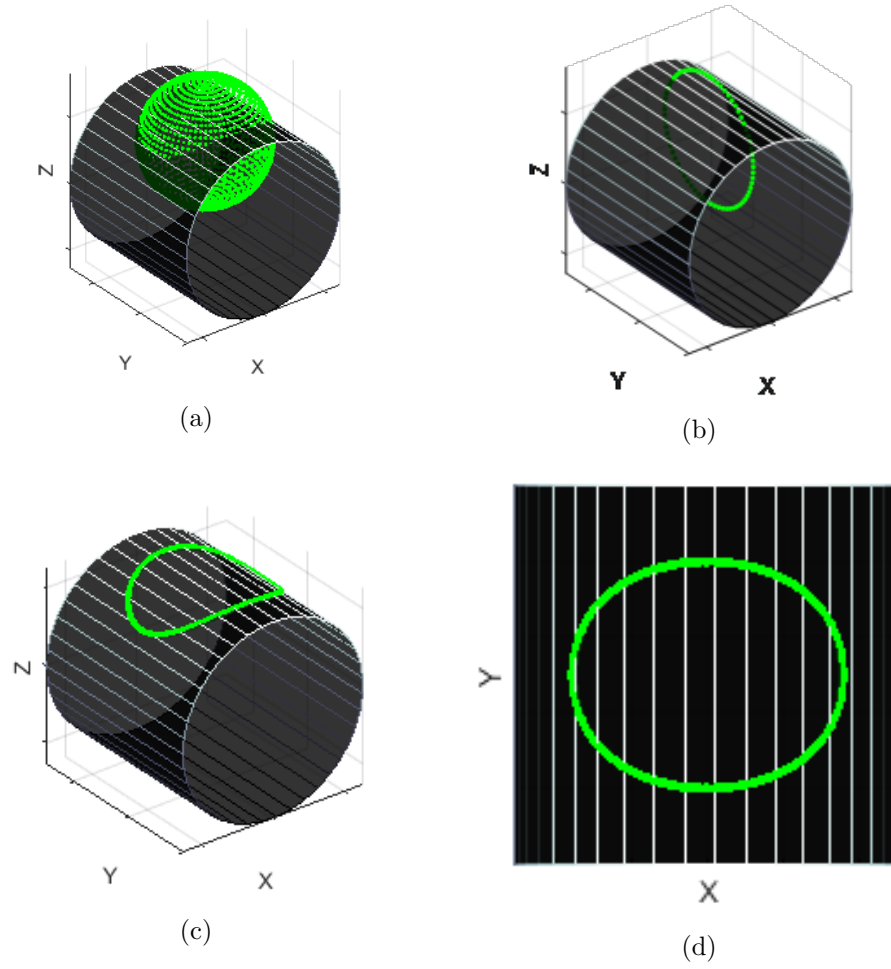
Figure 3.9: a) Modelled Sphere and pipe b) A great circle of the sphere at a given α angle c) and d) show the ellipse intersection equidistant from the centre of the drive wheels

Figure 3.11 shows the modelled length of the robot remains constant though a full 360° rotation in α and proves that this method holds compared to the cylinder-cylinder intersection model for the castor wheel.
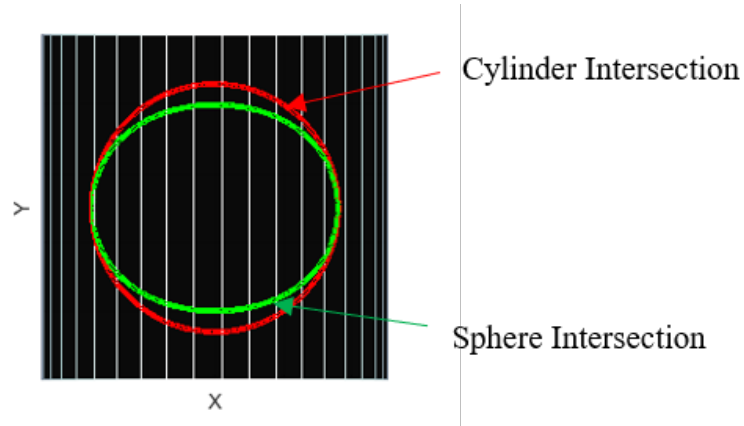
Figure 3.10: Example comparison of cylinder intersection (red) and Sphere intersection (green)
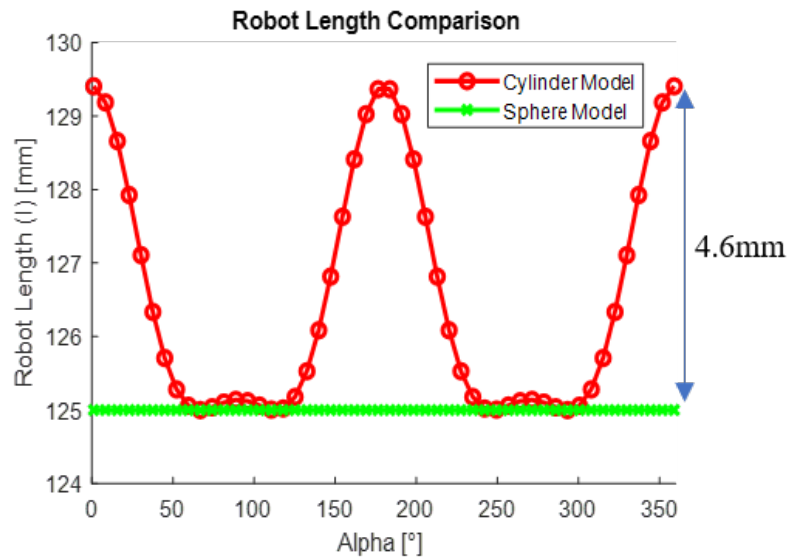
Figure 3.11: Example graph showing the relationship of the length of robot using cylinder-cylinder intersection (Red) the Sphere intersection (Green) though a 360° α rotation

Figure 3.10 compares the curves of the two intersections. From Figure 3.11 it is shown that the method of using a sphere intersection model removes the maximum error of 4.6 mm when modelling a robot length of 125mm. This error is present due to the centre of the drive wheels moving along the Z axis as the robot rotates and is not considered in the cylindrical model. This explains the bumps in Figure 3.11 at 90° and 180°.

This sphere intersection method could also be used to model the position of sensors attached at a fixed distance to the robot which is essential for creating defect maps for inspection purposes.

3.4   Accelerometer Readings Simulation

The expected 3-axis accelerometer readings can be determined from the 3 points of contact calculated in the previous sections.

From the 3 contact points, a plane is created and the normal vector to the plane is found. This vector is taken as the Z_{IMU} direction. The Y_{IMU} direction is found by taking the direction from the centre of the drive wheels to the left drive wheel and the X_{IMU} direction is the cross product of these two vectors. Gravity is taken to be acting in the negative Z_{Global} direction. Once all 3 accelerometer axes are determined, the gravity vector is separated into the 3 constituent vectors (X_{IMU}, Y_{IMU}, and Z_{IMU}) by calculating the angle between the vectors [104].Figure 3.12b shows an example simulation with the robot reference frame (X_{IMU}, Y_{IMU}, and Z_{IMU}) in relation to the global reference frame (X_{Global}, Y_{Global}, and Z_{Global}) and gravity (g).
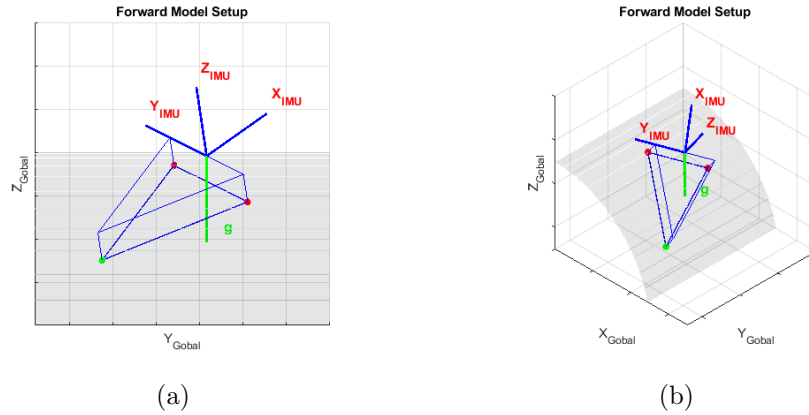
Figure 3.12: Example setup of IMU reference frame with respect to the global reference frame and gravity

3.5 Results

Figure 3.13 shows the combined intersection points of two cylinders to simulate the drive wheel points and a sphere-cylinder intersection to simulate the castor wheel points representing the curves which the wheels follow when a robot is rotating around the centre of its drive wheels.
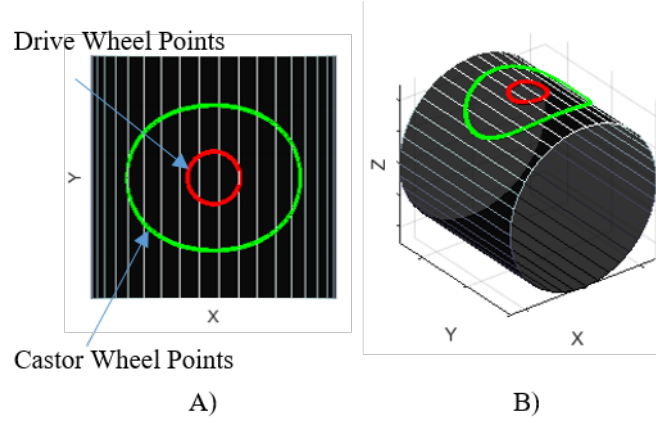
Figure 3.13: Cylinder and Sphere intersections for drive wheel and castor wheel points

Using Equations (3.4), (3.5) and (3.6) for the drive wheels and Equations (3.15),(3.16) and (3.17) for the castor wheel provides the 3 points of contact at any orientation. Once the 3 contact points are calculated, the Rodrigues rotation method [105] is applied to each point to rotate them around the pipe axis for a desired ω angle. This method can therefore be used to calculate the XYZ position of the 3 wheels a user defined α and ω. Figure 3.14 shows an example simulated robot at $\alpha = 45°$ and $\omega = 45°$.
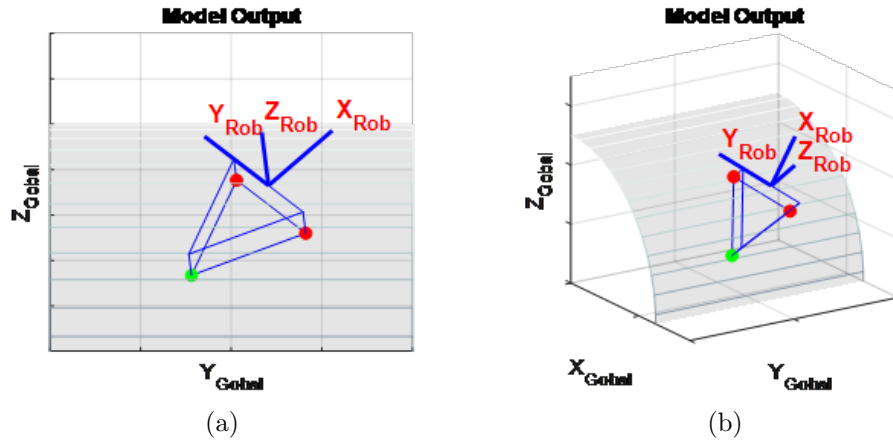
Figure 3.14: Example setup robot reference frame with respect to the global reference frame where the green points are the drive wheel points and the red point is the castor wheel contact point

Figure 3.15 and Figure 3.16 show examples of the 3-axis accelerometer readings (y-axis) simulated at 45° and 90° respectively while rotating though a full 360° in α (x-axis). From these graphs, the X and Y accelerometer patterns are offset by 90°. The pattern seen in the Acc Z values (yellow line), can be explained by the changing pitch of the robot previously described, which causes a slight oscillation of the Z axis thought the full α rotation.
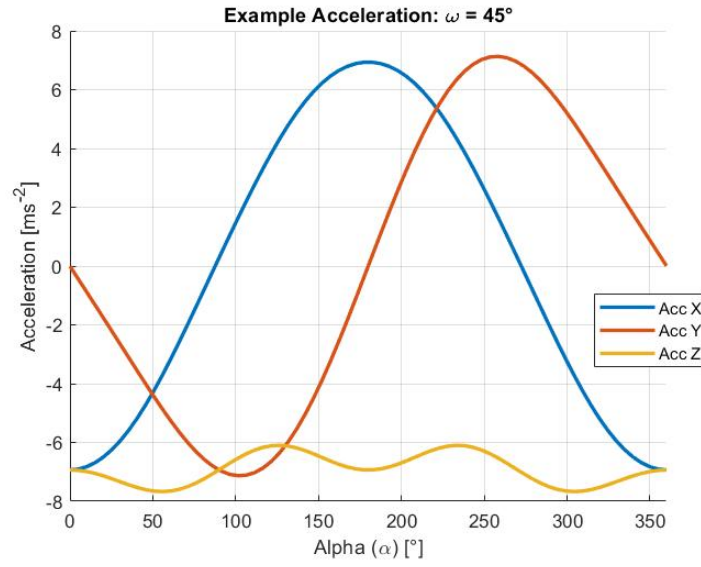
Figure 3.15: Plots showing the 3-axis acceleration in relation to α and $\omega = 45°$
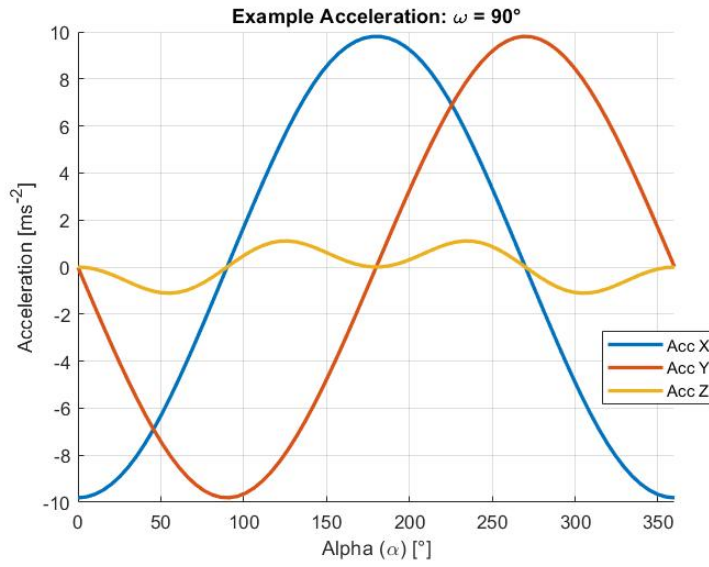
Figure 3.16: Plots showing the 3-axis acceleration in relation to α and $\omega = 90°$

Figure 3.17 shows how the X Y Z accelerometer readings from the simulation changes as both α and ω are varied. The X and Y accelerometer graphs are $\pi/2$ out of phase, as shown in the previous two figures. The graphs show the acceleration values changing between 9.81 and -9.81, represented by yellow and blue respectively, as the α and ω

angles change
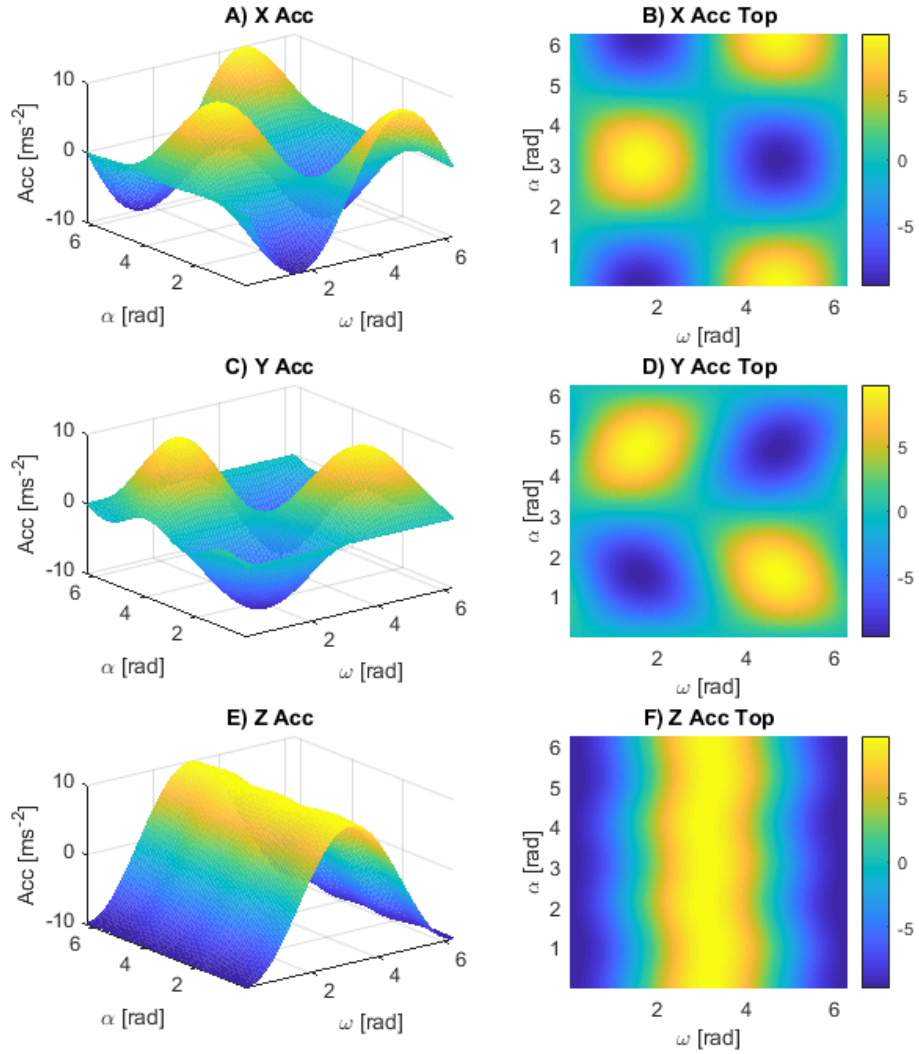
Figure 3.17: Plots showing the 3-axis acceleration in relation to α and ω

3.6   Model Comparison

A method of validating the model is to compare the output of the model with acceleration values at positions and orientations which are relatively straight forward to calculate manually, namely when the robot is at a positional angle of $\omega = 0°, 45°, 90°$ and

orientation angles $\alpha = 0°, 90°$. Example results are shown below and summarised in Table 3.1. The manual calculations were done using basic circular geometry and vector maths at positions and orientations where the geometry is easy to determine, such as on the top and side of the pipe with the orientation tangential to the axis of the pipe. Whereas the model output was calculated using the method above using the intersection between cylinders and spheres. The comparison shows that both the cases deliver the same output for these cases using two different mathematical methods. With these cases together with the conservation of the robot geometry for all possible cases as described previously, it can then be inferred the model can be used to successfully estimate the ideal world accelerometer values of a 3 wheeled robot on a pipe.

Table 3.1: Manual and model output calculations comparison

α and ω	Expected Output	Model Output
	X = 0	X = 0
$\alpha = 90°, \omega = 0°$	Y = 0	Y = 0
	Z = 9.81	Z = 9.81
	X = 9.81	X = 9.81
$\alpha = 90°, \omega = 90°$	Y = 0	Y = 0
	Z = 0	Z = 0
	X = 6.94	X = 6.94
$\alpha = 90°, \omega = 45°$	Y = 0	Y = 0
	Z = 6.94	Z = 6.94
	X = 0	X = 0
$\alpha = 0°, \omega = 90°$	Y = 9.81	Y = 9.81
	Z = 0	Z = 0

3.7   Discussion and Conclusion

This chapter describes a method that successfully models a three point-of-contact platform or robot on a cylindrical surface at any given known orientation and circumferential position, as well as simulate the 3-axis accelerometer values of the given position and orientation. This model assumes that the pipe surfaces is cylindrical, that gravity is considered constant and that the 3-points of contact are on a rigid body. This analytical model can be used for crawler robots on both the outside and inside of pipes as the mathematics remains the same. The required inputs are the desired α orientation, ω position angles and the geometry of the system. The geometry information required are the radius of the pipe, the wheel base of the robot and the length of the robot. This work can be extended to describe the wheel positions on an angled pipe and vertical pipes as well. This model has no projection inaccuracies as the geometry of the system is conserved at all positions and orientations. This model allows the relative robot reference frame to be determined in relation to the global reference frame and offers a method of referencing the absolute position of a three wheeled robot on a cylindrical surface in terms of the circumferential angle (ω) and the robot orientation (α). This work presents a measurement model for a 3-axis accelerometer which can be used as a forward model in a Forward/Inverse model problem, where the Forward Model presented outputs accelerometer readings from a known α and ω angle, while the Inverse Model would output the α and ω angle at known accelerometer measurements, as show in [106].

Chapter 4

Inverse Model and Optimisation

Three methods are presented to calculate the α and ω angles from accelerometer readings simulated using the Forward Model described in the previous chapter. These were:

- An analytical approximation: Discussed in Section 4.3.1, where a series of simultaneous equations are presented

- A parametric method: Where the lines of best fit are found following an assumed equation format and discussed in Section 4.3.2.

- A numerical optimisation method: Discussed in detail in this chapter and the method used in the remainder of this thesis.

It was found that a direct Inverse Model to this problem was not possible, and therefore an numerical optimisation method was deemed to be the most suitable. Figure 4.1 is repeated below to help describe the relationship between a Forward and Inverse model. The analytical approximation is used as the starting point in a least mean squared optimisation using the Forward Model as part of the cost function to obtain the correct angles. These methods are described in detail in the following sections.
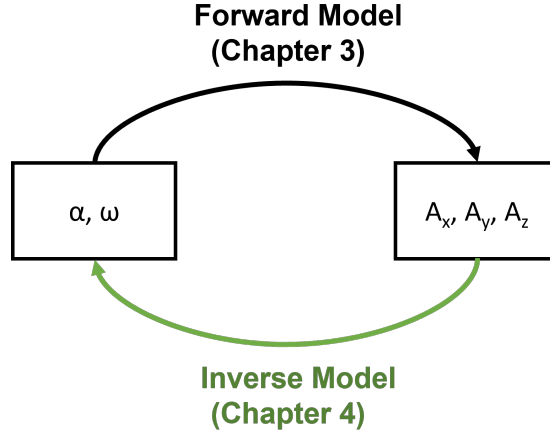
Figure 4.1: Schematic showing the relationship between the Forward Model and Inverse Model, where the Forward Model has inputs of (α, ω) and outputs (A_x, A_y, A_z) and vice versa for the Inverse Model.

4.1 Inverse Model

The aim of the Inverse Model is to go from the 3-axis accelerometer readings and calculate the α and ω angles. However, the Inverse Model for this problem is not a direct inverse of the presented forward model. This is because there is no unique solution to find the direction of the accelerometer axes from the 3-axis accelerometer readings alone and the Inverse model is mathematically ill-posed. This is the same reason yaw angles about the Z-axis can not be determined from acceleration values alone and magnetometers are required in IMUs to determine heading. This is because there is only 1 equation, and 3 unknowns, as shown in Equation (4.1), which represents a method of calculating the angle between two vectors (gravity vector and X accelerometer direction in this case), where:

- γ_{gx} is the angle between the chosen accelerometer axis in a global reference frame (in this case the X direction) which can be calculated from the accelerometer readings

- $X_{xg,yg,zg}$ are the x,y,z, components of the accelerometer X direction in terms of

83

the global reference, which need to be calculated in the Inverse Model

- $g_{xg,yg,zg}$ are the x,y,z, components of the gravity direction in terms of the global reference, which are known.

$$\gamma = \cos^{-1}\left(\frac{g_x x_x + g_y x_y + g_z x_z}{\sqrt{g_x^2 + g_y^2 + g_z^2}\sqrt{x_x^2 + x_y^2 + x_z^2}}\right) \qquad (4.1)$$

The simulated accelerometer readings (Ax, Ay and Az) are used to estimate the α and ω angles using Equation (4.2) and Equation (4.3). These equations are only approximations based on a simplified model using basic trigonometry and does not take into account the changing pitch of the robot as it rotates and the effects that this change in pitch has on the accelerometer readings. Figure 4.2 and Figure 4.3 show how these equations are formed.
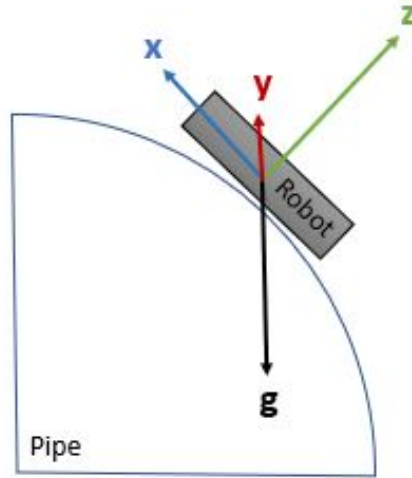
Figure 4.2: Schematic showing the vectors or the accelerometer and gravity
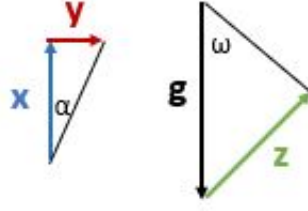
Figure 4.3: Finding the angles between the vectors to approximate α and ω

$$\omega = \sin^{-1}\left(\frac{A_z}{g}\right) \tag{4.2}$$

$$\alpha = \arctan2\left(A_y, A_x\right) \tag{4.3}$$

Where;

- Ax and Ay and Az are the X, Y and Z accelerometer readings in ms^{-2}

- g is the acceleration due to gravity in ms^{-2}.

Figure 4.5 shows the error in the ω angle though a full rotation in the α angle for a pipe of radius $r = 256mm$ at $\omega = 45°$. The maximum error in this particular case is $5°$. However, it should be noted that this error is a function of the pipe radius (r_p), and the robot geometry (b, l).
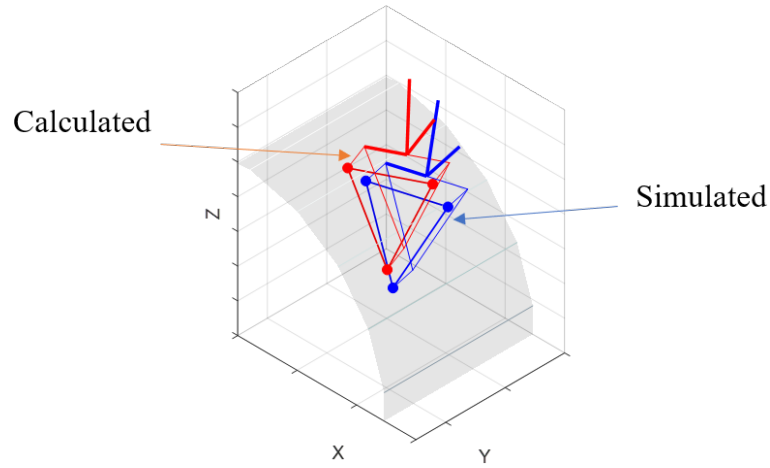
Figure 4.4: Blue: Simulated forward model position output from Chapter 3. Red: Output of Equation (4.2) and Equation (4.3) at estimated position
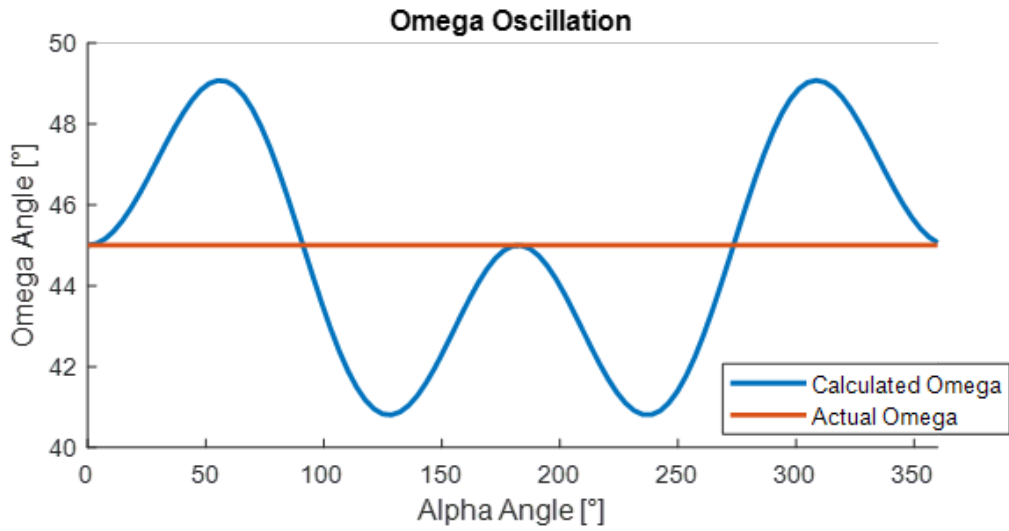
Figure 4.5: Example showing discrepancy between the calculated ω (blue) and the simulated ω (red) while simulating a full $360°$ rotation in the α angle for a pipe radius of 250mm

When the output of the above equations is plotted against the forward model, shown in Figure 4.5, it is noticed that there is a significant error in the calculated angles compared to the simulated ones as seen in the example given in Figure 4.4. This error is a result of Equation (4.2) and Equation (4.3) being approximations which do not

take into account the change in pitch of the robot as it rotates in α, which is a function of the geometry of the robot and the radius of the pipe. This error is present as the equations used in the Inverse model are only approximations and are used due to the ill-posed nature of the problem.

Futher to this, there are also cases where different α and ω angles will give the same accelerometer values. This is due to the two sides of the pipe and the accelerometers inability to determine yaw on its own. For each angle combination on one side of the pipe, there is a corresponding set of angles on the other side of the pipe which have the same accelerometer outputs. An optimisation approach is presented and is deemed more appropriate compared to the other methods presented as it obtains more accurate results and is a more generalised solution.

4.2   Optimisation Numerical Approach

To overcome the discrepancy between the calculated and the simulated robot angles, an optimisation method is presented. A least mean squared error minimisation technique is used to achieve this. The steps taken are described as follows:

1. Calculate α_{calc} and ω_{calc} from accelerometer readings.

2. Simulate accelerometer readings from α_{calc} and ω_{calc} using the forward model.

3. Apply least mean squared error minimisation optimisation between the original accelerometer readings (Step 1.) and the simulated accelerometer (Step 2.) by varying α_{calc} and ω_{calc}.

This process is outlined again in 4.6, which shows a Forward/Inverse model approach with an optimisation step. The forward model is used to simulate the accelerometer readings with given ω and α angles. The inverse model is used to give an approximation of the ω and α angles from the 3 axis accelerometer data. An optimisation approach is then used between the initial simulated accelerometer measurements and the simulated

accelerometer measurements at the calculated ω and α angles.
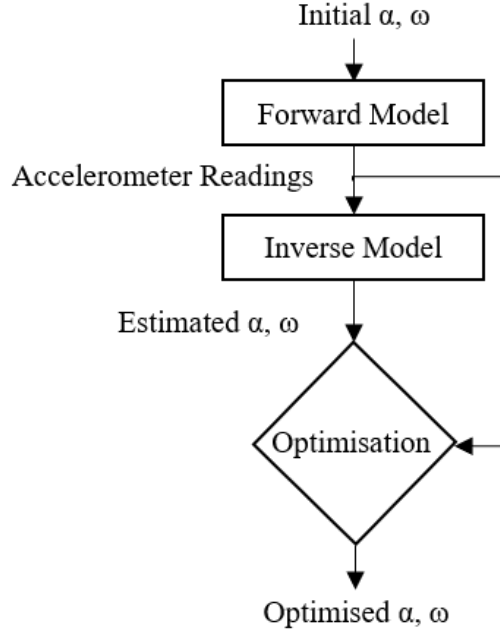
Figure 4.6: Schematic showing the processes used in this work

4.2.1   Least Mean Square Error Minimisation

The Levenberg-Marquardt (LM) algorithm was used to converge to the minimum error. LM is an iterative method that is used to determine a minimum of a multivariate function which is expressed as the sum of squares of a non-linear and real-valued function [107]. This discrepancy between the sum of the squares is sometimes also referred to as a residual. The LM algorithm preforms an optimum interpolation between the Taylor series and gradient iterative methods based on the likelihood of the Taylor series giving an adequate representation of the non-linear system [108].

Equation (4.4) is the minimised cost function. The initial point of the optimisation are the values given by Equation (4.2) and Equation (4.3).
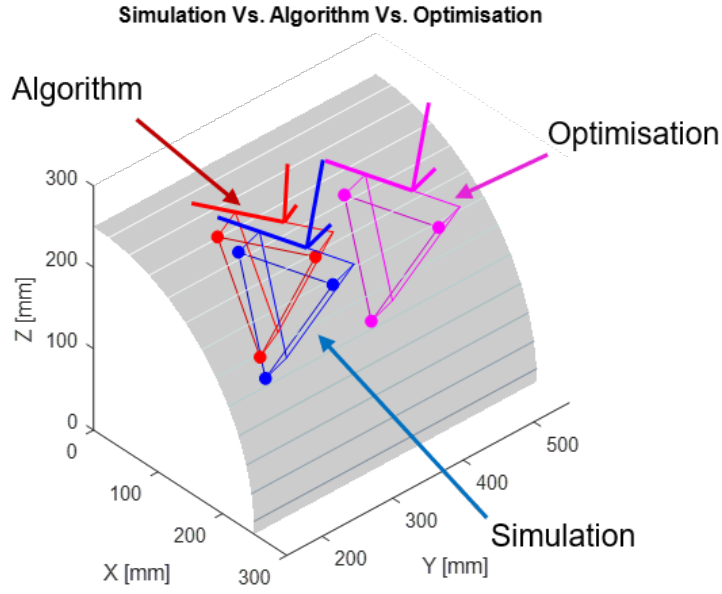
Figure 4.7: Comparison between the simulated (blue), estimated (red) and optimized (pink) robot positions

$$f(\alpha, \omega) = (A_{x_{opt}} - A_x)^2 + (A_{y_{opt}} - A_y)^2 + (A_{z_{opt}} - A_z)^2 \qquad (4.4)$$

This method returns an α and ω angle which outputs the same accelerometer data that are used in the forward model to simulate the corresponding acceleration readings.

A comparison between the simulated, calculated and optimised robot positions is shown in Figure 4.7, where the optimised robot position is shifted along the Y axis. This is done as the optimised position is the same as the simulated position as seen with the values of the angles in Table 4.1. This shows that in a perfect situation where the pipe is perfectly round and horizontal, a perfect accelerometer and flat robot, the optimisation solution converges to the exact values. It should be noted that if the initial angle guesses are on the opposite side of the pipe to the accelerometer readings, the optimisation will converge to the wrong solution. Therefore, it is useful to know which side of the pipe the optimisation needs to start with for the initial guess.

Table 4.1: Manual and model output calculations comparison

	α	ω
Forward Model Input	45°	45°
Analytical Approximation	41.5°	49.8°
Optimisation	45°	45°

Utilising an optimisation solution requires an initial guess of the state for the iterative process to start. The closer the initial guess to the minimum solution, the quicker the optimisation converges. A threshold value of $1e^{-6}ms^{-2}$ difference between the Forward Model output and accelerometer input values was used to ensure that the the accuracy of the converged values. This value is very small and in terms of the acceleration values, it is statistically insignificant. Table 4.2 illustrates this, showing how using the calculated analytical approximation converges after 7 iterations, whereas using an arbitrary guess can take longer, in this case 12 iterations. Table 4.3 shows the time taken for both these cases to converge using an XPS 15 laptop and Matlab. The time difference is not significant as the bulk of the processing time has been reduced due to the analytical nature of the forward model.

Table 4.2: Convergence Table

| | | Residuals |
| Iteration | Arbitrary Guess | Approximation Analytical Guess |
	$\alpha = 160° \ \omega = 160°$	$\alpha = 39.5° \ \omega = 39.2°$
1	130074.000000	1.71319000
2	5473.190000	0.13419200
3	539.004000	0.01006110
4	337.347000	0.00063344
5	130.108000	0.00003914
6	30.137100	0.00000243
7	3.290690	0.00000015
8	0.208168	–
9	0.012175	–
10	0.000739	–
11	0.000046	–
12	0.000001	–

Table 4.3: Convergence Time Table for $\alpha = 45° \omega = 45°$

| | Time to Convergence | |
| Iteration | Arbitrary Guess | Analytical Guess |
	$\alpha = 160° \ \omega = 160°$	$\alpha = 39.5° \ \omega = 39.2°$
Time Taken [s]	0.256	0.248

4.3 Alternative Approaches

There are other methods of finding a suitable Inverse model. The main approaches investigated were a series of simultaneous equations to solve for the wheel positions, and a parametric method to correct the initial estimates. Both are presented below.

4.3.1 Simultaneous Equations

A method which was thought to be a logical step in determining the Inverse model was to solve a system of 9 simultaneous equations to obtain the 3 dimensional coordinate points of the 3 wheel contact points.

The following series of 9 simultaneous equations (4.5) - (4.13) describe the system, linking the XYZ output of the accelerometer with the 3 points of contact on the pipe surface. It is not practical to solve these directly using the Gröbner basis [109] as the result was a polynomial with an order in excess of 100. However, they are included here for completeness. Where:

- Equation (4.5) sets the robots position along the pipe to 0

- Equations (4.6 – 4.8) ensure that the points of contact lie on the curved surface of the pipe

- Equations (4.9 – 4.11) set the geometry of the robot

- Equations (4.12 – 4.13) ensures that all the points of contact lie on the same plane

- D1, D2 and C are the geometries illustrated in Figure 3.1. X, Y and Z are the coordinates taken from the centre of the pipe

- (X_{D1}, Y_{D1}, Z_{D1}), (X_{D2}, Y_{D2}, Z_{D2}) and (X_C, Y_C, Z_C) are the coordinates of the contact points and the variables to be solved for

- n is the unit vector normal to the plane of the accelerometer calculated from

accelerometer readings

$$\frac{1}{3}(Y_{D1} + Y_{D2} + Y_C) = 0 \tag{4.5}$$

$$X_{D1}^2 + Z_{D1}^2 = R^2 \tag{4.6}$$

$$X_{D2}^2 + Z_{D2}^2 = R^2 \tag{4.7}$$

$$X_C^2 + Z_C^2 = R^2 \tag{4.8}$$

$$(X_{D1} - X_{D2})^2 + (Y_{D1} - Y_{D2})^2 + (Z_{D1} - Z_{D2})^2 = b^2 \tag{4.9}$$

$$(\frac{1}{2}X_{D1} + \frac{1}{2}X_{D2} - X_C)^2 + (\frac{1}{2}Y_{D1} + \frac{1}{2}Y_{D2} - Y_C)^2 + (\frac{1}{2}Z_{D1} + \frac{1}{2}Z_{D2} - Z_C)^2 = l^2 \tag{4.10}$$

$$\overrightarrow{D1 - D2} \cdot \frac{\overrightarrow{D1 + D2}}{2} - C = 0 \tag{4.11}$$

$$n(1)X_{D1} + n(2)Y_{D1} + n(3)Z_{D1} = n(1)X_C + n(2)Y_C + n(3)Z_C \tag{4.12}$$

$$n(1)X_{D2} + n(2)Y_{D2} + n(3)Z_{D2} = n(1)X_C + n(2)Y_C + n(3)Z_C \tag{4.13}$$

4.3.2 Parametric Correction

A parametric investigation is conducted to try and determine the relationship between the error in the α and ω angles and the radius of the pipe at a fixed robot geometry. Figure 4.5 shows an example of the oscillation in the ω angle as the robot is simulated to rotate $360°$ in α at an ω position of $45°$. Figure 4.8a shows the amplitude of oscillation in ω for different pipe radii simulated for the same α rotation and Figure 4.8b shows the correction needed in the α angle to match the original input.
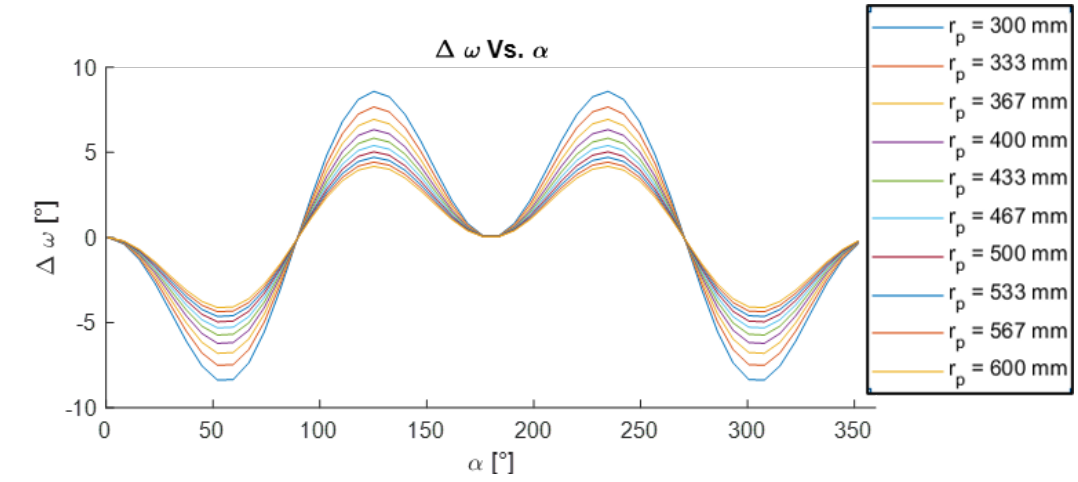
(a) Calculated ω values with respect to changing pipe radius (r_p)
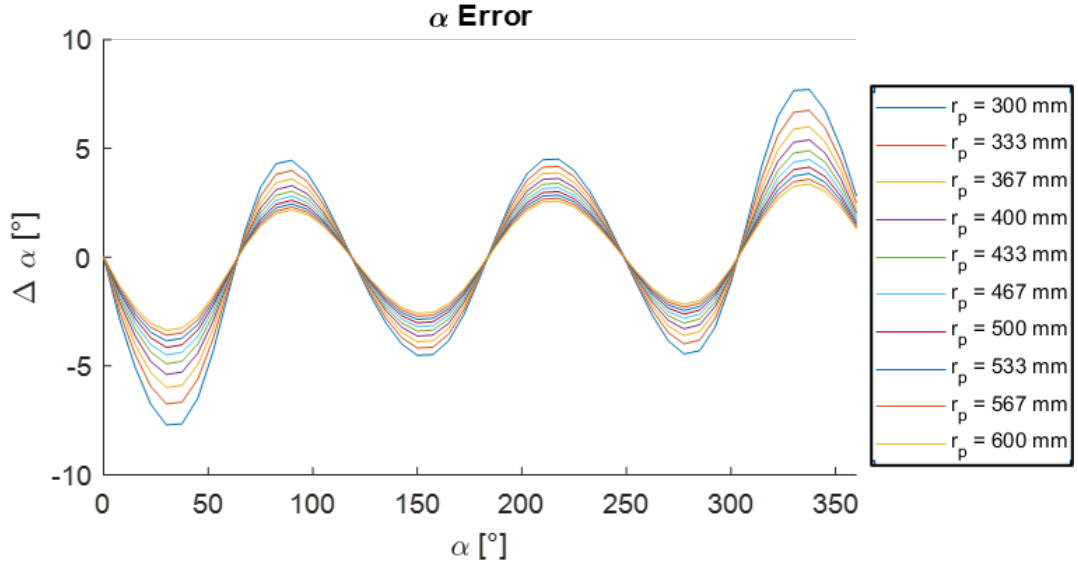
(b) Calculated α values with respect to changing pipe radius (r_p)

Figure 4.8: A) Two cylinders intersecting B) Curves of intersection of cylinders showing possible wheel positions

Equation (4.2) and Equation (4.3) are modified to Equation (4.14) and Equation (4.15) where C_{1-4} are correction factors. These factors are calculated by using a line fitting function to determine the C values which will give the closest fit to the lines in Figure 4.8a and Figure 4.8b for each pipe radius tested and shows how the oscillation decreases as the pipe radius increases. A polynomial is then fitted to these values to produce an equation for C_1, C_2, C_3 and C_4 as a function of pipe radius rp.

$$\omega_{cor} = \cos^{-1}\left(\frac{A_z}{g}\right) - C_1 \sin(\alpha)\sin(2\alpha) \tag{4.14}$$

$$\alpha_{cor} = \arctan2(A_x, A_y) - C_2 \sin(3\alpha) + C_3 \cos(C_4\alpha) \tag{4.15}$$

The wave of oscillation in 4.5 is a function of the robot geometry and the radius of the pipe. Therefore, if the robot geometry is known, a parametric study investigating how the pipe radius affects the oscillation can be done. To find the correction factors the following steps were taken:

1. Simulate 360° rotation of robot in the α orientation and simulate accelerometer readings

2. Calculate angles from accelerometer readings

3. Fit line of best fit to the oscillation to find an appropriate correction factor

4. Increase the radius of the pipe and repeat

5. Plot the calculated correction factors for each pipe radius and find the line of best fit

This method allows for the parametric analysis to be done only once for a given robot geometry. The calculated relationship of correction factors to pipe radius can then be used in practice. Figure 4.9 shows an example the calculated correction factors for different pipe radii. It is shown that an exponential line fit is much more similar to the parametric line. Even so, it is still not a perfect fit and therefore there will discrepancies between the real angles and the angles calculated using this method.
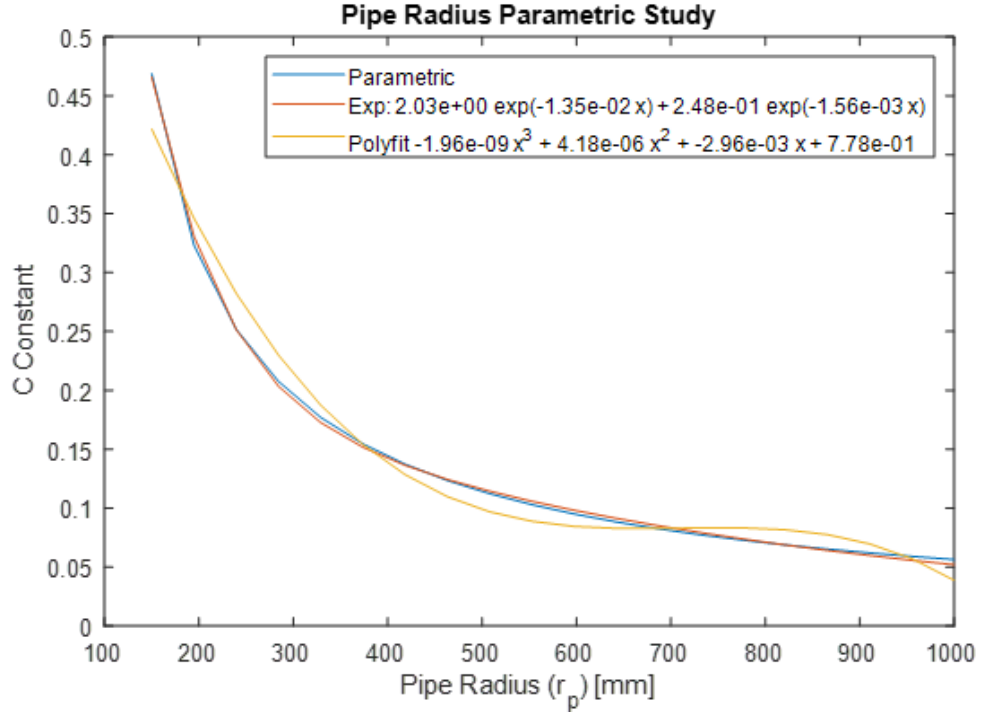
Figure 4.9: Determining the relationship between the correction factor and pipe radius

Figure 4.10a shows the position of the robot calculated when using Equation (4.2) and Equation (4.3) compared to the simulated forward model position. Figure 4.10b shows the robot position corrected using the correction factor found using a parametric study, where a difference in the α angle can still be seen. Figure 4.10c shows the comparison between the position calculated corrected for both the α and ω angles and the forward model.Figure 4.10c shows that using the correction factors found using a parametric study can accurately correct the analytical approximations made using Equation (4.2) and Equation (4.3). It should be noted that Figure 4.10c appears to show good agreement, there is a $< 2°$ error in both angles.

(a) Uncorrected

(b) ω Corrected

(c) α and ω Corrected
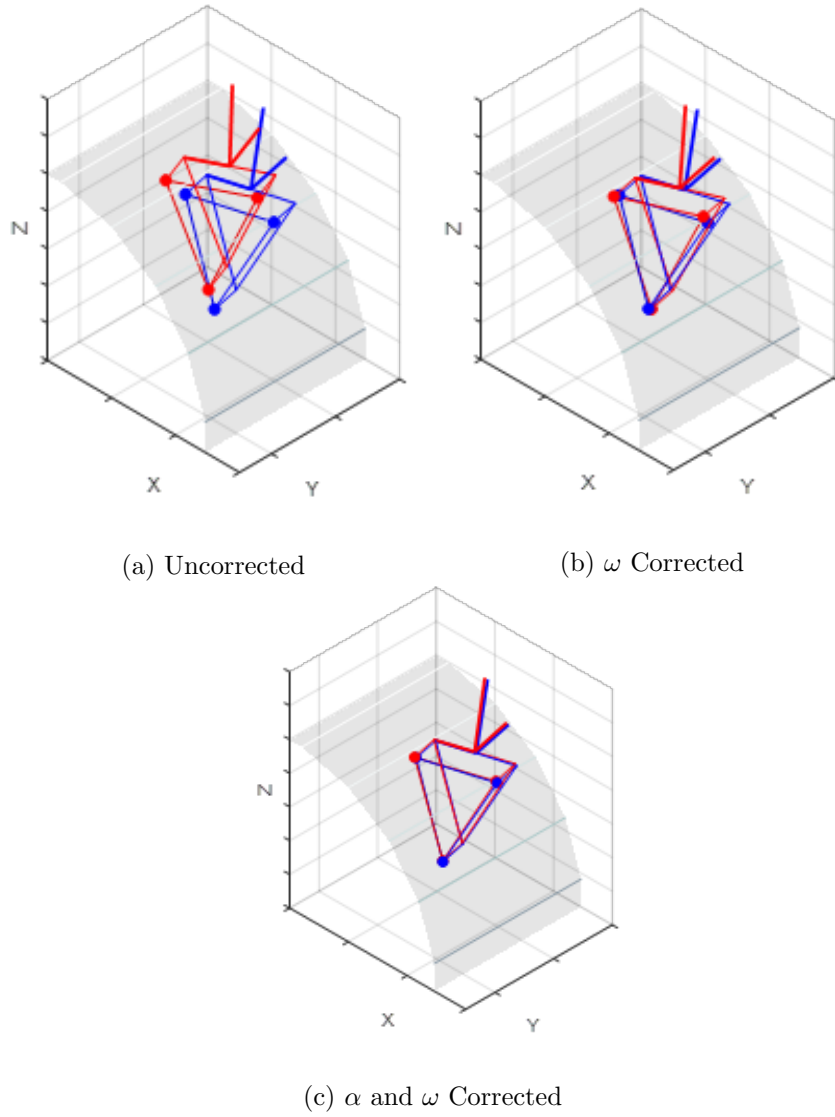
Figure 4.10: Showing plotted example at $\omega = 45°$ and $\alpha = 45°$ corrected and uncorrected

The parametric method above corrects the α angle to $42.9°$ and the β angle to $42.2°$, representing a $2.1°$ and $2.8°$ error compared to the ideal simulated case respectively. While this method is workable, it requires a parametric study to be completed for each robot/pipe geometry.

4.4 Conclusion

An example comparison of the methods presented above is shown in Table 3.1. Using the accelerometer readings simulated using the Forward Model developed, the optimisation approach minimises to the values entered into the Forward Model and is the most accurate method presented. While the numerical method is more computationally intensive with an approximate calculation time of 0.25s in Matlab using a Dell XPS 15 laptop, this is still a high enough rate to provide meaningful positional updates. Each of the methods investigated have pros and cons and are summarised in Table 4.5. This method is examined via physical validation in the next chapter.

Table 4.4: Manual and model output calculations comparison

	α	ω
Forward Model Input	45°	45°
Analytical Approximation	41.5°	49.8°
Parametric Correction	42.9°	42.2°
Optimisation	45°	45°

Table 4.5: Summary of pros and cons of the methods presented above

Method	Pros	Cons
Analytical Approximation	• Quick due to the simple equations used	• Not very accurate as the equations overly simplify the model of the system
Parametric Correction	• More accurate compared to analytical approximation • Once correction factors have been determined, calculation of the corrected values is relatively quick	• Parametric study needs to be completed to create a lookup table • Study needs to be completed for each desired robot geometry • There is still discrepancy between the corrected values and the input values
Optimisation	• Most accurate of the methods presented	• More computationally intensive

Chapter 5

Experimental Validation

The aim of this chapter is to prove that the algorithm consisting of the Forward Model, Inverse Model and Optimisation presented previously holds in reality and would satisfy the industrial partners requirements of having a $< 5°$ error. This was achieved by building a test rig with an attached accelerometer and placing it on a pipe. The diameter of the pipe used was nominally 20 inch and measured to be $D = 507mm$. The orientation and position data was captured using a photogrammetry system. The maximum error between the pose data collected from the photogrammetry system and calculated from the accelerometer was found to be $\Delta\alpha = 3.40°$ and $\Delta\omega = 4.17°$.

Unfortunately, the closure of university labs due to the corona virus restricted the time available to further validate this work. In an ideal situation, multiple pipe diameters would be used in the validation process.

5.1   Data Collection

Experiments were conducted to check the validity of the mathematical models developed and to determine the suitability of this method for real world applications.

5.1.1 Experimental Setup

Accelerometer Calibration Check

An MTi-300 AHRS (Attitude and Heading Referencing System) Xsens IMU unit, shown in Figure 5.1 was used for the experimental validation [110]. According to the datasheet, in static conditions, there is an error of up to $0.2°$ in the calculated angle and the sensitivity of the accelerometer is $40mVg^{-1}$ with the resolution being $0.0067ms^{-2}$. This highly accurate IMU was chosen to try an remove doubt over the accuracy of the accelerometer readings. The device also consists of a gyroscope which can potentially be used in future work. A Leica laser tracker AT901 measurement system [17] was used to test the accuracy of the accelerometer readings. The Leica laser tracker AT901 is a methodology based laser scanner which can measure the position of a retro reflector in free space to accuracies of $\pm0.2\mu m$ [111]. The accuracy of the accelerometer readings was tested by using the Leica system to determine the angle of a $45°$ wedge. The Leica system was used to determine the planes of both sides of the wedge, and from this, determine the actual angle of the wedge. Figure 5.3 shows a plot of the data points collected with the laser tracker and the angle between the 2 planes. The angle of the wedge determined by the Leica laser system was found to be $45.416°$. The accelerometer was placed on angled side of the wedge, while placed on a flat surface measured using a spirit measure, at different orientations, approximately 0, 45, 90, 135 and 180 from the axis of the wedge, and the roll and pitch were calculated from the accelerometer readings. An illustration of this is shown in Figure 5.2. The plane of the accelerometer was then calculated and the angle of this plane is taken as the wedge angle. The results in Table 5.1 showed a maximum discrepancy of $0.138°$ when calculating the angle using the accelerometer. This is in line with the accuracies stated in the datasheet of the accelerometer.

Figure 5.1: MTi-300 AHRS [110]
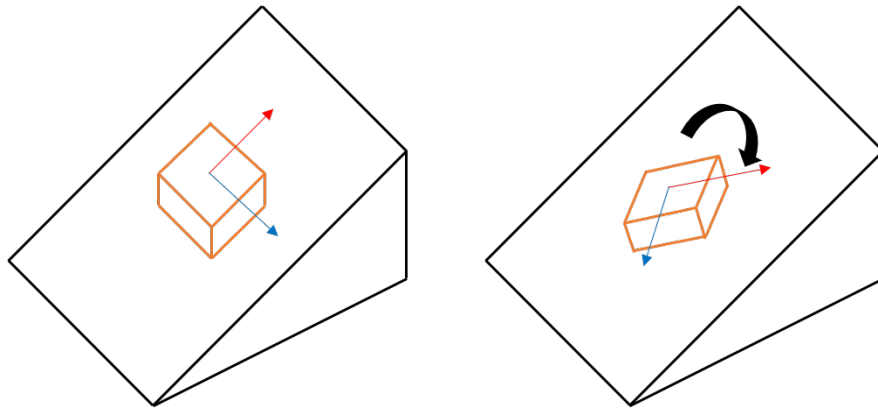
Figure 5.2: Schematic showing part of the process checking the calibration of the accelerometer
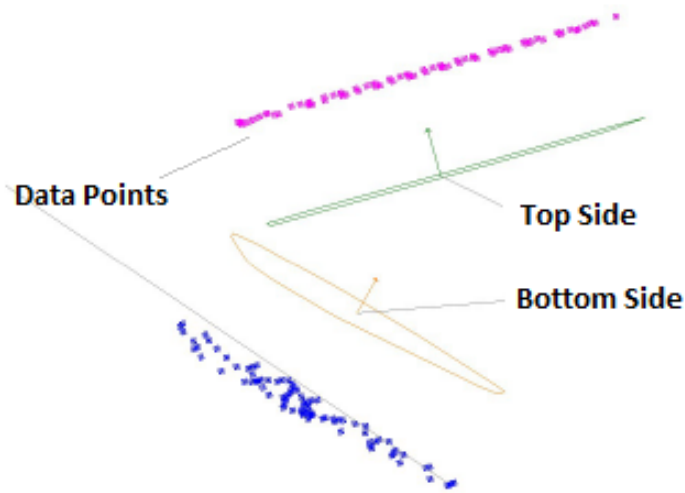
Figure 5.3: Results taken from the Leica AT901 using SpatialAnalyser software showing the point clouds captured for both sides of the angled wedge

Table 5.1: Angles Calculated from Accelerometer Readings for Calibration

Approximate Orientation [°]	Calculated Wedge Angle [°]	Wedge Angle Error [°]
0	45.46	0.047
45	45.55	0.138
90	45.50	0.087
135	45.48	0.059
180	45.39	0.028

Test Rig Design and Manufacture

A test rig was manufactured with 3 points of contact. Ring magnets were attached to the test rig to hold it in position on the metal pipe. Figure 5.4 shows a schematic of the base plate of the test rig. The base plate was manufactured from steel, Figure 5.6 shows the manufactured rig used for the experimental validation and Figure 5.5 shows the basic dimensions of the rig.
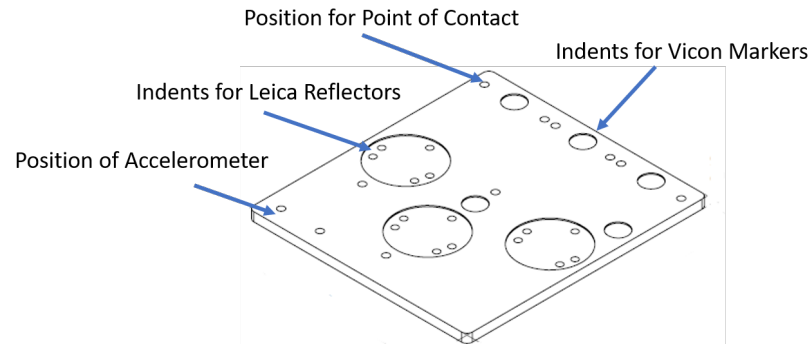
Figure 5.4: Test Rig Base Plate Schematic
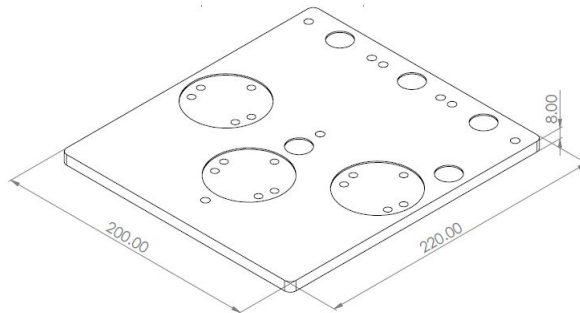
Figure 5.5: Test Rig Base Plate Outer Dimensions
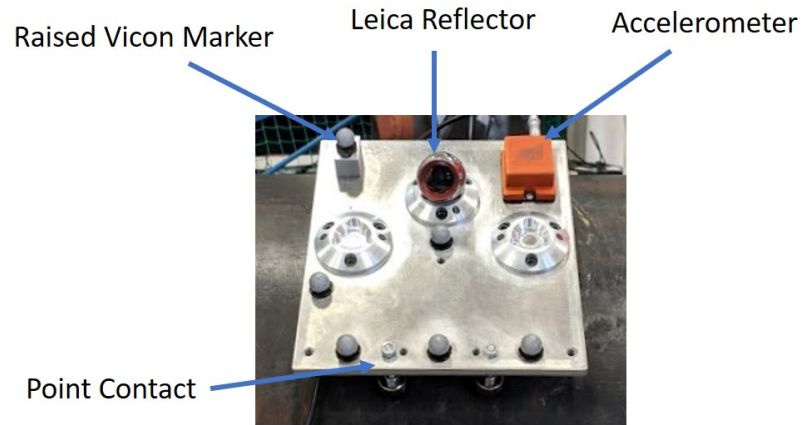
Figure 5.6: Image of the Manufactured Test Rig

Vicon Photogrammetry System

A Vicon MX Giganet system utilising 12 Vicon T160 cameras was used to measure ground truth position and orientation of the test rig, as done in previous studies [97], [20], and was calibrated before use. The Vicon MX Giganet system is a photogrammetry 6 DOF motion capture system which utilizes several cameras to track the position and orientation of an arrangement of retro-reflective markers.

Summan et al [98] thoroughly describes the process of calibrating the system and this procedure was followed for this experimental validation. Figure 5.7 shows a schematic of the photogrammetry system used for illustration purposes. The system was set up in controlled lab conditions. Summan et al [98] showed that the error associated between the measured Vicon position and the real position was an average of 1.48mm using the active calibration method employed in this work.
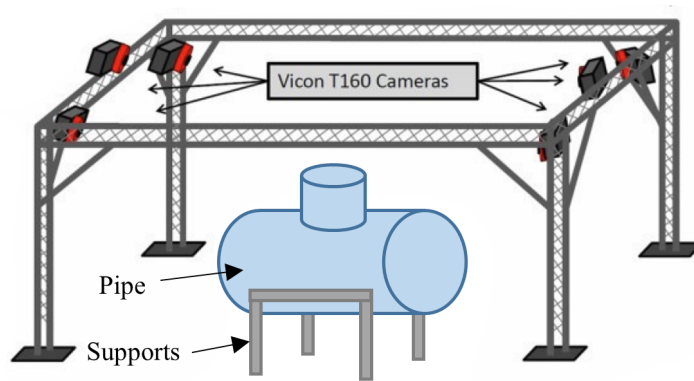
Figure 5.7: Schematic of experimental apparatus showing the frame with Vicon cameras, measurement volume and pipe, image adapted from [112]

Pipe

The pipe used for testing purposes was a steel pipe available in the lab and shown in Figure 5.8. The main horizontal pipe had a adjoining smaller orthogonal pipe connected by a saddle weld. Figure 5.7 shows a schematic of the pipe setup in the measurement volume of the Vicon photogrammetry system. The outer diameter of the pipe was measured to be 507mm with the total length 1.53m. This was used as it was the only available sample of suitable size at the time. Covid lock down prevented the ordering of other pipes.

Figure 5.8: Schematic of experimental apparatus showing the frame with Vicon cameras, measurement volume and pipe

Experimental Method

XYZ positional data and the orientation in quaternions were recorded at a rate of 100Hz for 3 seconds. The accelerometer on the IMU was sampled at a rate of 1kHz for 3 seconds. The IMU used in for this experiment an off the shelf XSens MTi-300 [110].

Two geometries were tested, both with a length (l) of 180mm and the two wheel bases (b) being 180mm and 70mm. The steps taken are detailed below:

1. Calibrate measurement volume as detailed in [98]

2. Find centre of pipe in Vicon coordinate system. This was achieved by placing a number of Vicon markers on the outside of the pipe. The positions of these markers were used to fit a circle, with the circle centre taken as the pipe centre.

3. Place test rig on pipe

4. Capture Vicon position and orientation data using Vicon software

5. Capture 3-axis accelerometer output using MTi software

6. Change position and orientation of rig and repeat steps 3-5.

To determine the centre point of the pipe, a series of Vicon markers were placed on the circumference of the pipe. The positions of the individual markers in the Vicon coordinate system were recorded and a circle of best fit was introduced. The centre point of this circle was taken as the position of the centre axis of the pipe.
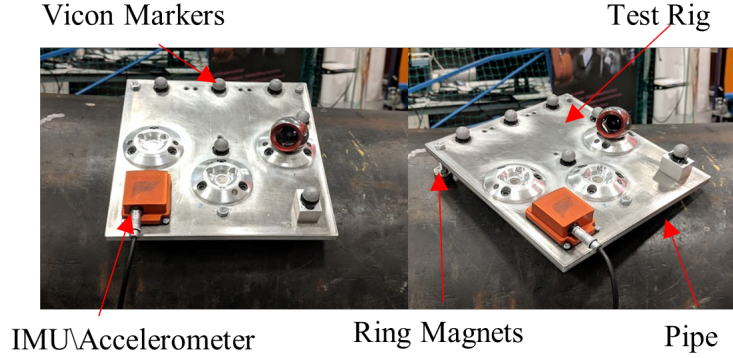
Figure 5.9: Rig setup showing the 3 points of contact with the Vicon markers and Accelerometer

5.2 Experimental Results

The experimental results are shown in Table 5.5, Table 5.6, Figure 5.16 and Figure 5.17. From these results, it can be seen that the optimisation method significantly improves on the analytical approximation algorithm. The optimisation reduces the maximum error from $16.4°$ to $3.4°$ in α and from $6.42°$ to $4.17°$ in ω for a base of $180mm$. For a wheel base of $70mm$ the error was reduced from $12.6°$ to $2.37°$ in α and from $7.23°$ to $2.5°$ in ω. Figure 5.16 and Figure 5.17 show examples of the discrepancy between the algorithm and optimisation position and orientation angles calculated using the accelerometer data with the angles recorded using the Vicon system.

An example of the raw accelerometer data recorded is shown in Figure 5.10. Table 5.2 show the mean, range and variance of this collected data. These values are small and show that the data collected over the sampling period is precise with little variation.

Calculating the ω and α angles from this raw data results in Figure 5.11 and Figure 5.12. Calculating the angles using the raw photogrammetry values results in Figure 5.13, and again shows low variability. Table 5.3 shows the example average, range and variance for the angles calculated from raw data.
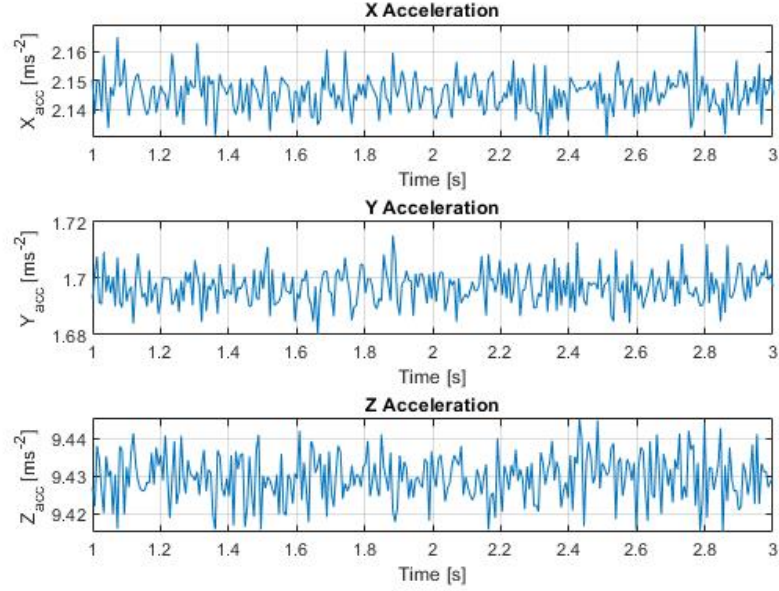
Figure 5.10: Graphs showing an example of the raw data taken over 3 seconds at 100Hz in the X,Y and Z axes for a single trial

Table 5.2: Table showing the mean, range and variance of the raw accelerometer data taken for the single trial shown in Figure 5.10

	X_{acc}	Y_{acc}	Z_{acc}
Mean	2.15	1.70	9.43
Range	0.0392	0.0351	0.0300
Variance	0.0000370	0.000038	0.000041
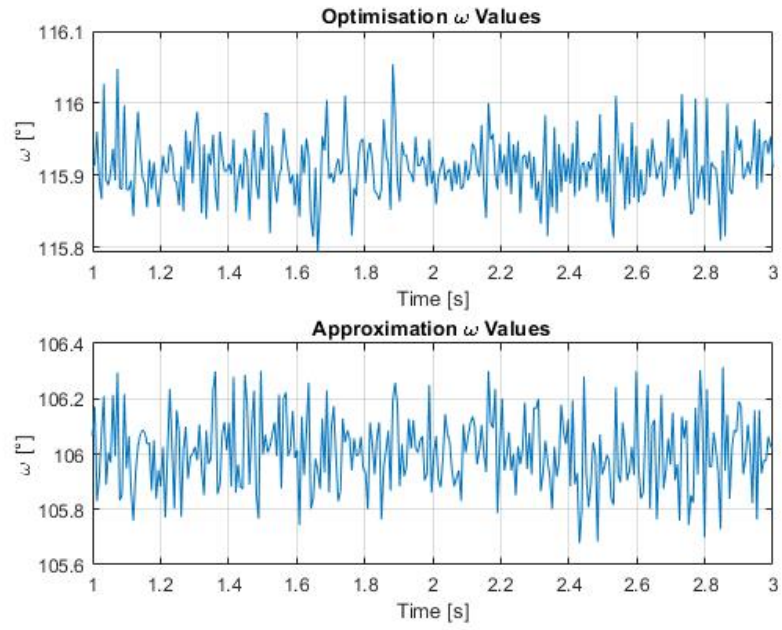
Figure 5.11: Graphs showing the values of ω calculated from the raw accelerometer readings for both the approximation and optimisation calculations
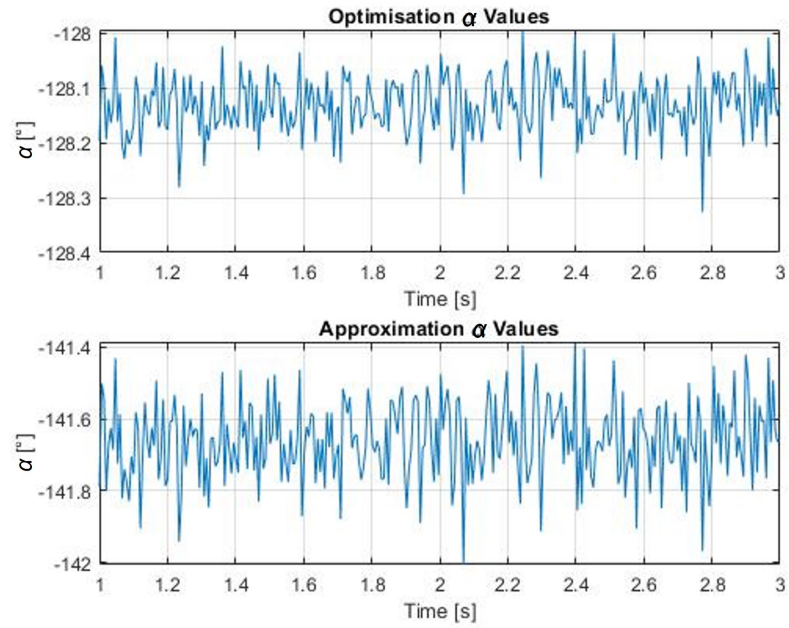
Figure 5.12: Graphs showing the values of α calculated from the raw accelerometer readings for both the approximation and optimisation calculations.

110

Table 5.3: Table showing the mean, range and variance of the α and ω angles calculated using accelerometer raw data taken for a single trial

	Approximation ω	Approximation α	Optimisation ω	Optimisation α
Mean	106.01	-141.66	115.91	-128.13
Range	0.6364	0.6147	0.2611	0.3301
Variance	0.00032	0.000208	0.000032	0.000049
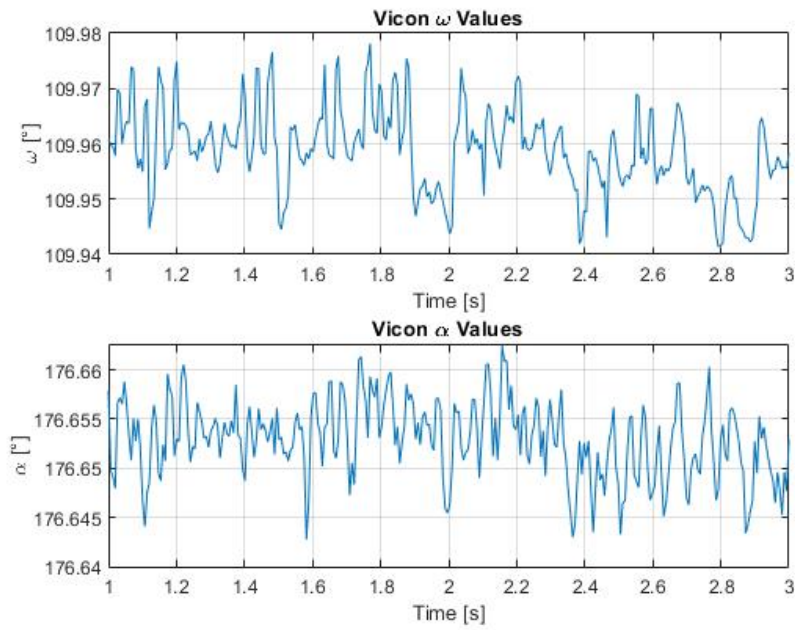
Figure 5.13: Graphs showing the values of α and ω angles calculated from the raw Vicon readings
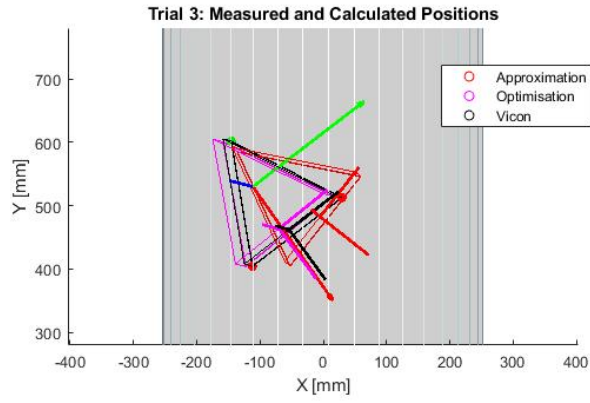
Figure 5.14: Image showing the position and orientation plotted from the averages values of the raw data for the Vicon (black), approximation (red) and optimisation (purple) for $b = 180$
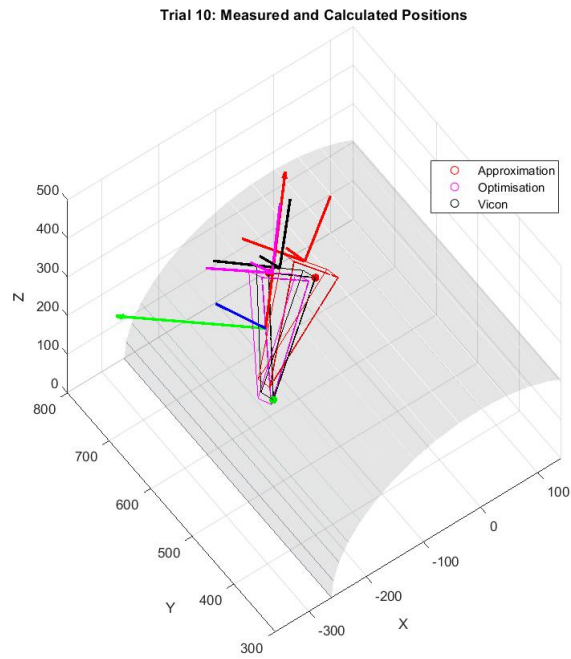
Figure 5.15: Image showing the position and orientation plotted from the averages values of the raw data for the Vicon (black), approximation (red) and optimisation (purple) for trial 10 for $b = 70mm$
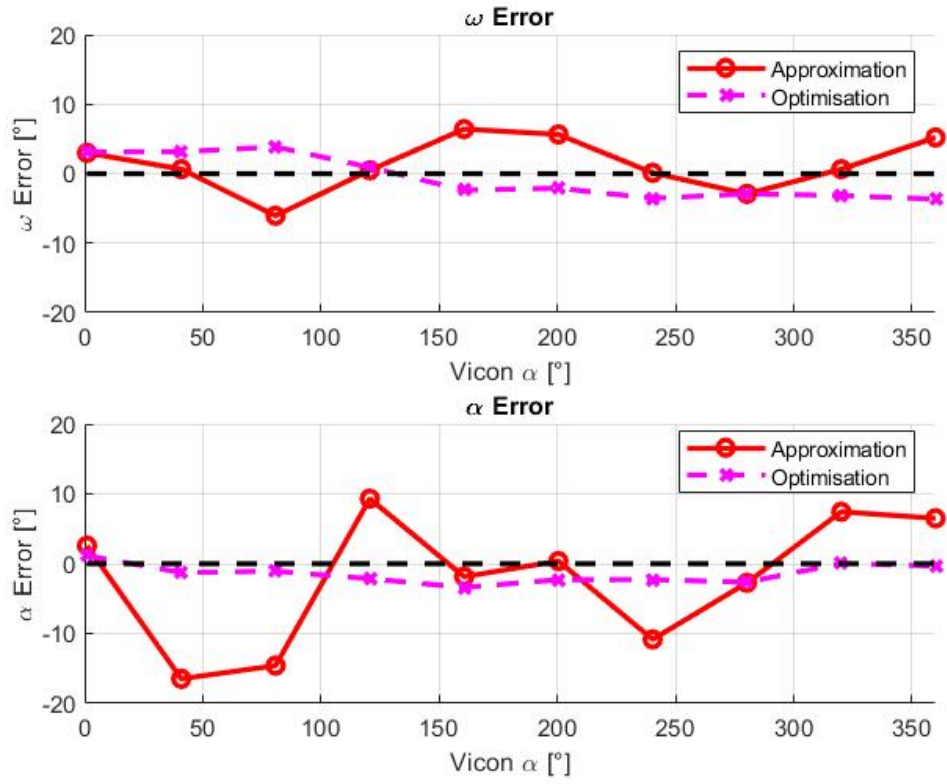
Figure 5.16: Comparison between the error between the angles calculated from the accelerometer and the measured Vicon angles for $b = 180mm$ $l = 180mm$ $R = 253.5mm$.
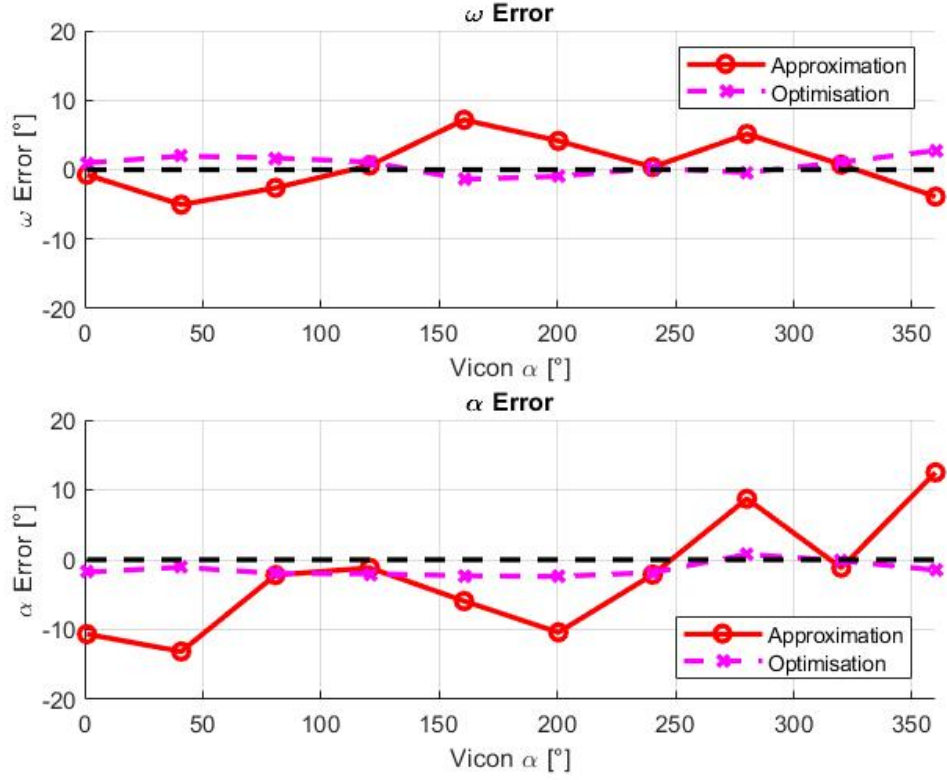
Figure 5.17: Comparison between the error between the angles calculated from the accelerometer and the measured Vicon angles for $b = 70mm$ $l = 180mm$ $R = 253.5mm$

Table 5.4: The standard deviations calculated for the graphs presented for the ω and α angles with and without the optimisation step.

Standard Dev.	Approximation	Optimisation
α: $b = 180mm$	$9.20°$	$1.40°$
ω: $b = 180mm$	$3.91°$	$3.08°$
α: $b = 70mm$	$8.23°$	$3.67°$
ω: $b = 70mm$	$3.95°$	$2.79°$

Table 5.5: Max and min errors in the calculated angles compared to the Vicon data for $b = 180mm$ and $l = 180mm$

	Max Approx	Min Approx	Max Para	Min Para	Max Opt	Min Opt
Alpha	16.47°	0.37°	16.47°	0.37°	3.40°	0.04°
Omega	6.42°	0.12°	5.28°	0.98°	4.17°	0.14°

Table 5.6: Max and min errors in the calculated angles compared to the Vicon data for $b = 70mm$ and $l = 180mm$

	Max Approx	Min Approx	Max Para	Min Para	Max Opt	Min Opt
Alpha	13.14°	1.16°	12.60°	0.70°	2.39°	0.15°
Omega	7.23°	0.45°	3.56°	15°	2.75°	0.16°

All these sources of error will accumulate, resulting in the disagreement between the calculated angles and the measured angles. One reason the angles calculated using the analytical approximation error is large compared to the Vicon measurements is because the approximation does not consider change in pitch of the test rig as it rotates. This explains why the algorithm error shows a peak error in the ω angle at approx. 45° 90° 270° and 315°. The results show that the optimisation step corrects these inaccuracies. There appears that there is a discrepancy between the 0° and 360° results in the α angle. This is present as the ω angle for both the trial were different, showing that the α angle calculation is dependant on the value of ω.

5.2.1 Error Analysis

There are two main sources of error which have been investigated in this work. These being the assumption that the pipe is perfectly horizontal and level with the flat ground, error in the accelerometer readings, and ovality of the pipe.

Figure 5.19 shows the error associated with the calculated angles as the pipe angle is increased from 0° to 5° with the rig rotating 360° in α, while assuming the pipe is

horizontal. This pipe angle is shown in Figure 5.18. The error between the simulated and optimised α and ω angles is then calculated. This shows that the elevation angle of the pipe is an important factor to consider, as a small pipe angle of $5°$ can have as much as a $10°$ error in the calculated orientation of the rig. Pipe angle appears to have a less significant effect on the ω angle as there is a maximum discrepancy of $2°$ for a $5°$ error in pipe angle. The alpha error appears to correspond to the pipe angle error.
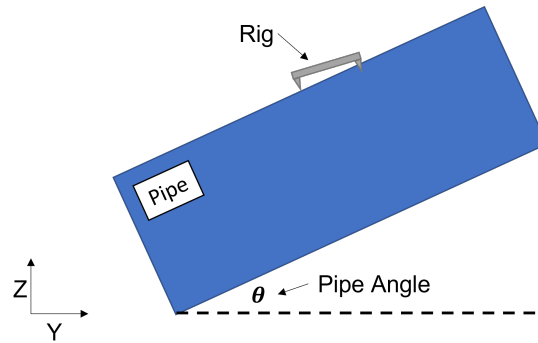
Figure 5.18: Schematic showing the angle of the pipe being varied
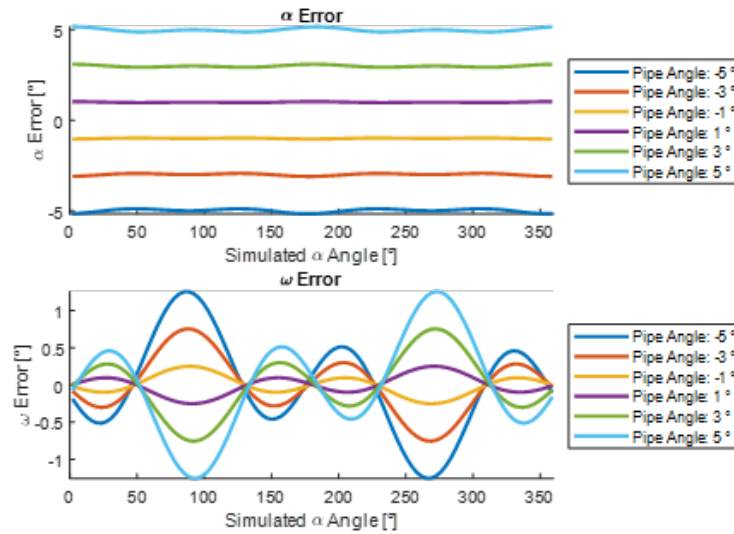
Figure 5.19: Error in calculated angles with changing pipe angle

Simulations were conducted to investigate the effect of incorrect accelerometer readings in the X, Y and Z directions. This error can be present in real environments in the form

116

of random error from sources such as outside vibrations from the pipe, or systematic errors in the calibration of the accelerometer. Error in terms of a percentage error in gravity was added to each of the X, Y, Z accelerometer readings. These are shown in figure Figure 5.20 and shows that as angle increases, the error increases. Error in the Xacc and Yacc affect the α and ω similarly, while error in the Z_{acc} mainly affects the ω angle, with minimal effect on the calculated α angle.,
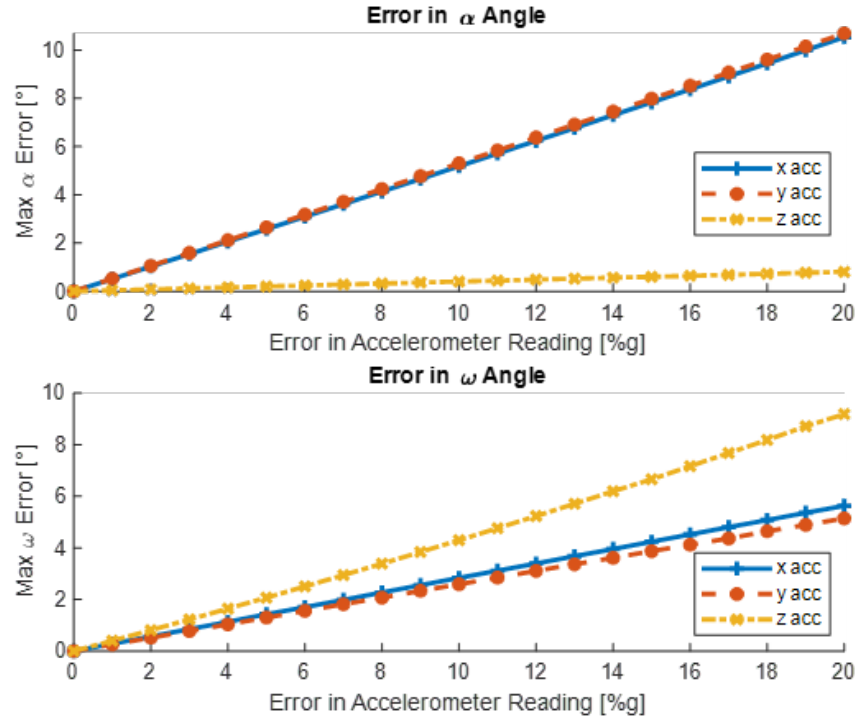
Figure 5.20: Error in calculated angles as error is added to the X, Y, Z acceleration readings

Another error which may be present when working with non-ideal pipes is that the pipe may not be perfectly cylindrical in shape. The error associated with increasing ovality was solved numerically and is shown in Figure 5.19. ASME (The American Society of Mechanical Engineers) guidelines state a tolerance of $< 8\%$ for ovality and many pipe manufactures consistently claim an ovality tolerance of 2% or less. These represent a $2°$ and $0.5°$ error in α respectively. A 0.7% ovality of the test sample corresponds to a $0.2°$ error in ω.
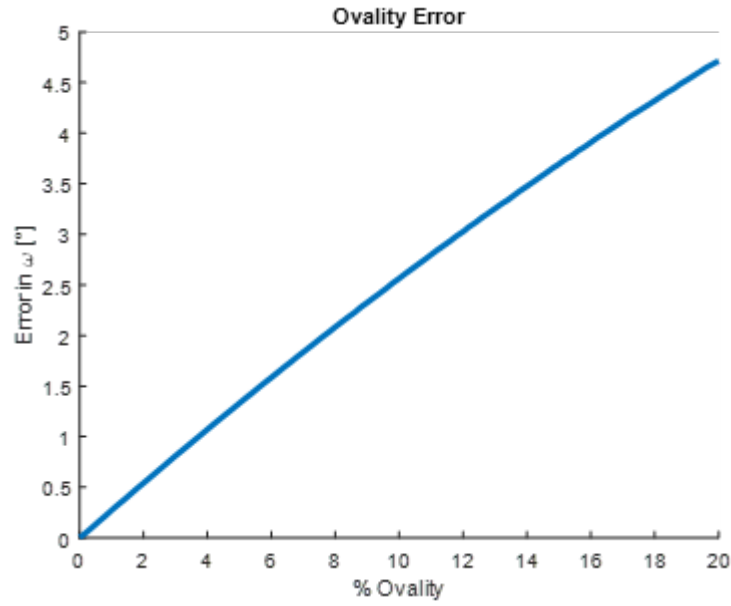
Figure 5.21: Error in ω angle calculation with respect to increasing ovality of the pipe

5.2.2 Error Risk Mitigation

There are several factors which can have an affect on the accelerometer readings which may affect the results. This section explores the possible effects of these sources and how they were mitigated in these experiments. These include:

- Pipe not level: The mathematical models used assume that the pipe used is perfectly horizontal and any deviation from this will result in a discrepancy. The level of the pipe varied by 3mm over the total length (1.53m) of the pipe which represents a 1.18% error in radius. This variation occurred at the joining of the two cylinders. The experiments were carried out away from this location so that this variation did not have an effect on the results. The floor was found to vary by <1mm over 1.5m distance, and a a spirit level was used to measure the flatness.

- Test rig not flat: The flatness of the test rig was tested using a circular spirit level and manually adjusted. Human error is present and therefore this may cause an

error in the calculated angles.

- Ovality: Ovality of the pipe was measured using the 3Leica laser tracker AT901 system to determine the cylindricality of the test pipe which showed a maximum variation in the pipe outer diameter of 1.09mm which represents a 0.36% ovality. This is in line with the American Petroleum Institutes API 5L manufacturing standard [113], which states that ovality should not exceed 1%.

- Error in Vicon measurements: The Vicon was taken to be ground truth as has been done in many studies [33], [97], [99], however [98] showed that the error associated between the measured position and the real position was an average of 1.48mm using the active calibration method employed in this work. This is in the same region of values of the 1.8mm circumferential error recorded in the results and represents an ω angle error of less than $0.1°$ in this setup.

5.2.3 Discussion

Considering the sources of error, this work shows a novel method of calculating the circumferential and orientation angles of a 3-point-of-contact rig from accelerometer sensor readings. The algorithm plots in Figure 5.16 and Figure 5.17 appear to follow the patterns shown in the Figure 3.4. There was a maximum error in the optimisation solution observed of $\Delta\alpha = 3.40°$ and $\Delta\omega = 4.17°$. These values are within a $5°$ error which is deemed acceptable by the Eddyfi Technologies. However, as mentioned previously, there are possible sources of error which will also be present in a real-world industrial environment which may have accumulated to realise the error shown. Table 5.5 and Table 5.6 compare the Inverse model, parametric method and optimisation solutions. The results show that there is an increase in accuracy in the ω angle when comparing the parametric and optimisation methods. It should be noted that where the α angle was not corrected in the parametric method for the reasons outlined in the previous section. This work presents a novel method of using accelerometer measurements to obtain absolute position and orientation measurements from an internal sensor for positioning on a pipe surface. The calculated angles rely on gravity as

a constant reference, therefore the output of this will not have integral error which accumulates with time. This absolute measurement type is vital for hand held probe positioning and robotic applications which need to be tracked over a long period of time. This will be a necessary requirement for fully autonomous pipe inspection. The experiments show that the algorithm developed calculates the positional angle (ω) and the orientation (α) on a horizontal pipe using only the knowledge of the device and pipe geometry, and the output of a 3-axis accelerometer to within the specified $< 5°$ accuracy. This positioning method can be improved by fusing other sensor information, such as a wheel encoder, gyroscope or magnetometer readings for real time positioning considering historical positioning data. Kalman filters are a form of Bayesian filtering that is commonly used for random noise reduction and sensor fusion for robot positioning [114]. A Kalman filter can be used to correct wheel encoder position measurements and prevent them from drifting over time, providing that there is an absolute measurement used for the correction step. This concept is explored in the subsequent chapter.

Chapter 6

Kalman Filter

Positioning sensors have inherent errors associated with them due to the physical mechanisms used. This limitation means that every sensor will have different errors and uncertainties associated with them [11]. As positional measurements will all have different uncertainty, probabilistic approaches to sensor fusion have been explored in the field of robotics [11]. The use of probabilistic approaches for the positioning problem is seen as one method of reducing the uncertainty in the positioning error and is commonly seen as a prerequisite for fully autonomous systems [49]. This chapter investigates the use of Bayesian filtering methods, specifically the Extended Kalman Filter, in order to reduce the error by fusing measurement information from multiple sources.

6.1   Bayes Law and Conditional Probability

The Bayesian Filter is a recursive algorithm and is the most fundamental probabilistic algorithm for calculating beliefs. The main concept of the Bayesian Filter is that new information obtained about the system can be used to update the estimate of the state of the system and its probability distribution [115]. This is sometimes referred to as a "belief" as the state of the system can not be measured directly, and therefore needs to be inferred, or calculated, from sensor data [11].

The general Bayesian filter [23] is described below:

Prediction Step:

$$bel(x_t) = \int p(x_t \mid u_t, x_{t-1})bel(x_{t-1})dx_{x-1} \qquad (6.1)$$

Measurment Update Step:

$$bel(x_t) = \eta p(z_t \mid x_t)bel(x_t) \qquad (6.2)$$

Where:

- $bel(x_t)$ is the belief of the state being estimated at time t

- u_t is the control input to the system

- $bel(x_{t-1})$ is the belief of the state at the previous time step

- z_t is the observed measurement at time t

- η is the normalisation constant

$p(x_t \mid u_t, x_{t-1})$ is the probability of x_t given the control input u_t and the previous state x_t. $bel(x_{t-1})$ which is the belief of the state values at the previous time step. Therefore, this shows that the first step of the Bayes Filter propagates the previous belief forward one time step based on the control input. This is known as the Prediction Step. The second step in the Bayes Filter is known as the Measurement Update Step, where the previous belief is multiplied by the probability that the observation (z_t) occurred, given x_t. Both of these multiplied together do not output a probability and may not integrate to 1. Therefore the result is normalised using the normalisation constant η.

The Bayes Filter assumes that the Markov assumption holds true. The Markov assumptions

postulates that all observations are conditionally independent, or that are not dependant on their non-descendants. This may not be the case as there can be unmodelled dynamics in the environment which are not taken into account in x_t and there can be inaccuracies in the probabilistic models [11].

6.2   Kalman Filter Theory

The Kalman filter is a form of Bayesian filtering and is an optimal estimation algorithm based on a dynamic model of the system and a measured parameter [23]. It is used in control systems and can be utilised in robot positioning when there is error associated with the measurements. This is done by using a weighted average based on the uncertainty of the system model and the uncertainty in the measurement. Some of the strong points are that it allows for the estimation of past, present and future states, and it is an optimal estimator for when uncertainties can be modelled as Gaussian distributions [116].

In addition to the Markov assumptions the following assumptions are also made:

- The system dynamics (control input and state update equations) are assumed to be linear with random Gaussian noise due to the inherent uncertainty in sensors.

- The measurement model is linear with random Gaussian noise, again due to the inherent uncertainty present in sensors.

- The initial belief (x_0) is normally distributed

The Kalman Filter algorithm is given below and the derivation can be found in [11]. For a one dimensional case:

Preditcion Step:

$$\hat{x}_t = x_{t-1} + u_t \tag{6.3}$$

$$K = \frac{\sigma_{est}^2}{\sigma_{est}^2 + \sigma_{meas}^2} \tag{6.4}$$

Measurment Update Step:

$$x_t = \hat{x}_t + K(z_t - \hat{x}_t) \tag{6.5}$$

$$\sigma_t^2 = (1 - K)\sigma_{est}^2 \tag{6.6}$$

- $\hat{x}_t$ is a single state variable

- u_t is a control input

- K is the Kalman Gain, weighting the filter between the expected value from the control input and the measured observation.

- σ_{est}^2 is the variance of the estimate

- σ_{meas}^2 is the variance of the measurement

- x_t is the corrected value of the state variable

- z_t is observed measurement

- σ_t^2 is the variance of the corrected value x_t

This is the general Kalman filter for a single state variable, single input and single measurement.

Figure 6.1 shows a step by step one-dimensional example of how the the probability distributions are combined in order to reduce uncertainty in the Kalman Filter. (a) shows the initial estimate of the position $bel(x_t)$, where x_t is the initial estimate and the

curve is the uncertainty distribution. (a) shows the initial estimate with an observation (z_t), such as a measurement of the physical position of the system. (c) shows the filter updating the belief based on the 2 previous distributions mean and variance, weighting the estimate and observation based on the Kalman gain and reducing the uncertainty. (d) shows the input result of the state update equations propagating to the next time step as a result of the control input to the system using the weighted average found in (c). (e) shows the new available observed measurement. (f) shows the filter updating the estimate using the 2 previous distributions.
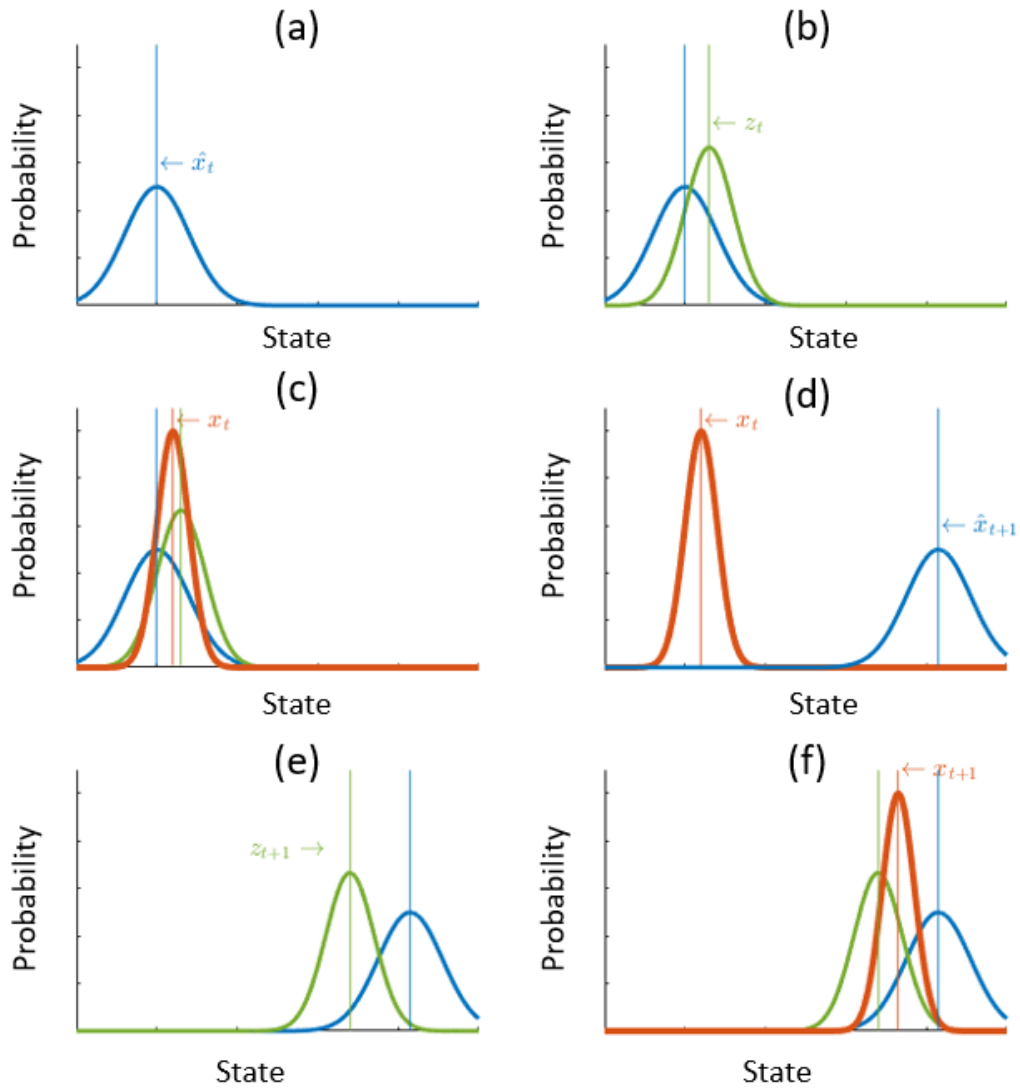
Figure 6.1: Graphs explaining the different steps of the Kalman filter algorithm

There are many different extensions to the standard Kalman filter which aim to address the non-linear nature of the state estimate equations. The two most common implementations are the Extended Kalman Filter and the Unscented Kalman Filter (UKF). The UKF takes several samples around the current state estimate and passes these through a non-linear transform and then builds a Gaussian probability density function from these points. The EKF linearises the state equations at the current step. The UKF is computationally more intensive, as the prediction step is computed multiple times per iteration, with studies and literature expressing that the performance difference between these two options is often negligible [11] [112]. For this reason, the EKF is used for the sensor fusion applications of this work.

6.3   Extended Kalman Filter Theory

If the state equations are non-linear, which is the case with many real world systems, the Gaussian assumption is no longer valid and the estimate will diverge. This linearisation is done using the first order Taylor Series Expansion in the Jacobian Matrices.

The assumptions that observations are linear are essential for the Kalman Filter to work. This is because any linear transformation of a Gaussian random variable results in another Gaussian random variable. The EKF considers processes which are non linear for both the state equations and measurement models as given below:

State Equation:

$$x_t = f(x_{t-1}, u_{t-1}, w_{t-1}) \tag{6.7}$$

Measurement Equation:

$$z_t = h(x_t, v_t) \tag{6.8}$$

Where x_t is the next state, u_{t-1} is the control input, w_{t-1} is process noise and v_t is the

noise in the measurement value.

Prediction Step:

$$\hat{x}_t = f(x_{t-1}, u_t, w_t) \tag{6.9}$$

$$\hat{P}_t = A_t P_{t-1} A_t^T + W_t Q_t W_t^T \tag{6.10}$$

Measurment Update Step:

$$K_t = \hat{P}_t H_t^T (H_t \hat{P}_t H_t^T + V_t R_t V_t^T)^{-1} \tag{6.11}$$

$$x_t = \hat{x}_t + K_t(z_t - H_t \hat{x}_t) \tag{6.12}$$

$$P_t = (I - K_t H_t)\hat{P}_t \tag{6.13}$$

Where:

- $\hat{x}_t$ is now a one dimensional vector of state variables, for example [position, velocity].

- A_t is an $n \times n$ Process Jacobian matrix, where n is the number of state variables. This linearises the state equations around the current operating point t. Described as $\frac{\partial f}{\partial x}$

- W_t is an $n \times m$ Process Control Jacobian matrix, where m is the number of control inputs. This linearises the control inputs at the current operating point t. Given by $\frac{\partial f}{\partial u}$

- u_t is the vector of the control inputs which are the the individual wheel speeds

- $\hat{P}_t$ is the covariance matrix of $\hat{x}_t$

- Q_t is the control input noise covariance matrix

- R_t is the measurement noise covariance matrix

- H_t is the measurement Jacobian relating the state variables to the measurements given by $\frac{\partial h}{\partial x}$.

- V_t is the measurement Jacobian given by $\frac{\partial h}{\partial v}$

- K_t is the Kalman Gain matrix

- z_t is the vector of observed measurement

- I is the identity matrix

6.4   EKF Simulations

Mathematical models describing the different states of the robot for tank floor and pipe scanning applications are presented below. This work was carried out for Eddyfi Technologies to demonstrate the feasibility of using multiple measurement sources for positioning their products in hazardous environments as proof of concept before implementing EKFs for pipe surfaces.

6.4.1   Differential Drive Wheel Kinematics for Dead Reckoning

A differential drive robot is one where the wheels are driven independently of each other. Steering is achieved by driving the wheels at different speeds allowing the robot to turn, eliminating the need for steerable wheels. A differential drive wheel setup was used in the subsequent simulations and filter designs to match the setup of Eddyfi products. Figure 6.2 shows a simple schematic of a differential drive robot and its relation to the global positioning system and the local robot coordinate system.
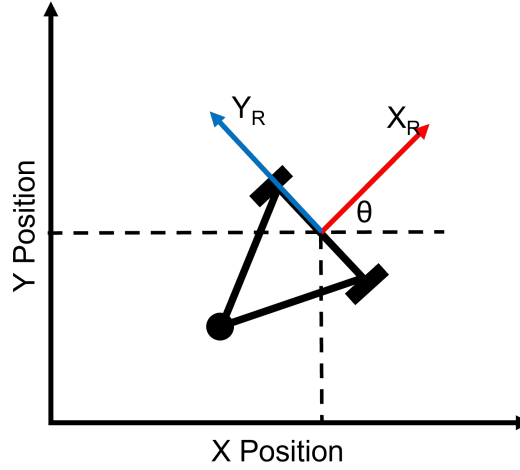
Figure 6.2: Differential Drive Robot Schematic where ϕ is the orientation of the robot and X_r and Y_r are the relative reference frame of the robot. X and Y position are the coordinates of the robot in a global reference frame.

The change in the pose of a robot, defined by an X, Y position and an angle ϕ can be defined as in Equation (6.14), Equation (6.15) and Equation (6.16). These are written in terms of the left and right wheel velocities [11].

$$\dot{x} = \frac{1}{2}(v_r + v_l)\cos\theta \tag{6.14}$$

$$\dot{y} = \frac{1}{2}(v_r + v_l)\sin\theta \tag{6.15}$$

$$\dot{\theta} = \frac{1}{b}(v_r - v_l) \tag{6.16}$$

Where; $\dot{x}$ is the change in the X dimension, $\dot{y}$ is the change in the Y dimension, $\dot{\theta}$ is the change in the orientation, $v_{r/l}$ are the speeds of the right and left wheel, and b is the wheelbase of the robot.

Using the kinematic equations, a mathematical model to describe the pose of the robot at each time-step can be deduced. This system of equations is used to predict the location of the robot based on the input wheel speeds and can be used to map the expected trajectory. Equation (6.17), Equation (6.18) and Equation (6.19) are used to predict the position and orientation [11].

$$x_t = x_{t-1} + \frac{1}{2}(v_r + v_l)\cos\phi \qquad (6.17)$$

$$y_t = y_{t-1} + \frac{1}{2}(v_r + v_l)\sin\phi \qquad (6.18)$$

$$\phi_t = \phi_{t-1} + \frac{1}{b}(v_r - v_l) \qquad (6.19)$$

6.4.2 Tank Floor Scanning Simulation

As part of the feasibility study into using the EKF for NDE positioning applications, simulations were designed and conducted for a EKF implementation for tank floor raster scanning, line by line, for the Eddyfi Floormap system.

Extended Kalman Filter Design

Simulations of an implementation of the EKF for a differential drive robot, using encoder values as the control input, and a GPS system measuring the x, y and z coordinates of the robot, with random error v associated with the measurement. This has been included here to further understand how the EKF can be implemented for mobile robotic problems and illustrate the EKF working.

The position and orientation of the robot were calculated using robot kinematic equations detailed in previously and have been rewritten here in matrix form for convenience.

State Equations:

$$\hat{x}_t = f(x_{t-1}, u_t, w_t) = \begin{bmatrix} x_t \\ y_t \\ z_t \\ \theta_t \end{bmatrix} = \begin{bmatrix} x_{t-1} + \frac{1}{2}(v_r + v_l)\cos(\theta_{t-1}) \\ y_{t-1} + \frac{1}{2}(v_r + v_l)\sin(\theta_{t-1}) \\ 0 \\ \theta_{t-1} + \frac{1}{b}(v_r + v_l) \end{bmatrix} \qquad (6.20)$$

130

Where x_t, y_t and z_t are the coordinates of the robot, θ_t is the orientation and b is the wheelbase of the robot. z_t is taken to be a constant 0 as this can be considered a 2D environment in terms of the positioning. The Jacobians and matricies used in the EKF algorithm are given below:

Process Jacobians:

$$\boldsymbol{A_t} = \frac{\partial f}{\partial x} = \begin{bmatrix} 1 & 0 & 0 & -\frac{1}{2}(v_r + v_l)\sin(\theta_{t-1}) \\ 0 & 1 & 0 & \frac{1}{2}(v_r + v_l)\cos(\theta_{t-1}) \\ 0 & 0 & 1 & 0 \\ 0 & 0 & 0 & 1 \end{bmatrix} \tag{6.21}$$

$$\boldsymbol{W_t} = \frac{\partial f}{\partial w} = \begin{bmatrix} \frac{1}{2}\cos(\theta) & \frac{1}{2}\cos(\theta) \\ \frac{1}{2}\sin(\theta) & \frac{1}{2}\sin(\theta) \\ 0 & 0 \\ \frac{1}{b} & \frac{1}{b} \end{bmatrix} \tag{6.22}$$

Process Noise Covariance Matrix:

$$\boldsymbol{Q_t} = \begin{bmatrix} \sigma_{rw}^2 & 0 \\ 0 & \sigma_{lw}^2 \end{bmatrix} \tag{6.23}$$

Measurement Model:

$$\bar{z}_t = h(x_t, v_t) = \begin{bmatrix} x_t + v_1 \\ y_t + v_2 \\ z_t + v_3 \end{bmatrix} \tag{6.24}$$

Measurement Jacobians:

$$\boldsymbol{H}_t = \frac{\partial h}{\partial x} = \begin{bmatrix} 1 & 0 & 0 & 0 \\ 0 & 1 & 0 & 0 \\ 0 & 0 & 1 & 0 \end{bmatrix} \qquad (6.25)$$

$$\boldsymbol{V}_t = \frac{\partial h}{\partial v} = \begin{bmatrix} 1 & 0 & 0 \\ 0 & 1 & 0 \\ 0 & 0 & 1 \end{bmatrix} \qquad (6.26)$$

Measurement Noise Covariance Matrix:

$$\boldsymbol{R} = \begin{bmatrix} \sigma_x^2 & 0 & 0 \\ 0 & \sigma_y^2 & 0 \\ 0 & 0 & \sigma_x^2 \end{bmatrix} \qquad (6.27)$$

It should be noted that the measurement model equation has been renamed as $\bar{z}_t$ to avoid confusion with z_t, which is the position in the z coordinate. Matrices and Equations (6.20) to (6.27) are used in the EKF algorithm described in Equations (6.9) to (6.13). It should be noted that in this case, the H Jacobian simplified quite nicely as the measurements observed are in the same units as the state variables, however this is not always the case and depends what is being measured and what the state variables are. In these simulations, it was assumed that $\sigma_{x,y,z} = 20mm$ and $\sigma_{rw,lw} = 2mms^{-1}$.

132

(a) GPS Measurement Comparison

(b) Odometry Comparison
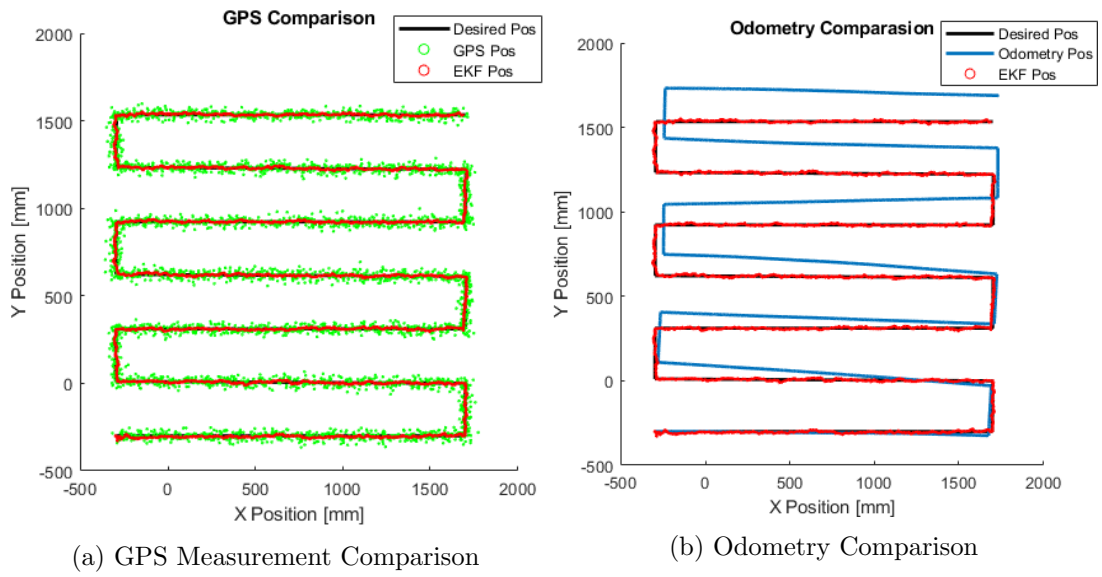
Figure 6.3: Comparison between EKF calculated estimates with the GPS measurement and Dead Reckoning
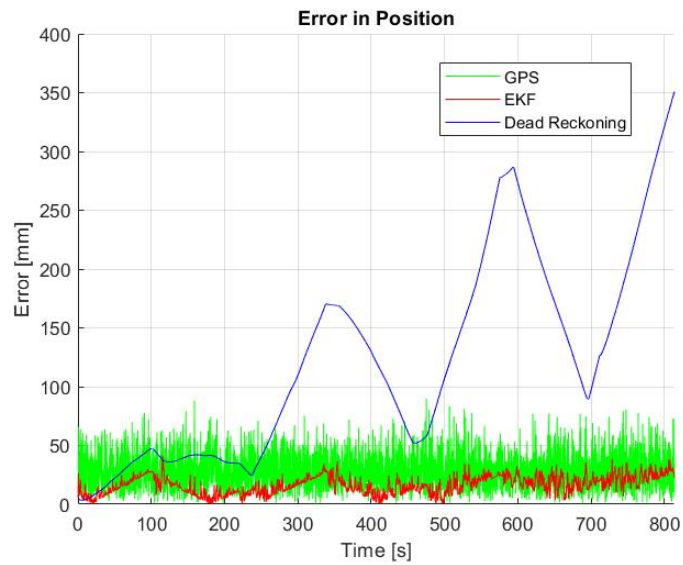
Figure 6.4: Graph showing the error in the position over time of the simulated raster scan comparing the Dead Reckoning (blue), GPS (green) and EKF (red)

Figure 6.3 shows the output of the dead reckoning (blue) and the estimated EKF position (red) compared to the desired position (black). The odometry position starts

133

out quite accurate, however due to the integral error, as the robot progresses though the raster scan, the inaccuracies grow larger. Fusing the odometry with the absolute GPS measurement prevents the positional error from becoming larger as a function of time. This is a key result of the EKF for sensor fusion over longer time periods.

Figure 6.4 shows that using the EKF (red) significantly reduces the overall error when compared to the raw GPS measurements (green) and the fusion of the GPS and dead reckoning removes the integral error and reduces overall error over time.

6.5   Pipe Scanning EKF Equations

The EKF for a differential drive robot presented previously is suitable for 2D applications and needs to be modified for 3D pipe surfaces. The state equations in Equation (6.28) show the modified kinematic equations for a differential drive robot bound to the surface of the pipe. In this case, the Z direction position can no longer be assumed as constant. The positions in the X and Z directions are based on the parametric equations of a circle and describe the component of the system movement in the X and Z directions. The Y position y_t is calculated by adding the component of the velocity in the y direction to the previous y value y_{t-1}. α, ω and $\dot{\omega}$ are also added to the state matrix, where $\dot{\omega}$ is calculated using the velocity component of the system which is tangential to the pipe clock-face surface. Equation (6.29) to Equation (6.39) show the developed EKF for a differential drive robot on a pipe surface with the modified kinematic equations.

State Equations:

$$\hat{x}_t = f(x_{t-1}, u_t, w_t) = \begin{bmatrix} x_t \\ y_t \\ z_t \\ \alpha_t \\ \omega_t \\ \dot{\omega}_t \end{bmatrix} = \begin{bmatrix} r_p \sin(\omega_{t-1} + \dot{\omega}_{t-1}) \\ y_{t-1} + (\frac{v_r + v_l}{2}) \cos(\alpha_{t-1}) dt \\ r_p \cos(\omega_{t-1} + \dot{\omega}_{t-1}) \\ \alpha_{t-1} + (v_r - v_l)\frac{dt}{b} \\ \omega_{t-1} + \dot{\omega}_{t-1} \\ \frac{v_r + v_l}{2} \sin(\alpha_{t-1})\frac{dt}{r_p} \end{bmatrix} \tag{6.28}$$

The equations for x_t and z_t are taken from the equations of a circle. The equation for y_t uses the previous position in the y direction and adds the change in the y direction calculated from the wheel velocities and the orientation of the robot. α_t is calculated from the wheel velocities and $\dot{\omega}$ is calculated taking the velocity tangential to the cylinder surface. dt is the time step between each calculation of the system which comes from the control input to the system (u_t), in this case dictated by the encoder refresh rate. The encoders are assumed to have random error denoted here by the covariance matrix w_t.

Process Jacobians:

$$A = \begin{bmatrix} 0 & 0 & 0 & 0 & \frac{\partial x}{\partial \omega} & \frac{\partial x}{\partial \dot{\omega}} \\ 0 & 1 & 0 & \frac{\partial y}{\partial \alpha} & 0 & 0 \\ 0 & 0 & 0 & 0 & \frac{\partial z}{\partial \omega} & \frac{\partial z}{\partial \dot{\omega}} \\ 0 & 0 & 0 & 1 & 0 & 0 \\ 0 & 0 & 0 & 0 & 1 & 1 \\ 0 & 0 & 0 & \frac{\partial \dot{\omega}}{\partial \alpha} & 0 & 0 \end{bmatrix} \tag{6.29}$$

Where:

$$\frac{\partial x}{\partial \omega} = \frac{\partial x}{\partial \dot{\omega}} = r_p \cos(\omega_{t-1}) \cos(\dot{\omega}_{t-1}) - r_p \sin(\omega_{t-1}) \sin(\dot{\omega}_{t-1}) \tag{6.30}$$

$$\frac{\partial z}{\partial \omega} = \frac{\partial z}{\partial \dot{\omega}} = -r_p \sin(\omega_{t-1}) \cos(\dot{\omega}_{t-1}) - r_p \cos(\omega_{t-1}) \sin(\dot{\omega}_{t-1}) \tag{6.31}$$

$$\frac{\partial y}{\partial \alpha} = -\frac{v_r + v_l}{2} \sin(\alpha_{t-1}) dt \tag{6.32}$$

$$\frac{\partial \dot{\omega}}{\partial \alpha} = \frac{v_r + v_l}{2 r_p} \cos(\alpha_{t-1}) dt \tag{6.33}$$

$$W = \begin{bmatrix} 0 & 0 \\ \frac{\cos(\alpha_{t-1}) dt}{2} & \frac{\cos(\alpha_{t-1}) dt}{2} \\ 0 & 0 \\ \frac{dt}{b} & -\frac{dt}{b} \\ 0 & 0 \\ \frac{\sin(\alpha_{t-1}) dt}{2 r_p} & \frac{\sin(\alpha_{t-1}) dt}{2 r_p} \end{bmatrix} \tag{6.34}$$

Process Covariance Matrix:

$$\boldsymbol{Q_t} = \begin{bmatrix} \sigma_{rw}^2 & 0 \\ 0 & \sigma_{lw}^2 \end{bmatrix} \tag{6.35}$$

Three different measurement models where compared to investigate the effects on the overall accuracy of including different combinations of positional output. The three measurments simulated were; wheel encoder values for dead reckoning, an iGPS setup, and the α and ω angles which can be calculated from accelerometer output as described in the previous chapters. The measurement model and Jacobians combining iGPS and angle readings are shown below.

iGPS and Accelerometer Measurement Model and Jacobians:

$$z = \begin{bmatrix} x \\ y \\ z \\ \alpha \\ \omega \end{bmatrix} \tag{6.36}$$

$$H = \begin{bmatrix} 1 & 0 & 0 & 0 & 0 & 0 \\ 0 & 1 & 0 & 0 & 0 & 0 \\ 0 & 0 & 1 & 0 & 0 & 0 \\ 0 & 0 & 0 & 1 & 0 & 0 \\ 0 & 0 & 0 & 0 & 1 & 0 \end{bmatrix} \tag{6.37}$$

$$V = \begin{bmatrix} 1 & 0 & 0 & 0 & 0 \\ 0 & 1 & 0 & 0 & 0 \\ 0 & 0 & 1 & 0 & 0 \\ 0 & 0 & 0 & 1 & 0 \\ 0 & 0 & 0 & 0 & 1 \end{bmatrix} \tag{6.38}$$

Measurement Covariance:

$$R = \begin{bmatrix} \sigma_x^2 & 0 & 0 & 0 & 0 \\ 0 & \sigma_y^2 & 0 & 0 & 0 \\ 0 & 0 & \sigma_z^2 & 0 & 0 \\ 0 & 0 & 0 & \sigma_\omega^2 & 0 \\ 0 & 0 & 0 & 0 & \sigma_{\dot{\omega}}^2 \end{bmatrix} \tag{6.39}$$

6.5.1   Pipe Scanning EKF Simulation

Simulations were run to compare the estimated positions from the filters presented to the ideal case of a robot going around the circumference of a horizontal pipe. The measurement simulated are wheel encoder values, indoor GPS (iGPS) and α and ω angles.

There are a number of assumptions made during this simulation. These being:

- Full Coverage iGPS setup: It is assumed that the iGPS measurements are available all around the pipe. In practice, this is difficult to achieve on the underside of the pipe as line of sight is usually required for optimal positioning. There are many factors which affect the positioning capabilities of iGPS systems, including temperature, point source angle and error in the placement of the beacons [24].

- Measurement Frequency Standardised: The simulation was set up so that the refresh rate of all the simulated measurements are available at every time step. A refresh rate of 10Hz was used.

- Variances: The variances used of the measurements are;

  - $\sigma_{enc} = 2mms^{-1}$, as used in previous research [24]

  - $\sigma_{iGPS} = 20mm$, as quoted from existing iGPS (Pozyx) systems [117]

  - $\sigma_{angle} = 3°$ taken from the work conducted in Chapter 5.

Figure 6.5 shows the Cartesian comparison between the different EKF filters for robot simulated going around the circumference of a pipe for a single revolution. Where the X, Y and Z axis' are the position in the X,Y and Z directions in mm respectively. Each of the EKFs presented use the simulated wheel encoder values which are corrected in the EKF. It is shown that the dead reckoning using wheel encoder measurements (blue) are the furthest from the ideal case (black). The EKF correcting the α and ω angles (pink) shows improvement in positional accuracy compared to the dead reckoning. However, a Kalman filter using an ideal iGPS case (green) is more accurate. Although obtaining a similar result using actual iGPS is unlikely due to the ideal characteristics mentioned previously, it can be useful to compare the accuracy and use the ideal iGPS case as an ideal scenario. A Kalman filter combining both angles and iGPS positions (red) is also presented which is the most accurate filter shown.

(a) XY view

(b) ZY view

(c) Orthographic view
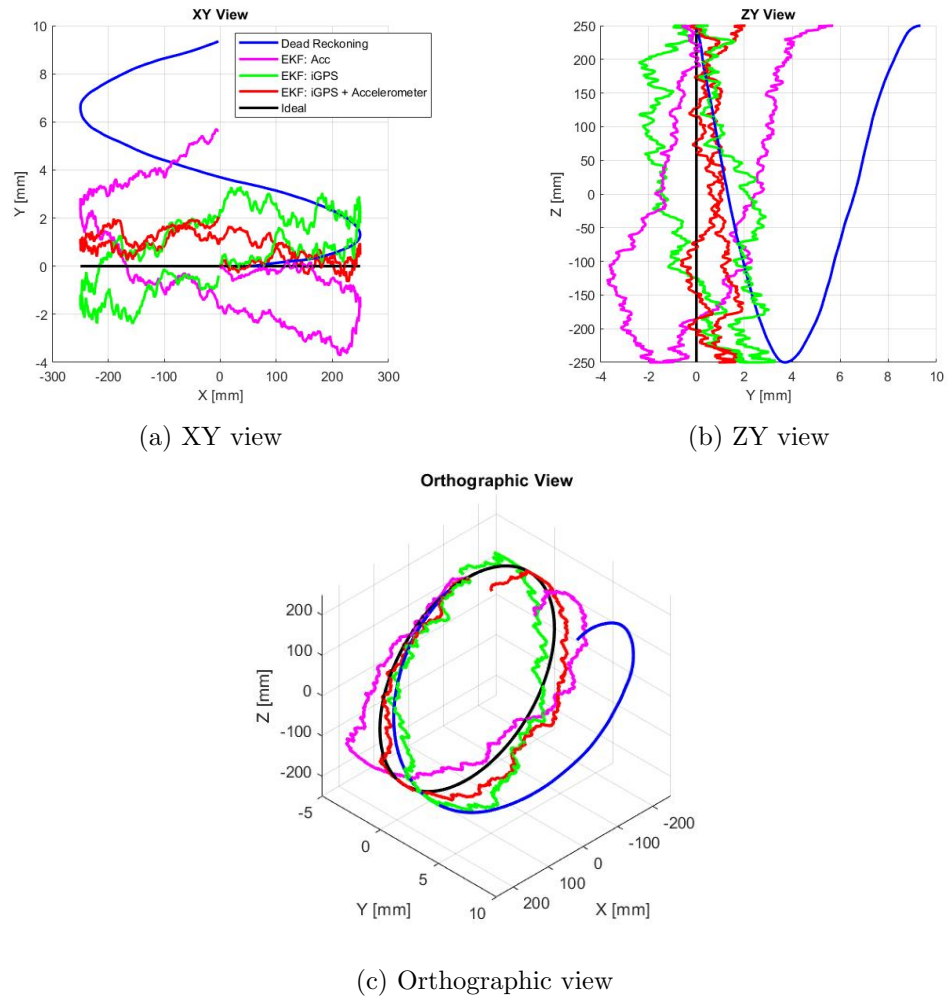
Figure 6.5: Dead Reckoning and EKF simulation results for a single trial for one revolution around the circumference of a pipe

(a) XY view

(b) ZY view

(c) Orthographic view
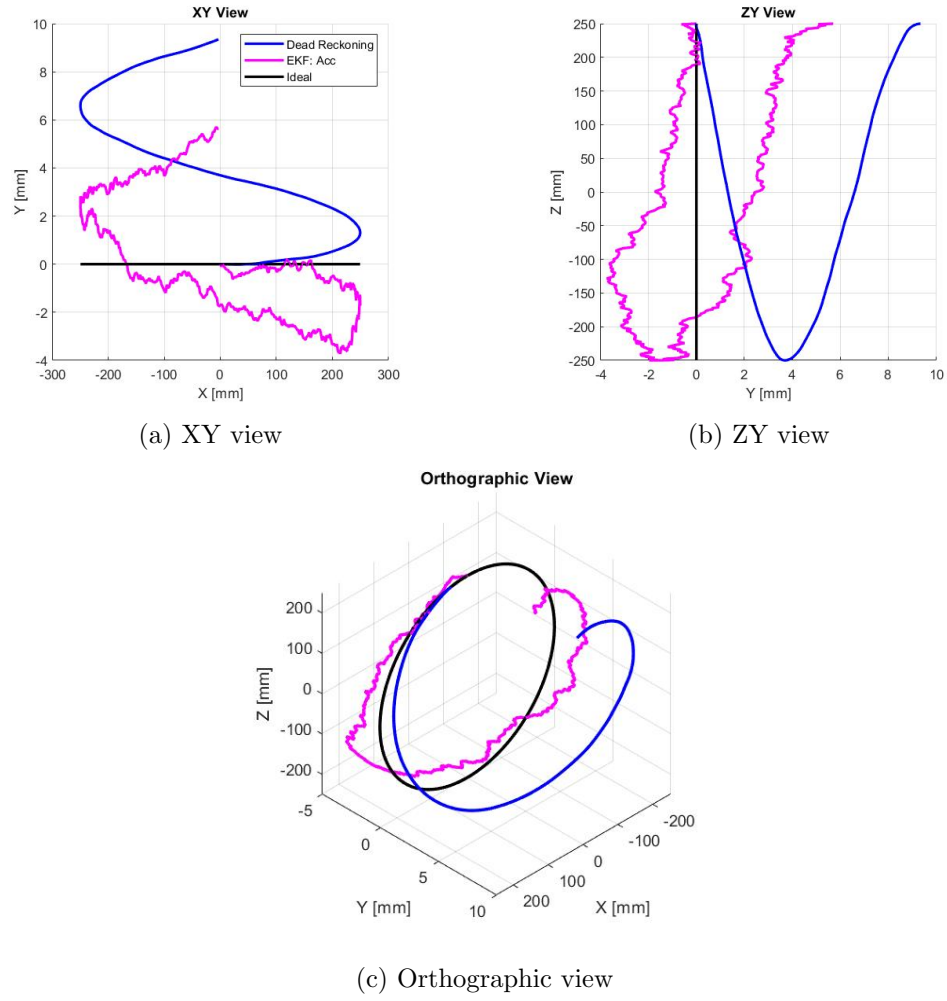
Figure 6.6: Dead Reckoning and accelerometer angle EKF simulation results for a single trial for one revolution around the circumference of a pipe

Figure 6.6 shows an example of the Cartesian comparison between the dead reckoning and the EKF using α and ω angle measurements in the correction step. It should be noted that over long periods of time the Y position calculated using the α angle will be subject to integral error. This is due to the orientation being corrected, rather than the Y position, although from the simulations conducted, this is still significantly more accurate compared to relying solely on wheel encoder readings with no correction.
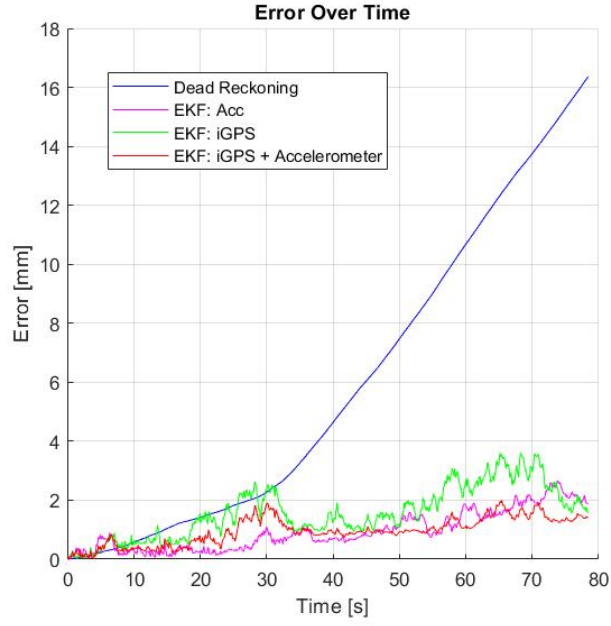
Figure 6.7: Graph showing the error along the surface of the pipe during one revolution for each of the EKFs and dead reckoning using wheel encoders

Figure 6.7 shows an example of the cumulative error along the circumference of the pipe surface for each time step, comparing the dead reckoning error with the EKF errors. It shows how even after one revolution the dead reckoning error is significantly higher than the errors of any of the EKFs due to the inherent nature of the integral error associated with wheel encoders.

The error is calculated as follows:

$$e = \sqrt{r_p^2 \Delta\omega^2 + \Delta Y^2} \tag{6.40}$$

Where; r_p is the pipe radius, $\Delta\omega$ is the difference in the circumferential angle between the ideal end point and the EKF end point and ΔY is the difference in the Y position along the pipe.
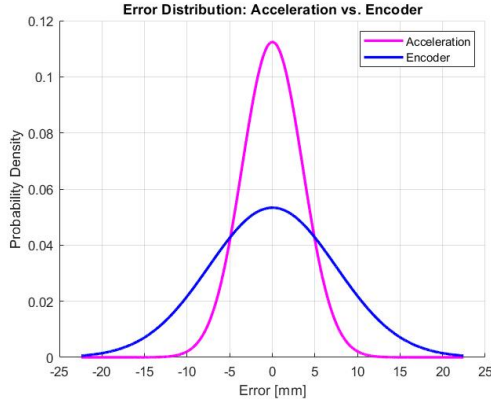
141

(a) Acceleration vs. Dead Reckoning
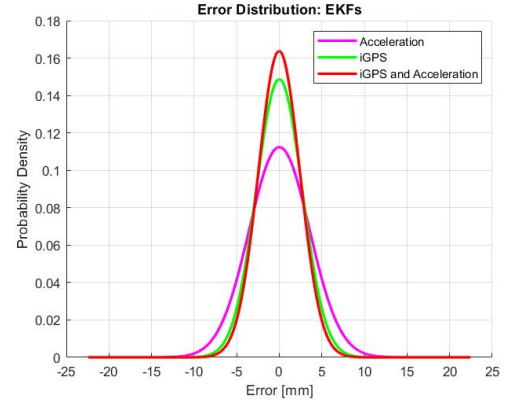
(b) Comparison of EKFs
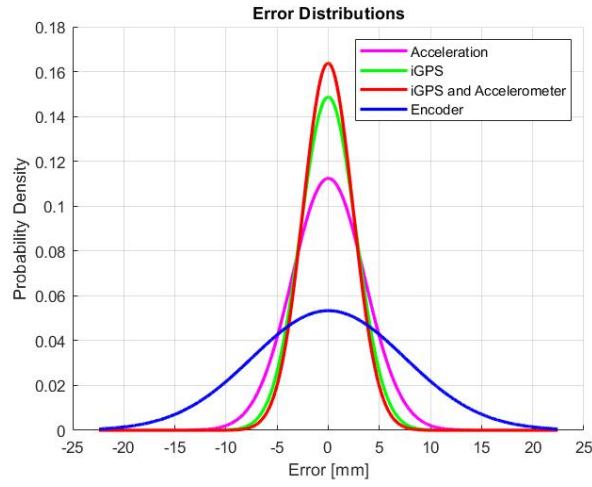
(c) Comparison of EKFs and Dead Reckoning

Figure 6.8: Comparison of distributions of error along the surface of the pipe between the end point of the measured positions and the ideal end point for 1 revolution

Figure 6.8a shows the distribution of the errors over 10,000 simulations between the end point of the ideal position and both the end position of the dead reckoning and EKF using the angle measurements. Figure 6.8b shows the comparison of the 3 EKFs tested; correction using angles (pink), iGPS (green) and both angles and iGPS (red). Figure 6.8c shows a comparison of the EKF errors with the dead reckoning error. Table 6.1 lists the standard deviations of these error distributions. The reduction in variance of the EKFs compared to the dead reckoning are as follows:

- Angles from Acceleration: 57.5%

- iGPS: 75.4%

- Angles and iGPS: 81.1%

Using an onboard accelerometer to determine the α and ω angles and fusing this with wheel encoder readings in the proposed EKF setup achieves an decrease in the variance of 57.5% for a single revolution simulation. This also represents 73% of the accuracy compared to the ideal iGPS case, without the impracticalities of setting up the system.

Table 6.1: Table showing the standard deviations of the error distributions for 1 revolution

Measurement	Standard Deviation [mm]
Dead Reckoning	7.08
Acceleration Angles	3.01
iGPS	1.74
iGPS and Angles	1.34

Further simulations are presented to showcase the usefulness of having an absolute measurement to correct the orientation and circumferential angle on a pipe over a longer period of time using the EKF. These simulations are extended for the case of 10 revolutions around the circumference of a pipe and presented below.

(a) XY view   (b) ZY view

(c) Orthographic view
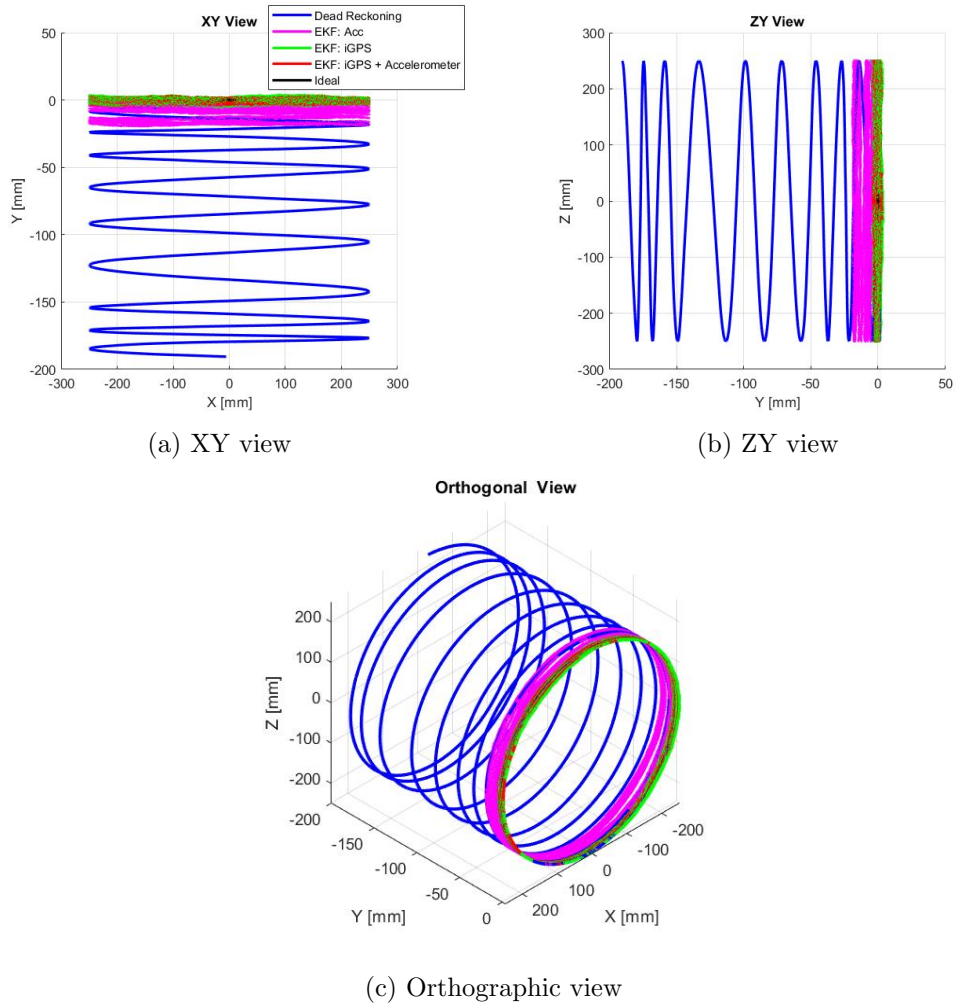
Figure 6.9: Dead Reckoning and EKF simulation results for a single trial for 10 revolutions around the circumference of a pipe

Figure 6.9 shows the Cartesian comparison between the dead reckoning and the EKFs. It can be seen that the wheel encoder measurements have significant drift compared to the EKFs. Figure 6.10 shows the comparison between the dead reckoning and the EKF using the angle measurements to correct the state estimates. This shows that there is a small amount of drift in the Y direction as expected and discussed previously, however it is significantly less compared to the dead reckoning. This shows that using sensor fusion of wheel encoder values and angles measurements presented previously, accuracy is significantly increased and this method may be feasible for autonomous or

144

semi-autonomous pipe inspection.

(a) XY view

(b) ZY view

(c) Orthographic view
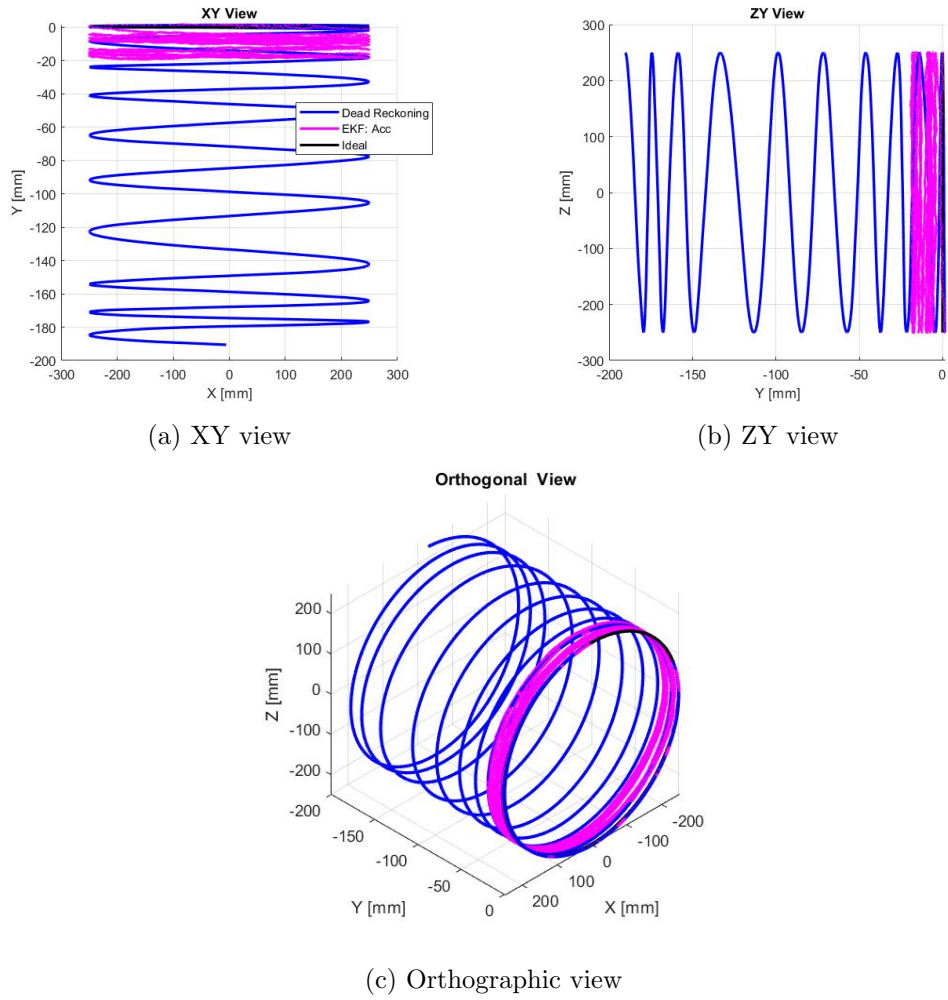
Figure 6.10: Dead Reckoning and accelerometer angle EKF simulation results for a single trial for 10 revolutions around the circumference of a pipe

145
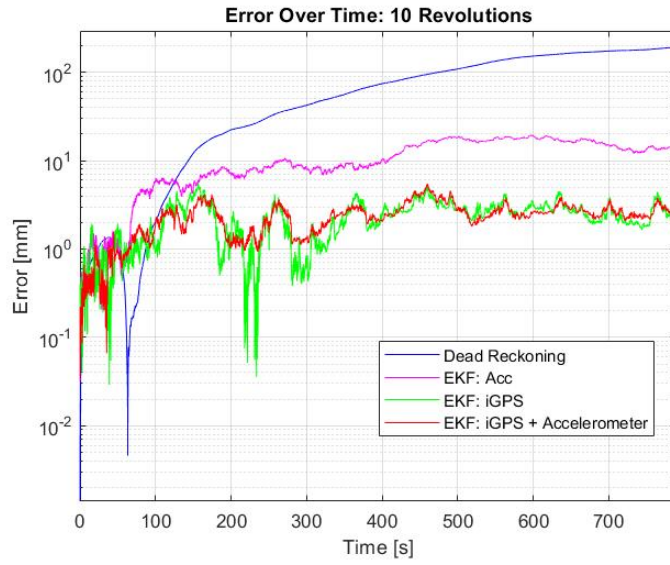
Figure 6.11: Graph showing the cumulative error along the surface of the pipe during 10 revolutions for each of the EKFs and dead reckoning using wheel encoders

Figure 6.11 shows an example of the cumulative error over 10 revolutions around the pipe on a log scale. This shows the slight drift compared in the *EKF: Acc*, which is expected as the orientation is corrected. Dead reckoning is an order of magnitude larger in this case when compared to the EKFs. as seen in the results shown in Table 6.2

(a) Acceleration vs. Dead Reckoning

(b) Comparison of EKFs

(c) Comparison of EKFs and Dead Reckoning
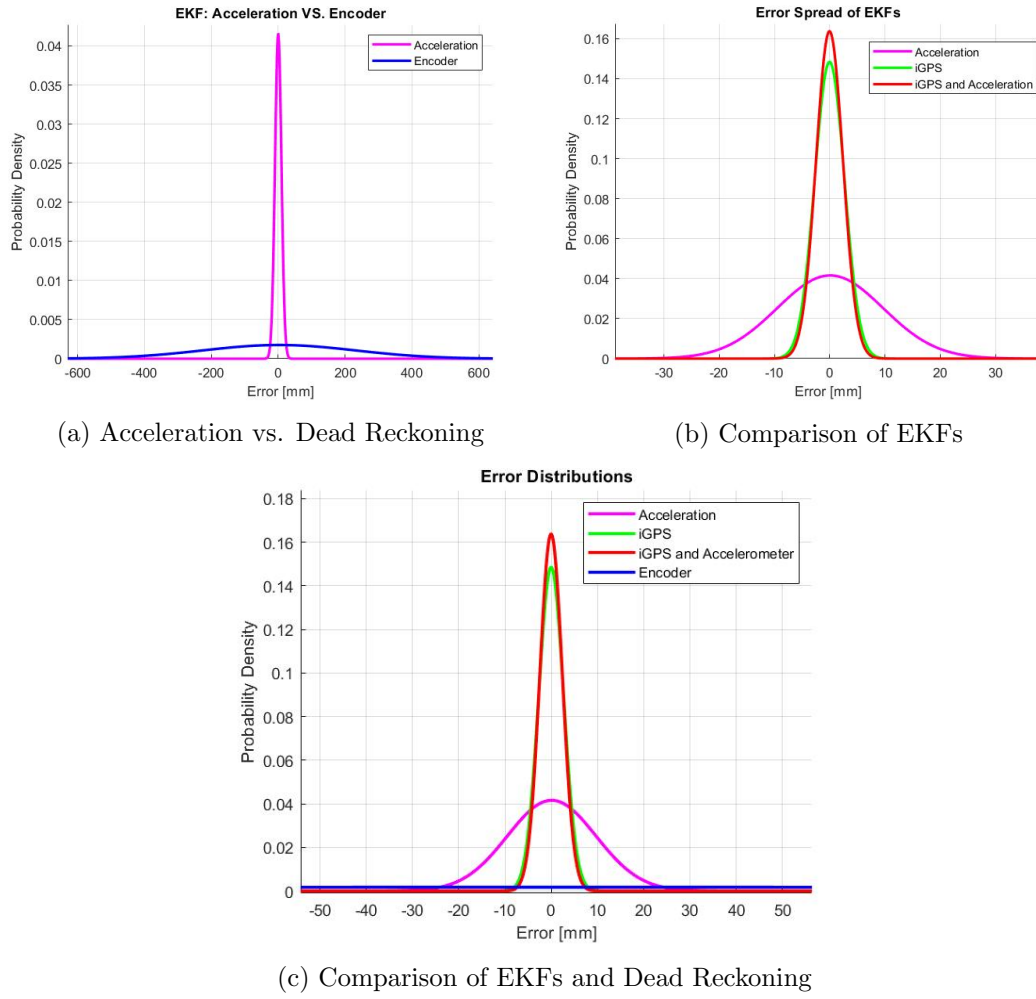
Figure 6.12: Comparison of distributions of error along the surface of the pipe between the end point of the measured positions and the ideal end point after 10 revolutions

Table 6.2: Table showing the standard deviations of the error distributions for 10 revolution

Measurement	Standard Deviation [mm]
Dead Reckoning	132.06
Acceleration Angles	10.11
iGPS	2.07
iGPS and Angles	2.01

Raster scan simulations are presented below to show how the designed EKF compares to dead reckoning when considering a traditional NDE scan path on a pipe surface. The raster scan covers $\frac{1}{4}$ of the circumference of the pipe, and each pass moves 50mm along the Y axis along the pipe. Figure 6.13 compares the ideal, dead reckoning and EKF using acceleration angles for a raster scan on a pipe surface. From this, the dead reckoning is shown to have an increasing error similar to that shown in the typical 2D raster scans in Figure 6.3b. Figure 6.14 once again shows that sensor fusion using and EKF decreases the error significantly compared to relying on wheel encoders.

(a) XY view

(b) ZY view

(c) Orthographic view
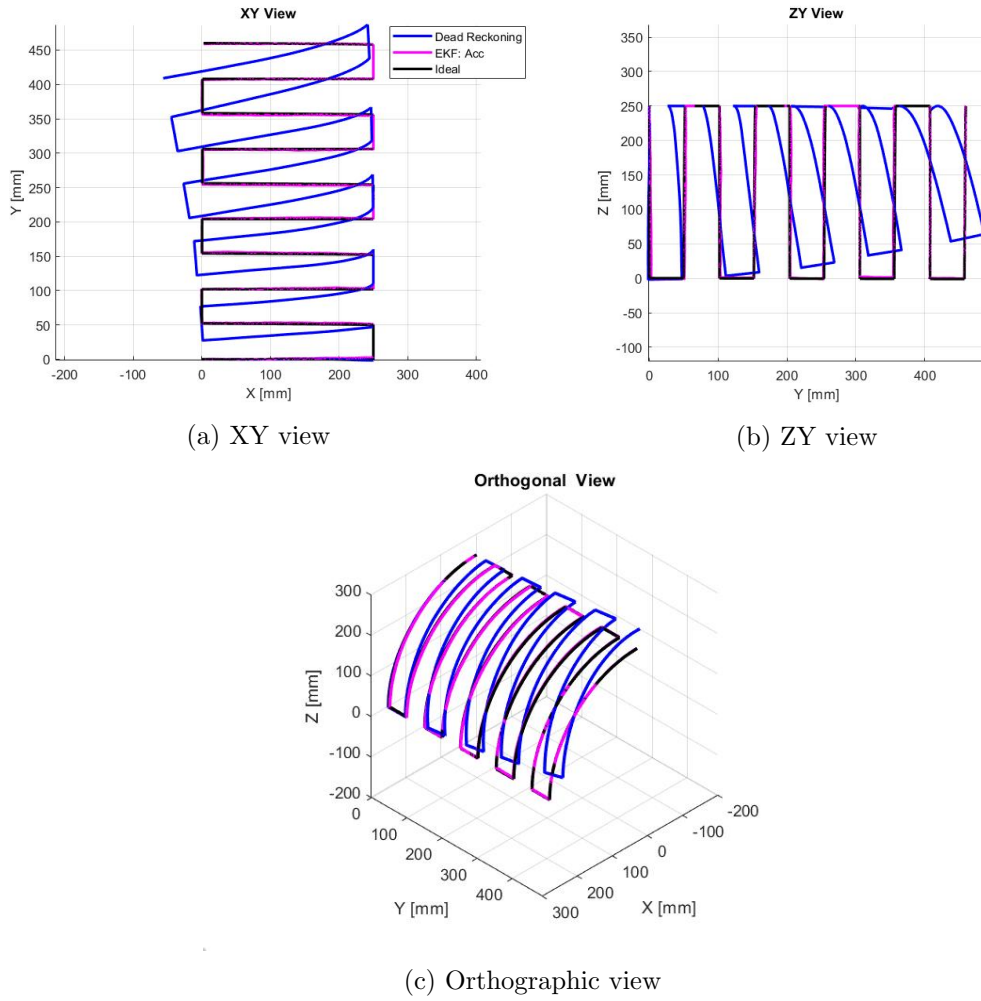
Figure 6.13: Dead Reckoning and EKF using accelerometer angles to correct position and orientation results for a single trial for raster scan on a pipe surface

148
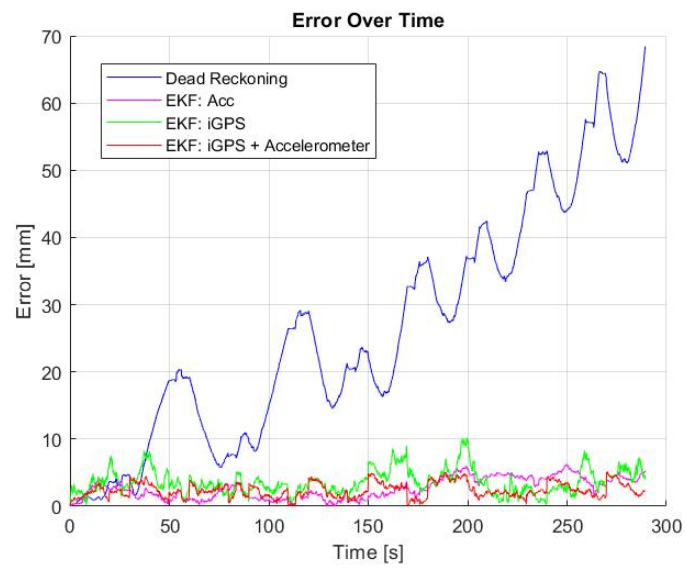
Figure 6.14: Graph showing the cumulative error along the surface of the pipe during typical raster scan for each of the EKFs and dead reckoning using wheel encoders

(a) Acceleration vs. Dead Reckoning

(b) Comparison of EKFs

(c) Comparison of EKFs and Dead Reckoning
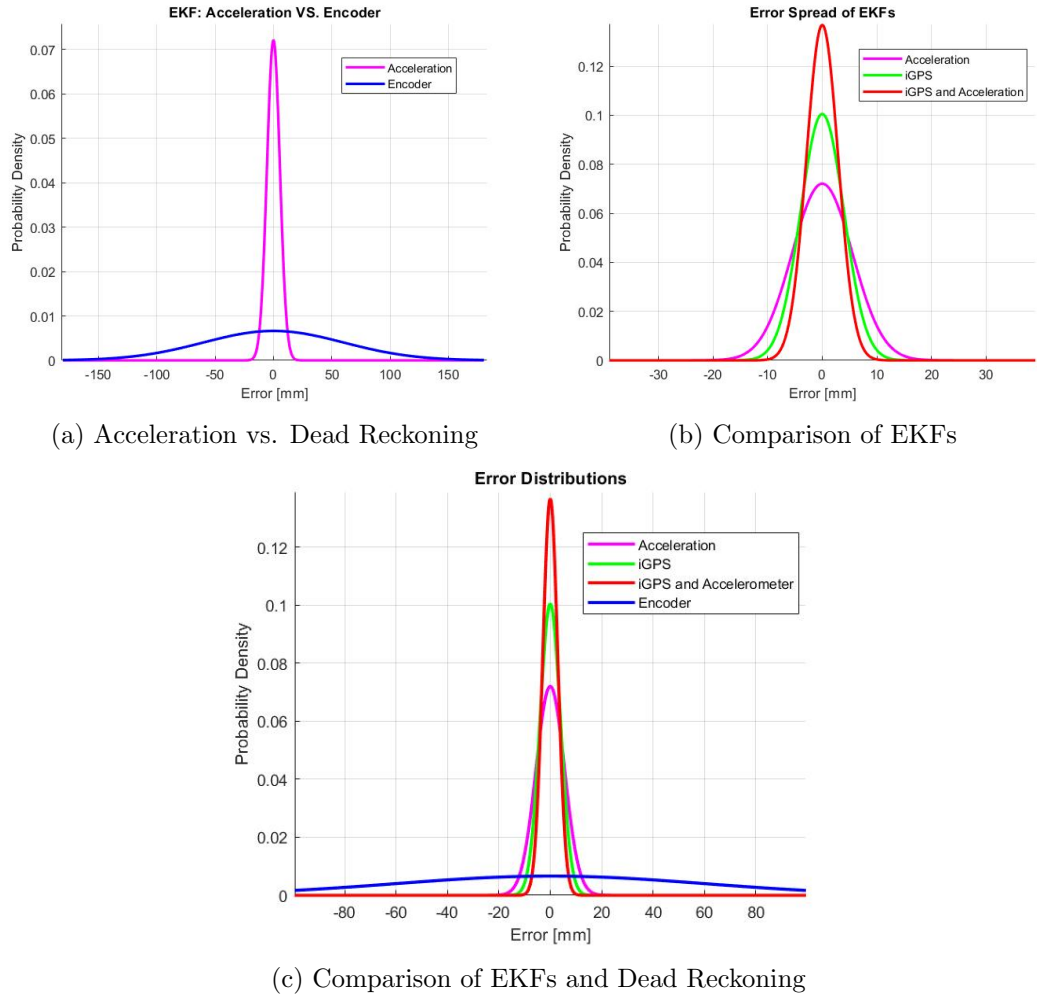
Figure 6.15: Comparison of distributions of error along the surface of the pipe between the end point of the measured positions and the ideal end point

Table 6.3: Table showing the standard deviations of the error distributions for a raster scan on the pipe

Measurement	Standard Deviation [mm]
Dead Reckoning	62.22
Acceleration Angles	5.40
iGPS	1.99
iGPS and Angles	2.88

6.5.2 Conclusion

This section shows how the work done in previous chapters to determine the ω and α angles can be used to correct the position of a device. A robot was simulated going around the circumference of a pipe using modified differential drive kinematic equations and an EKF was designed to fuse the angles and encoder values. This was implemented and shows significant decrease in the positional error for both a single rotation around a pipe, and multiple rotations around a pipe. It should be highlighted again that the iGPS measurement considered here are from an ideal system, where there is complete coverage and no interference of the signals from the pipe. In practice, this is not the case, as the pipe will obstruct iGPS measurements, and obtaining line of sight around the full pipe is impractical. Not only this, but the extra steps of setting up an iGPS system makes this method more impractical for on-site inspection. These simulations show that it is possible to gain a majority of the positional accuracy obtained from an ideal iGPS system, by using an onboard accelerometer which omits the disadvantages mentioned previously. Unfortunately Covid-19 restrictions prevented experimental validation of the simulations and models developed in this chapter.

Chapter 7

Productisation at Eddyfi Technologies

The work described in this thesis serves as a foundation for a positioning system which Eddyfi Technologies is employing to enhance the positioning capabilities of existing products. The productisation of this work is being conducted by the Technology Team at the Eddyfi Technologies Centre of Excellence for NDT Scanner Positioning based in Swansea. The work demonstrated in this thesis is being utilised to create a circumferential positioning encoder and the feasibility of its integration into Eddyfi products has been tested using the Spyne system (shown in Figure 7.1).

Figure 7.1: An image of the Eddyfi Spyne system being used in field.

7.1 Problem Statement

Eddyfi Technologies has a number of commercial hand held and automated solutions designed for the inspection of pipes, these were discussed in Chapter 2. There are several challenges that Eddyfi Technologies are attempting to overcome when it comes to positioning of NDT sensors on pipe surfaces. The main issues addressed though the productisation include:

- **Account for the corkscrew effect:** Following a straight horizontal path along a pipe is difficult and not always achievable. This can be caused by the weight of the device with the influence of gravity pulling downwards. This can cause the path of the scanner to corkscrew with the effect becoming more pronounced over longer distances. This is shown in Figure 7.2. Even if the pipe is gridded, it can still be difficult to fully observe and take into account this behaviour.

- **Ensuring sufficient coverage:** Incomplete inspection coverage of an asset can lead to defects being missed. This can be achieved by showing that a scan has sufficient overlap. Some Eddyfi products already feature a "Grid-as-

U-Go" feature described in Section 2.4, where the user is required to enter the starting circumferential position and the scanned area is physically marked onto the surface as the scan is conducted. The region is outlined and the scan tracks marked out (based on the width of the scanning tool with a percentage overlap) onto the surface with a pen to help guide the user. When the indexing button is pressed, the software assumes that the scanner is placed in the exact position for the adjacent track. This is highly unlikely to be carried out in the field for all adjacent tracks during the inspection and so there is a potential for defects to be duplicated or missed altogether if there is no scan overlap. This method allows users to check for insufficient coverage, however any deviation from the ideal path is not considered in the processing of the data on the system.

- **Obtain real time positioning information:** Real time tracking and positioning updates will help guide operators to ensure full inspection coverage. Recording the orientation of the device around the pipe from the start to the end position will automatically account for any drift around the pipe and place defect indications in the correct spatial position. With this research, continually measuring the circumferential position of the device during the scan and updating this position for the recorded data automatically will enable more accurate defect localisation.
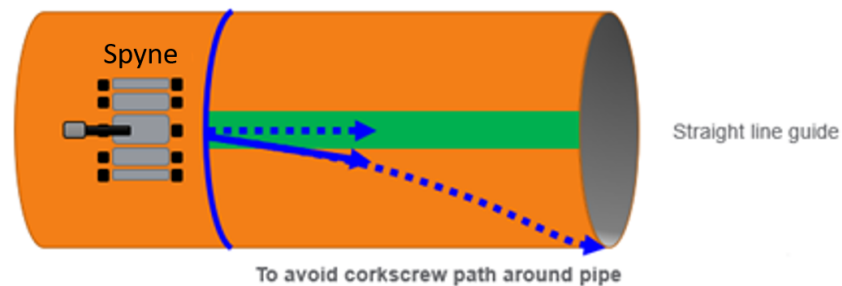
Figure 7.2: Schematic showing the discrepancy in path as a result of the corkscrew effect when attempting to scan along a horizontal pipe due to gravity and human error.

The value of integrating this EngD research with manual inspection devices is to reduce

human error introduced by the gridding process, manual position and assumption of the location of adjacent tracks by the software. The idea is that the a modified probe shell, which incorporates 3 points of contact, and accelerometers can be used to calculate the position of the scanner on the pipe and display it in real-time to the user. The position of the probe on the pipe in real time can then be shown to the inspector. The advantages of this are:

- Removes gridding process, making overall inspection time quicker

- Can improve coverage as inspectors can see if there is incomplete coverage

- Removes human factors such as the inspectors ability to follow the grid, which can deteriorate with inspector fatigue and inexperience.

At the time of writing, Eddyfi are prototyping and developing a system for their Spyne product, as shown in Figure 7.1, which uses accelerometer readings to enhance the "Grid-as-U-Go"functionality. With the proposed enhancements, the user will be able to view the projected trajectory of the scan in the software and observe any unscanned areas. Implementation of this work aims to improve the efficiency of the setup process by further automating the "Grid-as-U-Go" system and enhance the accuracy of defect positioning of the Spyne system. Integrating into the Spyne will provide increased efficiency and accuracy of defect location through automated gridding, enhanced digital twinning, and reduced human error. The projected manufacturing cost of the accelerometer based system is estimated to be in the region of $USD 400 with a target sale price of $USD 2500. The Spyne is the first application from the Eddyfi Technologies pipeline tool set where this research is being applied, however feasibility is also being explored for the integration of this work into the PipescanHD and PECA product lines where this technology can be applied to gain similar benefits as mentioned above.

7.2 Technical Description

This section describes how the work presented in this thesis has been modified by the Technology Team at Eddyfi Technologies to meet requirements of the Spyne scanner. Research Engineer Ralf Leib conducting a large part of the integration work.

7.2.1 Accelerometer Work

The accelerometer used for the prototype is a Bosch BMX160 IMU. This accelerometer was used opposed to the Xsens MTi-300 as it is much more cost effective at a price point of £30 and has a faster output rate. Two accelerometers are used in a Galperin setup [118], where the second accelerometer is rotated by 45° in both roll and pitch. The Galperin configuration was first utilised in the oil & gas exploration sector and in commonly used in seismology applications [119]. This configuration ensures that each of the axis is affected by gravity equally [119]. The information from the second accelerometer is used to make calculations on a non horizontal pipe more accurate and as a second source to measure the orientation and position on the pipe surface for measurement fusion to reduce noise and increase accuracy of the overall measurement. The Galperin is primarily for sensitivity improvement at different azimuth angle but also when on top and on bottom of a pipe. A schematic of this setup is shown in Figure 7.3, where the Galperin coordinate systems are shown with reference to a horizontal pipe. Figure 7.4 shows an image of the device prototyped by Eddyfi Technologies. One added assumption to the model here is that the device is facing down the axis of the pipe, and therefore the roll of the device can be directly translated to the position angle on the pipe.

$$\begin{bmatrix} x \\ y \\ z \end{bmatrix} = \begin{bmatrix} -\sqrt{\frac{2}{3}} & \frac{1}{\sqrt{6}} & \frac{1}{\sqrt{6}} \\ 0 & \frac{1}{\sqrt{2}} & -\frac{1}{\sqrt{2}} \\ \frac{1}{\sqrt{3}} & \frac{1}{\sqrt{3}} & \frac{1}{\sqrt{3}} \end{bmatrix} \begin{bmatrix} u \\ v \\ w \end{bmatrix}$$

$$\begin{bmatrix} u \\ v \\ w \end{bmatrix} = \begin{bmatrix} -\sqrt{\frac{2}{3}} & 0 & \frac{1}{\sqrt{3}} \\ \frac{1}{\sqrt{6}} & \frac{1}{\sqrt{2}} & \frac{1}{\sqrt{3}} \\ \frac{1}{\sqrt{6}} & -\frac{1}{\sqrt{2}} & \frac{1}{\sqrt{3}} \end{bmatrix} \begin{bmatrix} x \\ y \\ z \end{bmatrix}$$
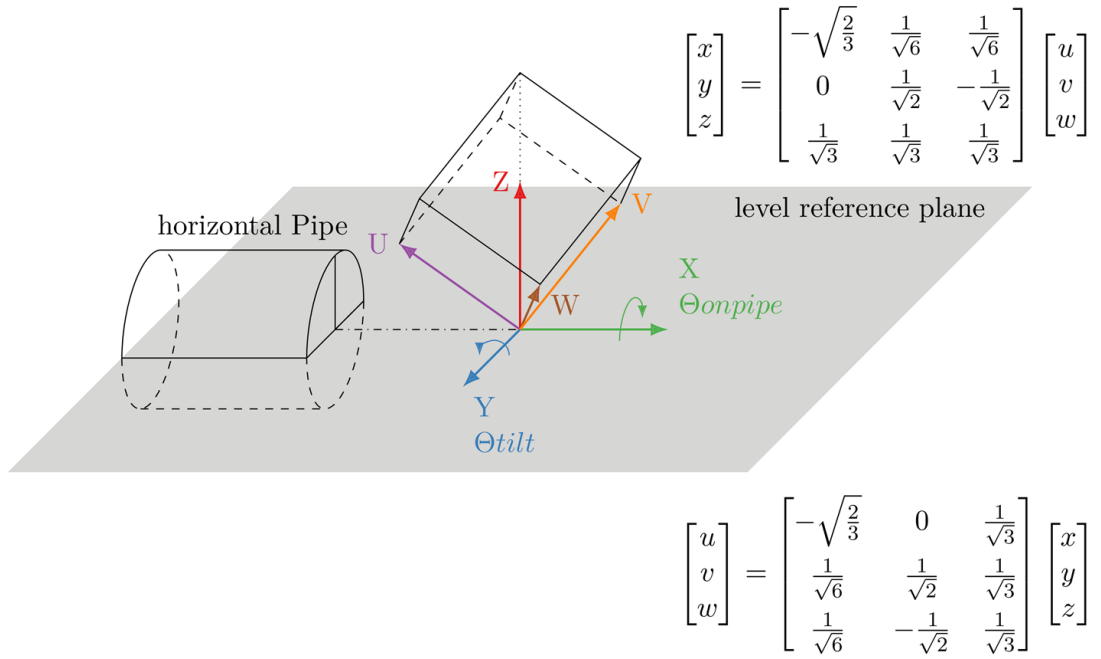
Figure 7.3: Schematic showing the coordinate system of 2 accelerometers in a Galperin setup, where one accelerometer is in a standard configuration with axis XYZ and another is is offset by 45° with the axis UVW.
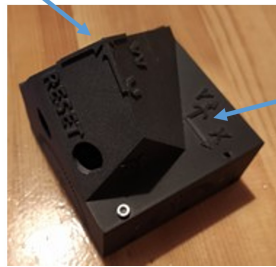
Figure 7.4: An image of the outer casing of the prototype device showing the Galperin and standard accelerometer coordinate systems currently being used at Eddyfi Technologies to test feasibility.
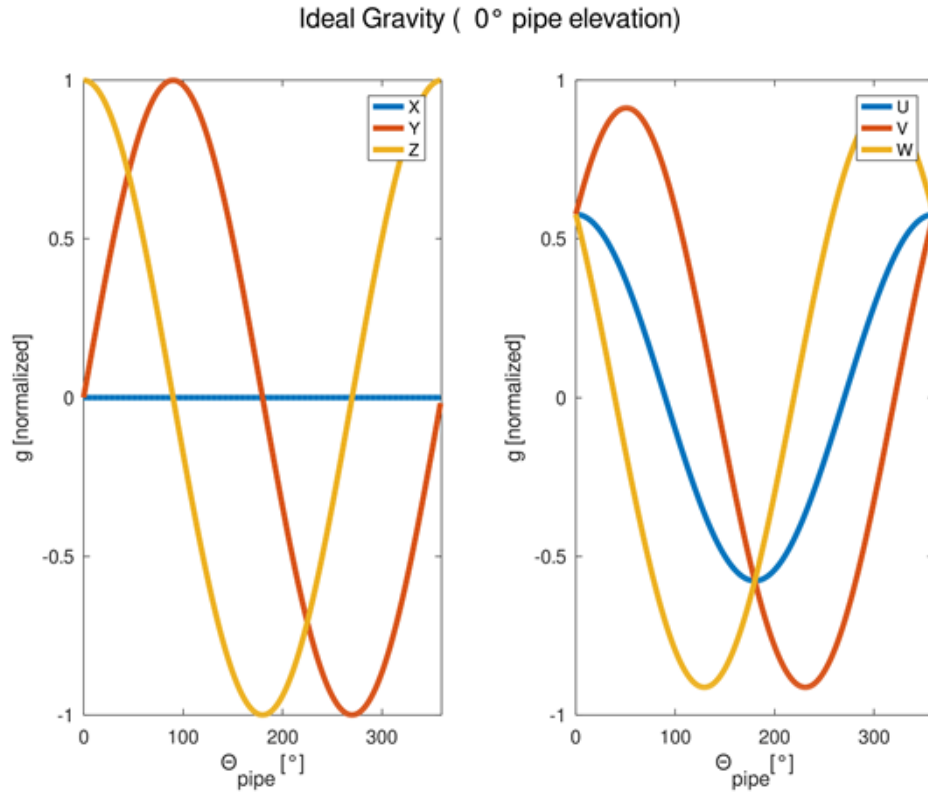
Figure 7.5: Graphs comparing the 3 axis accelerometer outputs from the standard (XYZ) and Galperin (UVW) configurations around a horizontal pipe showing that for the standard accelerometer configuration, the X acceleration remains 0, whereas the corresponding U acceleration changes.

Figure 7.5 shows that as the device is positioned at different circumferential positions around the pipe, the standard accelerometer X axis, when laid perpendicular to gravity, does not provide any information as it is a always 0. With the Galperin setup, the corresponding U axis changes with the rotation, allowing it to be used in the position calculations. Gyroscope measurements were investigated, however as the theory predicts, this introduced integral error, although the noise was significantly lower than that of the accelerometer.

7.2.2 Application of Filter Work

The aim of implementing a filter is to reduce the noise of the calculated angle. Three types of filters were tested. A low pass filter was introduced to reduce the noise from the accelerometer, however this was found to be slow to react or did not reduce noise to a suitable level. It was concluded that increasing the number of parameters and creating more complex models would be a challenge given the budget and the limited onboard computing power available. Consequently, the Unscented Kalman Filter (UKF) was used instead. The UKF is a particle filter where the state is projected forward N+1 times, with each result weighted and the average of the results it taken as the estimate of the next state. An overview of the UKF is described in [11]. Figure 7.6 shows an example of this illustrating how the perturbations are averaged to obtain the current state estimate.
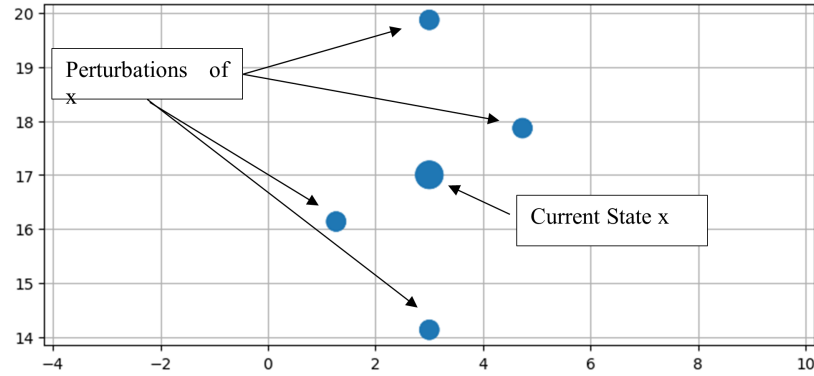
Figure 7.6: Example graph showing an arbitrary case where x has been perpetuated 4 times, with the weighted average of the results estimating the current state of x

The state equations used to perpetuate the current state forward N+1 times are given below.

State Equations:

$$\hat{x}_t = \begin{bmatrix} \omega_t \\ \dot{\omega}_t \end{bmatrix} = \begin{bmatrix} \omega_{t-1} + \dot{\omega}_{t-1}\Delta T \\ \dot{\omega}_{t-1} \end{bmatrix} \tag{7.1}$$

Measurement Model:

$$z = \begin{bmatrix} 0 \\ 9.81 * \sin(\omega) \\ 9.81 * \cos(\omega) \end{bmatrix} \tag{7.2}$$

Where; ω is the clock face angle and $\dot{\omega}$ is the rate of change of ω.

This simplified model is acceptable as the use cases are constrained to a device assumed to be orientated along the axis of the pipe. Deviations from this are expected to cause errors in the positional estimate and will be investigated further at Eddyfi Technologies. Figure 7.7 shows an example of the UKF being used illustrating the stability of the filter when erratic behaviour outside the norm is introduced to the system. In this case, samples 5500 - 18000 show a repeating signal with high variation in the angle with the UKF remaining stable throughout.
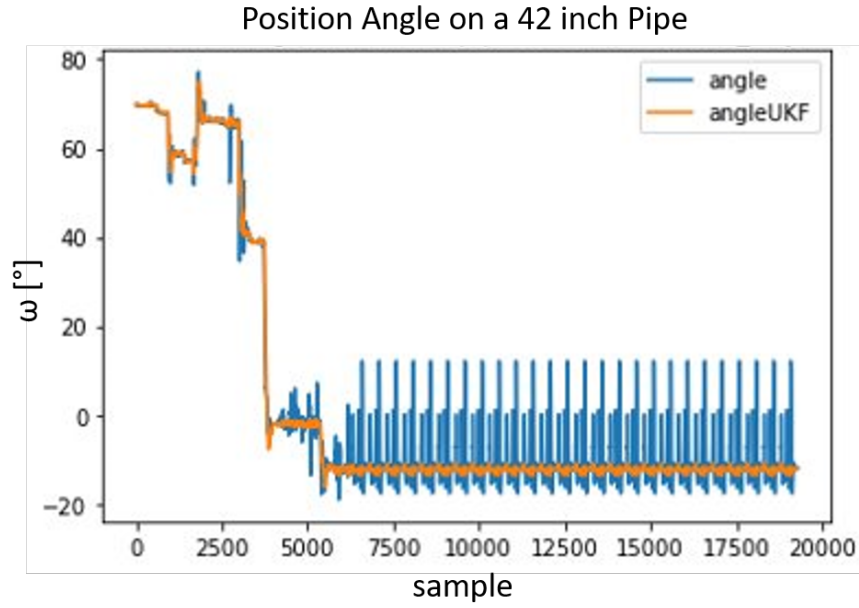
Figure 7.7: Graph showing the results of the angle measured directly from the accelerometer (blue) compared with the UKF filtered result (yellow), where an impact signal was added to the end multiple times to test the stability of the UKF.

7.3 Proposed Solution

The solution proposed by Eddyfi is a circumferential Positioning Encoder (CPE) which utilized an IMU to determine the circumferential position on a pipe for the Spyne system. The solution uses two IMUs mounted at 45° in the XY and XZ planes which adds more information as shown previously. Vertical pipes are not possible with this approach due to the constant direction of gravity downwards.

A Bayesian filter in the form of a UKF smooths calculated angle to improve the positional accuracy throughout the scan. This, coupled with the wheel encoders, ensures that each NDE measurement can be positioned on C-Scans and show circumferential movements occurring during the scan. The clear benefit to this approach is the automatic gridding approach fro the Spyne.

The Spyne users will benefit from increased efficiency and positional accuracy as the

161

clock angle of the system is automatically recorded. The stream of clock positions calculated from the accelerometer outputs can be used to monitor the trajectory of the Spyne and warn the inspector if the path is veering off course due to gravitational, environmental or pipe conditions. An example of this is shown in Figure 7.9, where the software shows the areas which have not been scanned. The inspector can then correct the trajectory or complete another scan which cover the missed areas. Ultimately, this method helps to control human factors which affect the scan quality. These mainly being imperfect alignment of the Spyne for subsequent scans and incomplete coverage due to the factors mentioned previously. Overall the efficiency for the operators will be improved and the reliability of the scans are increased. One major advantage of using this system compared to a a system with 2 wheel encoders is that the slippage of the device can be measured using the accelerometer readings, but not with the wheel encoders. This more accurately shows an operator if full coverage has been achieved.
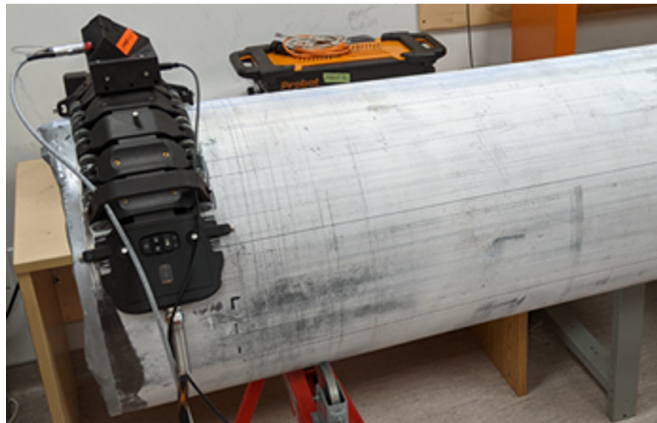
Figure 7.8: Example setup of a Spyne system for axial scans along a pipe to capture C-scan data.
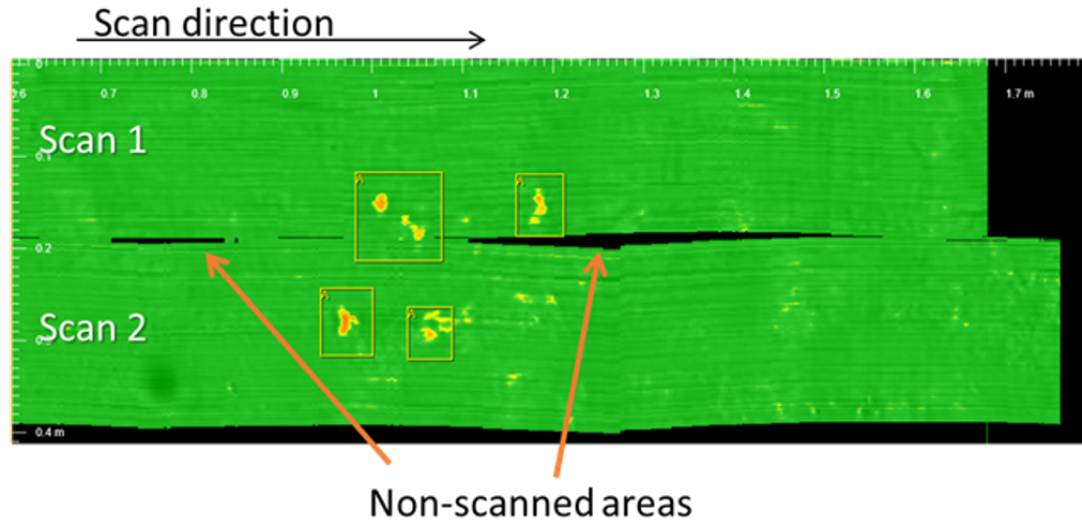
Figure 7.9: Example output of a C-Scan showing the trajectory of two separate Spyne scans where the system recognises that full coverage is not achieved using CPE prototype.

Accurate positioning for the NDE scans and correctly stitching the data is key to monitoring defects and applying repairs. It is also important for defects which may cross the scan boundary and span multiple scans. This method will reduce situations where the same defect is shown multiple times on multiple scans as a result of being mispositioned or not considering suitable overlap. This makes the overall scan more reliable and increases the integrity of the data collected.

7.4 Vertical Pipes

Vertical pipes pose another challenge when considering pipe inspection. The method described in this thesis can not be used as with vertical pipes, the gravity vector can only be used to determine the orientation on the pipe, however it contains no information about the clock-face angle as at all clock-face angles the accelerometer output will be the same.

In non-industrial settings, the magnetometer in the IMU can be used. However, as

described previously, local magnetic deformations due to the ferrous material in the environment make this method unusable. Therefore, the gyroscope measurements are seen as the most suitable onboard system to combat this problem. Although this is a relative measurement and will be subject to drift over long periods of time. Figure 7.4 shows a schematic of the vertical pipe problem.
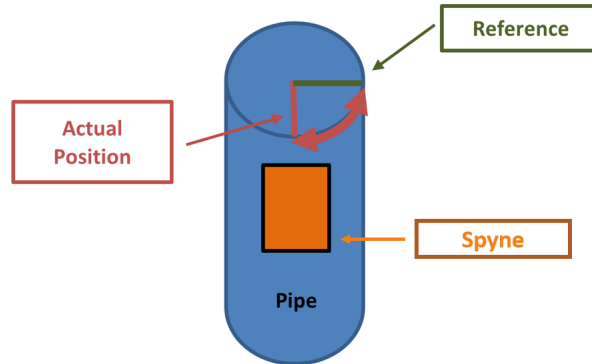
Figure 7.10: Schematic of the vertical pipe problem showing clock face position relative to a given reference point

Figure 7.11: Spyne setup on a vertical pipe with the MTi-100 IMU attached

Figure 7.12 shows the output of the gyroscope and 3-axis accelerometer, showing the yaw angle from the gyroscope drifting between $\pm 1.5°$ and the stability of the accelerometer readings in the 3 axis while stationary. In tests conducted by Eddyfi, over multiple scans the gyroscope experienced drift of up to $10°$ for 5 scans of 500mm length. The engineers at Eddyfi concluded that this fluctuation and drift are too large for this application.

Possible solutions include using a much higher spec gyroscope at an increased cost, but with less drift. An on-board camera system could be utilized to perform visual odometry by tracking features to determine the change in orientation and position of the system [33]. Another option which will be investigated are outside-in systems such as iGPS or LiDAR systems coupled with sensor fusion though Bayesian filters. There is also the possibility to use computer vision for robot localisation. The research presented in Chapter 3 and 4 form the basis of the feasibility study conducted by Eddyfi Technologies.
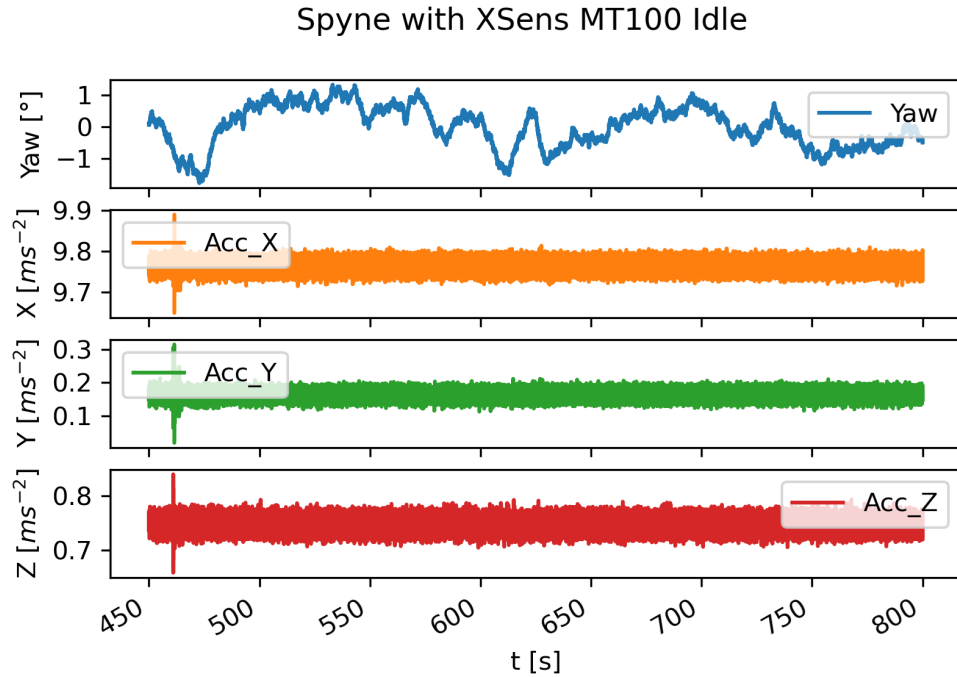
Figure 7.12: Results of the the gyroscope and 3-axis accelerometer for a stationary Spyne system on a vertical pipe

7.5 SWOT Summary and Conclusion

A summary of the Strengths, Weaknesses, Opportunities and Threats is given below for the CPE implemented on the Spyne system above: **Strengths:**

- Reduce scan setup time: No pre gridding necessary.

- Enhanced positioning: Ensure inspection coverage real time via software and warn of scanner drift.

- Ease of use: reduces the amount of work and reliance on an individual inspector.

- Low cost: tested using £20 IMU and £50 dedicated PCB.

- Absolute positioning: No integral error is present as the measurement is taken with respect to gravity, which is deemed constant.

- Self-contained: The system does not require external beacons or base stations to be set up.

Weakness:

- Limited use cases: Accuracy deemed acceptable for horizontal pipes, however at pipe angles of 50° to 90° (vertical), method is not viable.

- Axial positioning is lost when device is removed form surface.

Opportunities:

- Automation: First step towards automated positioning in the Eddyfi scanner product range.

- Modularity: System can be added as an accessory with little to no changes required, for other products from Eddyfi Technologies.

Threats:

- Vertical pipes: No capability for vertical pipes

- Accessory marketing: Unclear if customers will be willing to pay for an accessory, or if the device should be fully integrated into existing products.

There are benefits of incorporating a CPE to manual scanners such as the Spyne. The main benefit being that the position of the scanner can be tracked resulting in better coverage as well as the other benefits mentioned above. At the time of writing, Eddyfi Technologies are currently investigating the feasibility of patenting this system based on the research done in this thesis.

Chapter 8

Conclusion and Future Work

8.1 General Overview

An algorithm was developed to obtain an absolute measure of the position and orientation of a robot or probe on a pipe. A thorough body of work encompassing the current capabilities of mobile robotic pipe inspection in industry and the contributions to the field has been presented. The limitations and challenges of localisation on pipes for automated inspection as been discussed. The presented work addresses some of these limitations with regard to the limited positioning capabilities of automated pipe inspection, providing a new novel approach to overcome localisation challenges with the potential to make the inspection process simpler, quicker and more cost effective overall. The algorithm developed is a step towards the longer term goal of automated and autonomous robotics of pipe inspection over long periods of time with minimal to no human interferences.

A novel method of obtaining an absolute measurement of the positional clock-face angle (ω) and the orientation angle (α) using an onboard accelerometer has been presented. This method does not require any external sensors to be used and is not subject to integral error over time as it does not require integration of the accelerometer signals and provides an absolute measure of these values referenced to gravity. This is achieved

through the development of a mathematical model which explains the relationship between the ω and α angles with the 3-axis accelerometer readings for a 3 point-of-contact robot. This is done by first determining the 3 points of contact on the pipe surface, ensuring that the geometry of the robot is conserved using the intersection of 2 perpendicular cylinders and a cylinder and sphere in the analytical model. From these 3 points, the X, Y and Z axis' of the modelled accelerometer are determined and their values are calculated from the gravity vector. This forward model provides an in-depth view of how a robots position and orientation on a pipe surface affects the accelerometer readings. The development of this model allows for any combination of α and ω to be simulated, and their corresponding accelerometer readings and wheel positions to be calculated analytically.

The inverse model is found using a least-mean squared optimisation method due to the relationship from accelerometer readings to α and ω angles being ill-posed. The cost function of the optimisation is the root mean squared difference between the real accelerometer output and the forward model accelerometer readings calculated, with α and ω being the changable variables. Experimental validation of the mathematical principles was conducted using a Vicon photogrammetry system and a 3 point-of-contact rig with a mounted accelerometer and shows an accuracy of $\Delta\alpha = 3.40°$ and $\Delta\omega = 4.17°$.

An error analysis was conducted to characterise how different environmental aspects which are likely to vary in real world settings, such as angle of pipe and ovality of pipe, to determine how these characteristics will affect the results of the algorithm developed.

Fusion of these measurements and the other existing methods of measuring the pose of a robot was completed though the development of Extended Kalman Filters. A number of EKFs were formed to compare their accuracy through simulations, showing how the novel method of using accelerometer readings can be used as a substitute for other absolute measurements such as iGPS. A kinematic model of a differential drive robot on a pipe was defined for use in the state update equations in the EKFs. The

169

simulations were run 10,000 times and the distributions of the final difference between the measured and ideal states were recorded. These simulations show an improvement in positional error on the pipe surface over one revolution from a variance of 7.08 mm for dead reckoning and 3.01 mm for an EKF fusing wheel encoder and angle measurements.

The industrial sponsor, Eddyfi Technologies, is commercialising this work and testing the feasibility of its implementation to current products. Work has been conducted to incorporate accelerometers to measure the clock face angle for the Eddyfi Technologies Spyne system. At the time of writing, this work is being extended by the engineering research team to incorporate an extra accelerometer in a Galperin setup to increase the sensitivity of the calculations. Research into extending this work to vertical pipes though the use of magnetometers and gyroscopes is also being investigated.

8.1.1   Benefit to Other Products

Eddyfi Technologies has a number of hand held probes, such as the PEC and Sharck probes. Figure 8.1 shows the underside of an Eddyfi Sharck Probe with 3 wheels, which can be considered as 3 points of contact, making this probe a good fit for this research conducted in this thesis to be integrated with as there is minimal redesign work required. An accelerometer needs to be added to the system, which can potentially be incorporated in the form of a clip-on attachment or integrated in the future designs of the probe in a similar fashion to the Spyne.
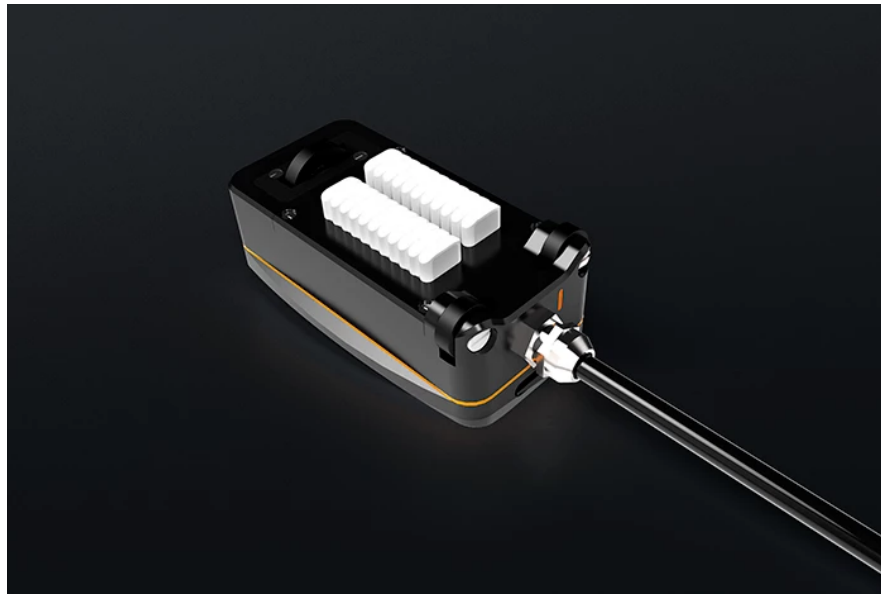
Figure 8.1: Eddyfi Sharck Probe Underside

Figure 8.2: Eddyfi Single Element PEC Probe

The inspection process using a hand held probe with this work integrated could be as follows:

1. Place probe on pipe

2. Capture NDE scan

3. Press button to capture position and orientation using the method detailed in this thesis

4. Move probe to new inspection position

5. Repeat, checking scan map for full coverage

8.2   Future Recommendations

There are a number of recommendation and refinements for future work extending from the research completed in this thesis. This work also lends itself to a more autonomous future for pipe inspection robotics.

Short Term Refinements

While the mathematical principles developed in this work show that the algorithm can be modified to take into account the angle of the pipe, this work has not been tested for angled pipes. Simulations show that as long as the angle of the pipe is known, the position and orientation can be determined from the accelerometer readings.

Another limitation of this work in its current form is that it is not suitable for vertical pipes. This is because at all circumferential positions on a vertical pipe will have the same accelerometer readings as gravity will always be acting in the same direction relative to the 3-axis of the accelerometer or robot. While this is the case for the ω angle, it is theoretically possible for the α orientation angle can be calculated using this method. A hybrid method where gyroscope and encoder measurements could be used to obtain a better positioning estimates when compared to relying on encoders on their own. There would still be integral error present with this method, however, as the orientation measurement form the accelerometer would be an absolute measurement,

the overall error would be expected to be significantly lower over longer periods of time.

This work requires a settled state for the accelerometer readings to be used. Further work should be done to characterise how motion of a robot would affect the measurements and to see whether or not the motion of a robot needs to be considered and at what velocity the motions effect on the results can be considered acceptable or negligible.

Further work would fuse gyroscope measurement to improve the accuracy of the position and orientation estimations though their integration into the EKF which has been developed. In terms of the physical gyroscope, the addition of this to a system is negligible as gyroscopes are already a standard part of an IMU.

While the principles on which Kalman Filters are based on are well understood and have been implemented in many industries, short term future work could include experimental validation of the EKFs designed in this thesis using a robotic platform with real, rather than simulated, measurement values. This was not completed in this research due to time constraints brought on by the current pandemic.

8.2.1 Long Term Vision

As described previously, this work is a step towards having an autonomous system which would be able to conduct scans over long periods of time without the increasing integral error associated with current positioning systems.

Synchronous Drive Robotic Platforms

This work lends itself to be used as part of a synchronous system of pipe inspection robotics. NDE methods such as Time of Flight Detection (TOFD), Multi-skip (M-skip) or other pitch catch methods which require a emitting probe and a receiving probe. The placement of these probes in relation to each other have a significant effect on the ultrasonic reading, with Lorenz et al [120] citing that alignment between the pitch-catch probes needs to be below 2°. A current system for M-skip relies on braces or on encoder positioning as seen in Figure 8.3.

Track systems are cumbersome while wheel encoder based systems become more inaccurate over time. Therefore, a system based on the presented work which uses an accelerometer to measure the absolute clock-face angle and encoder readings fused together in EKF could solve this problem.

Figure 8.3: Sonovation M-Skip Setup
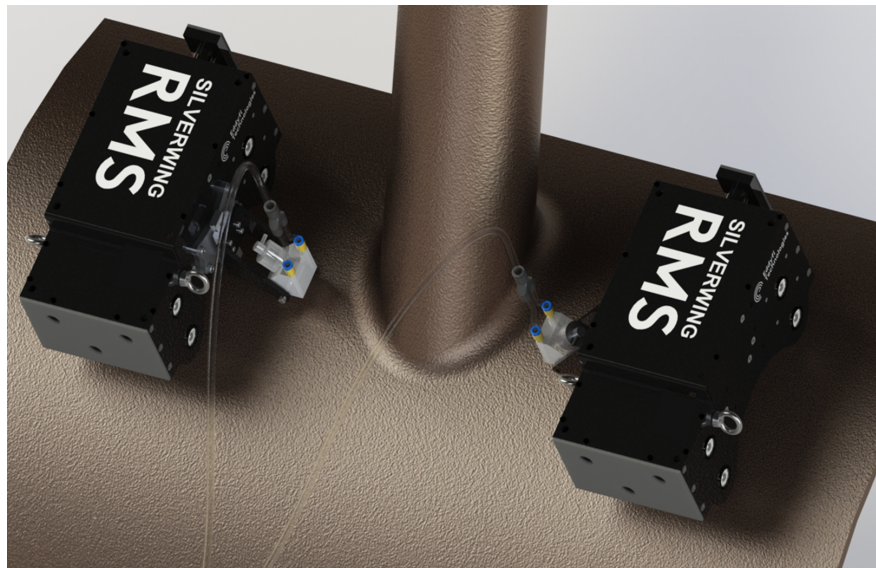
Figure 8.4: Rendered image of the Eddyfi Silverwing RMS platform being used in a synchronous pitch-catch setup

A general purpose pipe inspection differential drive robot using this positioning system could be used as part of a synchronous system and would reduce the overall cost of inspection for asset owners as it could remove the need for platforms and solutions which are specialised for a specific inspection type. A modular design would allow for

the probe attached to the robot to be swapped out depending on the needs of the asset owner.

Machine Vision Integration

A stated previously, the method developed in this thesis is not designed to be a stand alone positioning solution, especially when considering robotic platforms. Integrating the absolute angles calculated here with measurements from other sensors will provide the greatest benefit to mobile robotic systems. One group of complimentary positioning method are visual methods, such as visual odometry and machine vision. A camera system is also an onboard measurement system and further advance the positioning capabilities of a mobile robotic system only using onboard sensors.

Integrating a camera to the system would give more measurements, but also allow operators to see from the perspective of the robot for manual control or visual inspection. This may be useful from a productisation perspective as many companies are investigating the role that VR and telepresence can play in the inspection process.

Conclusion

The main findings as a result of the research are as follows:

- It is possible to obtain absolute measure of the position and orientation on a pipe surface using an onboard accelerometer and knowledge of the geometry of the system

- An EKF can be used to correct encoder position values on a pipe using the angles calculated from accelerometer readings

- Simulations show that encoders combined with the angles calculated from an accelerometer in an EKF show a positional accuracy of 73% of an ideal simulated iGPS system without the need to set up external equipment over a single revolution around a pipe

- A positioning system using the methods in this thesis can be made for $< \pounds 500$ while having an error of less than $5°$

With accurate positioning, path planning and execution on pipes could be achieved to deliver more autonomous robotic systems for defect mapping. Planning and execution of raster scans or saddle weld inspections are possible.

8.3   Final Thoughts

The Non-destructive Evaluation process is inevitably moving towards a more automated and robotic future. While industry is moving ahead with further automation, there are still many challenges that are present which prevent the implementation of fully autonomous solutions. One of these, obtaining accurate pose estimates for long periods of time for pipe inspection, is addressed in this thesis. This research has led to the development of a new circumferential encoder system at Eddyfi Technologies which will be used to improve reliability of manual and automated inspections. This research has led to improvements to existing products at Eddyfi which will be commercially implemented to improve positional accuracy of NDE scans.

Appendix A

Appendix

A.1 Other Robot Adhesion Types

A.1.1 Negative Pressure

The principle of using negative pressure for robot locomotion is to create a suction force between the robot and the surface which overcomes the force of gravity to ensure that the robot adheres to the surface. This can be done though suction cups, or by creating a vacuum. The main advantage of using such systems is that they can be used on non-magnetic surfaces.

Suction Cups

Suction cups are usually used on leg-type robots. These are more complex mechanically and kinematically compared to wheel or track systems. Steps need to be taken to ensure that the suction force is sufficient before the robot can proceed with the next step in its motion [**rosa˙low-cost˙2002**]. Another drawback of suction cup robots is that their locomotion is comparatively slow compared to other methods [121]. The main advantage of this setup is that there is no magnetic force, meaning that the robot can be used to inspect assets which are non-magnetic, such as assets with layers of insulation.

Vacuum Adhesion

Vacuum adhesion works by creating a suction force between the robot and the asset. One of the main drawbacks for using this method is that if the vacuum stops, the robot no longer has any adhesion force, meaning that the robot will fall. This can cause damage to the system, asset or even humans meaning these kinds of systems may not be not intrinsically safe. Traditional propeller based vacuum robots are suitable for wide flat surfaces [122]. Curved or irregular surfaces can reduce the adhesion force. Other drawbacks include the inability to climb coarse walls and poor ability to overcome obstacles and the energy is required to generate the suction force [123].

A.1.2 Bio-Mechanical

Biomechanical adhesion aims to duplicate the structure of the biological feet of animals such as geckos. Typically, they can be used on most surfaces and do not require power to maintain adhesion, however they can be sensitive to dusty surfaces and only generate low adhesion forces [123][124]. Another issue is that if the adhesive surface becomes dirty from the asset surface, the adhesive force can be reduced [125].

Bibliography

[1]   Michael Peshkin and J. Edward Colgate. "Cobots". In: *The Industrial Robot* 26.5 (1999), pp. 335–341. ISSN: 0143991X.

[2]   Tommaso Pardi et al. "Planning Maximum-Manipulability Cutting Paths". In: *IEEE Robotics and Automation Letters* 5.2 (Apr. 2020), pp. 1999–2006. ISSN: 2377-3766.

[3]   Kathleen A. Kas and Gary K. Johnson. "Using Unmanned Aerial Vehicles and Robotics in Hazardous Locations Safely". In: *Process safety progress* 39.1 (2020). ISSN: 1066-8527.

[4]   Randika K.W. Vithanage, Colin S. Harrison, and Anjali K.M. De Silva. "Autonomous Rolling-Stock Coupler Inspection Using Industrial Robots". In: *Robotics and Computer-Integrated Manufacturing* 59 (Oct. 2019), pp. 82–91. ISSN: 07365845.

[5]   Youyu Wang et al. "Review of Research on the Chinese Space Station Robots". In: vol. 11743. Lecture Notes in Computer Science. Cham: Springer International Publishing, 2019, pp. 423–430. ISBN: 978-3-030-27537-2.

[6]   R. Summan et al. "Practical Constraints on Real Time Bayesian Filtering for NDE Applications". In: *Mechanical Systems and Signal Processing* 42.1-2 (Jan. 2014), pp. 181–193. ISSN: 08883270.

[7]   S. Gareth Pierce et al. "Positioning Challenges in Reconfigurable Semi-Autonomous Robotic NDE Inspection". In: SPIE Smart Structures and Materials + Nondestructive Evaluation and Health Monitoring. Ed. by Tribikram Kundu. San Diego, California, USA, Mar. 25, 2010, p. 76501C.

179

[8] M. Morozov et al. "Assessing the Accuracy of Industrial Robots through Metrology for the Enhancement of Automated Non-Destructive Testing". In: *2016 IEEE International Conference on Multisensor Fusion and Integration for Intelligent Systems (MFI)*. 2016 IEEE International Conference on Multisensor Fusion and Integration for Intelligent Systems (MFI). Baden-Baden, Germany: IEEE, Sept. 2016, pp. 335–340. ISBN: 978-1-4673-9708-7.

[9] ASME. *Process Piping - AMSE Standards B31.3*. 2020th ed. ASME. 544 pp. ISBN: 978-0-7918-7366-3.

[10] American Petroleum Institute. *Tank Inpsecion, Repair, Alteration and Reconstruction: API Standard 653*. 5th Edition. American Petroleum Institue, Nov. 2014.

[11] S. Thrun, W. Burgard, and D. Fox. *Probabilistic Robotics*. MIT Press, 2005.

[12] Paul E. Ceruzzi. *GPS*. MIT Press Essential Knowledge Series. Cambridge: MIT Press, 2018. ISBN: 978-0-262-53595-3.

[13] Yufei Liu, Noboru Noguchi, and Kazunobu Ishii. "Attitude Angle Estimation for Agricultural Robot Navigation Based on Sensor Fusion with a Low-Cost IMU". In: *IFAC Proceedings Volumes* 46.4 (2013), pp. 130–134.

[14] Kate Baggaley. *Why Robots Are Replacing Humans in the World's Mines*. NBC News. Dec. 21, 2017. URL: `nbcnews.com/mach/science/robots-are-replacing-humans-world-s-mines-here-s-why-ncna831631` (visited on 10/18/2021).

[15] E. Guizzo. "Three Engineers, Hundreds of Robots, One Warehouse". In: *IEEE Spectrum* 45.7 (July 2008), pp. 26–34. ISSN: 1939-9340.

[16] *Motion Capture Systems*. Vicon. URL: `www.vicon.com` (visited on 06/21/2019).

[17] *Leica Geosystems*. URL: `leica-geosystems.com` (visited on 06/21/2019).

[18] Lu Lou and Xin Xu. "An Approach to Improving Attitude Estimation Using Sensor Fusion for Robot Navigation". In: *Procedia Engineering* 15 (2011), pp. 5601–5605. ISSN: 18777058.

[19] Xuan Vinh Ha, Cheolkeun Ha, and Jewon Lee. "Trajectory Estimation of a Tracked Mobile Robot Using the Sigma-Point Kalman Filter with an IMU and Optical Encoder". In: *Intelligent Computing Technology: 8th International Conference, ICIC 2012, Huangshan, China, July 25-29, 2012. Proceedings*. Ed.

by De-Shuang Huang et al. Berlin, Heidelberg: Springer Berlin Heidelberg, 2012, pp. 415–422. ISBN: 978-3-642-31588-6.

[20] Vibhute Akash Ajay et al. "Localization and Trajectory Tracking of an Autonomous Spherical Rolling Robot Using IMU and Odometry". In: ASME, 8 2015-08-02, V05AT08A058. ISBN: 978-0-7918-5712-0.

[21] Mary Alatise and Gerhard Hancke. "Pose Estimation of a Mobile Robot Based on Fusion of IMU Data and Vision Data Using an Extended Kalman Filter". In: *Sensors* 17.10 (Sept. 21, 2017), p. 2164. ISSN: 1424-8220.

[22] Taehee Lee, Joongyou Shin, and Dongil Cho. "Position Estimation for Mobile Robot Using In-Plane 3-Axis IMU and Active Beacon". In: *2009 IEEE International Symposium on Industrial Electronics*. 2009 IEEE International Symposium on Industrial Electronics (ISIE 2009). Seoul, South Korea: IEEE, July 2009, pp. 1956–1961. ISBN: 978-1-4244-4347-5.

[23] G. Welch and G. Bishop. "An Introduction to the Kalman Filter". In: University of North Carolina, 1995.

[24] G. Dobie et al. "A Noncontact Ultrasonic Platform for Structural Inspection". In: *IEEE Sensors Journal* 11.10 (Oct. 2011), pp. 2458–2468. ISSN: 1558-1748.

[25] L. D. Mackenzie et al. "Robotic Inspection System for Non-Destructive Evaluation (NDE) of Pipes". In: *AIP Conference Proceedings*. Review of Progress in Quantitative Non-Destructive Evaluation: Proceedings of the 35th Annual Review of Progress in Quantitative Nondestructive Evaluation. Chicago (Illinois): AIP, 2009, pp. 1687–1694.

[26] J M Farley and Mitsui Babcock. "BEST PRACTICE IN THE APPLICATION OF NDT – AN UPDATE". Renfrew, UK.

[27] Hiroyuki Fujita. "What Can MEMS Do for Robotics?" In: *Robotics Research*. Ed. by John M. Hollerbach and Daniel E. Koditschek. London: Springer, 2000, pp. 377–383. ISBN: 978-1-4471-0765-1.

[28] Pedro A. Pérez Ramírez and Ingrid Bouwer Utne. "Challenges Due to Aging Plants". In: *Process Safety Progress* 30.2 (June 1, 2011), pp. 196–199.

[29] Safe Work Australia. *Confined Spaces: Code of Practice.* Sydney, NSW: Safe Work Australia, 2014. ISBN: 978-0-642-33313-1.

[30] JPT. "Sensabot: A Safe and Cost-Effective Inspection Solution". In: *Journal of Petroleum Technology* 64.10 (Oct. 1, 2012), pp. 32–34. ISSN: 0149-2136.

[31] *Piping Inspection Code: In-Service Inspection, Rating, Repair, and Alteration of Piping Systems: API 570.* Feb. 2016.

[32] S. F. Burch et al. "M-Skip: A Quantitative Technique for the Measurement of Wall Loss in Inaccessible Components". In: *Insight-Non-Destructive Testing and Condition Monitoring* 49.4 (2007), pp. 190–194.

[33] Gordon Dobie et al. "Visual Odometry and Image Mosaicing for NDE". In: *NDT & E International* 57 (July 2013), pp. 17–25. ISSN: 09638695.

[34] Peter Hansen et al. "Visual Mapping for Natural Gas Pipe Inspection". In: *The International Journal of Robotics Research* 34.4-5 (Apr. 1, 2015), pp. 532–558. ISSN: 0278-3649.

[35] Harutoshi Ogai and Bishakh Bhattacharya. *Pipe Inspection Robots for Structural Health and Condition Monitoring.* Vol. 89. Intelligent Systems, Control and Automation: Science and Engineering. New Delhi: Springer India, 2018. ISBN: 978-81-322-3749-5 978-81-322-3751-8.

[36] Thomas Ying-Jeh Chen, Seth David Guikema, and Craig Michael Daly. "Optimal Pipe Inspection Paths Considering Inspection Tool Limitations". In: *Reliability Engineering & System Safety* 181 (Jan. 2019), pp. 156–166. ISSN: 09518320.

[37] B.B.V.L. Deepak, M.V.A. Raju Bahubalendruni, and B.B. Biswal. "Development of In-Pipe Robots for Inspection and Cleaning Tasks: Survey, Classification and Comparison". In: *International Journal of Intelligent Unmanned Systems* 4.3 (July 4, 2016), pp. 182–210. ISSN: 2049-6427.

[38] *Pipeline Corrosion and Cracking and the Associated Calibration Considerations for Same Side Sizing Applications.* URL: https://www.ndt.net/article/v07n07/ginzel_r/ginzel_r.htm (visited on 03/04/2021).

[39] Hatem Mostafa Elwalwal, Shahruddin Bin Hj. Mahzan, and Ahmed N Abdalla. "Neural-Fuzzy Model Based Steel Pipeline Multiple Cracks Classification". In:

Journal of Physics: Conference Series 914 (Oct. 2017), pp. 12–18. ISSN: 1742-6588, 1742-6596.

[40]   Linxiao Yu. "Understanding and Improving Ultrasonic Inspection of Jet-Engine Titanium Alloy". Doctor of Philosophy. Ames: Iowa State University, Digital Repository, 2004, p. 6091411.

[41]   Jérôme Combaniere et al. "Interaction Between SH0 Guided Waves and Tilted Surface-Breaking Cracks in Plates". In: *IEEE Transactions on Ultrasonics, Ferroelectrics, and Frequency Control* 66.1 (Jan. 2019), pp. 119–128. ISSN: 1525-8955.

[42]   Noé Rodríguez-Olivares et al. "Improvement of Ultrasonic Pulse Generator for Automatic Pipeline Inspection". In: *Sensors* 18.9 (Sept. 5, 2018), pp. 295–317. ISSN: 1424-8220.

[43]   Hong Quang Pham et al. "Highly Sensitive Planar Hall Magnetoresistive Sensor for Magnetic Flux Leakage Pipeline Inspection". In: *IEEE Transactions on Magnetics* 54.6 (June 2018), pp. 1–5. ISSN: 1941-0069.

[44]   *ROSEN*. URL: https://www.rosen-group.com/global.html (visited on 12/27/2020).

[45]   P. Raczyński and K. Warnke. "Ultrasonic Diagnostics of Main Pipelines". In: *Advances in Materials Science* 17.4 (2017), pp. 37–54. ISSN: 17302439.

[46]   Pedro Neto, J. Norberto Pires, and Anonio Paulo Moreira. "3-D Position Estimation from Inertial Sensing: Minimizing the Error from the Process of Double Integration of Accelerations". In: *IECON 2013 - 39th Annual Conference of the IEEE Industrial Electronics Society*. IECON 2013 - 39th Annual Conference of the IEEE Industrial Electronics Society. Vienna, Austria: IEEE, Nov. 2013, pp. 4026–4031. ISBN: 978-1-4799-0224-8.

[47]   Rory Hampson, Gordon Dobie, and Graeme West. "Elasticity Measurement of Soft Tissues Using Hybrid Tactile and MARG-Based Displacement Sensor Systems". In: *IEEE Sensors Journal* 19.22 (Nov. 2019), pp. 10262–10270. ISSN: 1558-1748.

[48] Roland Siegwart, Illah Reza Nourbakhsh, and Davide Scaramuzza. *Introduction to Autonomous Mobile Robots*. 2. ed. Intelligent Robotics and Autonomous Agents. Cambridge, Mass.: MIT Press, 2011. ISBN: 978-0-262-01535-6.

[49] Hugh Durrant-Whyte and Tim Bailey. "Simultaneous Localisation and Mapping (SLAM): Part I The Essential Algorithms". 2020.

[50] Tomislav Kos, Ivan Markezic, and Josip Pokrajcic. "Effects of Multipath Reception on GPS Positioning Performance". In: *Proceedings ELMAR-2010*. Proceedings ELMAR-2010. Sept. 2010, pp. 399–402.

[51] Matjaž Mihelj et al. "Mobile Robots". In: *Robotics*. Cham: Springer International Publishing, 2019, pp. 189–208. ISBN: 978-3-319-72910-7 978-3-319-72911-4.

[52] Matjaž Mihelj et al. "Robot Sensors". In: *Robotics*. Cham: Springer International Publishing, 2019, pp. 85–105. ISBN: 978-3-319-72910-7 978-3-319-72911-4.

[53] J. Borenstein et al. *Mobile Robot Positioning – Sensors and Techniques*.

[54] Johann Borenstein and Liqiang Feng. *UMBmark: A Benchmark Test for Measuring Odometry Errors in Mobile Robots*. 1995.

[55] Gordon Dobie. "Ultrasonic Sensor Platforms for Non-Destructive Evaluation". University of Strathclyde, 2010. 308 pp.

[56] *Marvelmind Robotics*. Precise (±2cm) Indoor Positioning and Navigation - Marvelmind Robotics. URL: https://marvelmind.com/ (visited on 12/27/2020).

[57] *Pozyx*. Pozyx NV. URL: https://www.pozyx.io (visited on 12/27/2020).

[58] Tommaso Pardi et al. "Path Planning for Mobile Manipulator Robots under Non-Holonomic and Task Constraints". In: *2020 IEEE/RSJ International Conference on Intelligent Robots and Systems (IROS)*. 2020 IEEE/RSJ International Conference on Intelligent Robots and Systems (IROS). Oct. 2020, pp. 6749–6756.

[59] Sami Atiya and Greg Hager. "Real-Time Vision-Based Robot Localization". In: *Technical Reports (CIS)* (Oct. 1990), p. 23.

[60] Paulo Alves, Hugo Costelha, and Carlos Neves. "Localization and Navigation of a Mobile Robot in an Office-like Environment". In: *2013 13th International Conference on Autonomous Robot Systems*. 2013 13th International Conference

on Autonomous Robot Systems (Robotica). Lisbon, Portugal: IEEE, Apr. 2013, pp. 1–6. ISBN: 978-1-4799-1247-6 978-1-4799-1246-9.

[61]   Roman Szewczyk, Cezary Zieliński, and Małgorzata Kaliczyńska, eds. *Progress in Automation, Robotics and Measuring Techniques.* Vol. 351. Advances in Intelligent Systems and Computing. Cham: Springer International Publishing, 2015. ISBN: 978-3-319-15846-4 978-3-319-15847-1.

[62]   Matt Simon. *Your First Look Inside Amazon's Robot Warehouse of Tomorrow.* Wired. URL: `https://www.wired.com/story/amazon-warehouse-robots/` (visited on 05/10/2021).

[63]   *Spot — Boston Dynamics.* URL: `https://www.bostondynamics.com/spot` (visited on 05/10/2021).

[64]   Danda Pani Paudel et al. "2D–3D Synchronous/Asynchronous Camera Fusion for Visual Odometry". In: *Autonomous Robots* 43.1 (Jan. 2019), pp. 21–35. ISSN: 0929-5593, 1573-7527.

[65]   Benjamin Dutton and Elbert S. Maloney. *Dutton's Navigation & Piloting.* Naval Institute Press, 1978. 968 pp. ISBN: 978-0-87021-164-5.

[66]   D.M. Helmick, Yang Cheng, and S.I. Roumeliotis. "Path Following Using Visual Odometry for a Mars Rover in High-Slip Environments". In: *2004 IEEE Aerospace Conference Proceedings (IEEE Cat. No.04TH8720).* 2004 IEEE Aerospace Conference Proceedings (IEEE Cat. No.04TH8720). Vol. 2. Big Sky, MT, USA: IEEE, 2004, pp. 772–789. ISBN: 978-0-7803-8155-1.

[67]   Manon Kok, Jeroen D. Hol, and Thomas B. Schön. "Using Inertial Sensors for Position and Orientation Estimation". In: *Foundations and Trends in Signal Processing,* 11.1-2 (4 2017-04-20), pp. 1–153.

[68]   Yun Xiaoping, E.R. Bachmann, and R.B. McGhee. "A Simplified Quaternion-Based Algorithm for Orientation Estimation From Earth Gravity and Magnetic Field Measurements". In: *IEEE Transactions on Instrumentation and Measurement* 57.3 (Mar. 2008–3), pp. 638–650. ISSN: 0018-9456, 1557-9662.

[69] Seong-hoon Won et al. "A Quaternion-Based Tilt Angle Correction Method for a Hand-Held Device Using an Inertial Measurement Unit". In: IEEE, Nov. 2008–11, pp. 2971–2975. ISBN: 978-1-4244-1767-4.

[70] Seungkeun Cho, Jaehyun Park, and Jangmyung Lee. "A Dynamic Localization Algorithm for a High-Speed Mobile Robot Using Indoor GPS". In: *Robotica* 30.04 (July 2012), pp. 681–690. ISSN: 0263-5747, 1469-8668.

[71] Lu Lou et al. "Sensor Fusion-Based Attitude Estimation Using Low-Cost MEMS-IMU for Mobile Robot Navigation". In: *2011 6th IEEE Joint International Information Technology and Artificial Intelligence Conference.* 2011 6th IEEE Joint International Information Technology and Artificial Intelligence Conference (ITAIC). Chongqing, China: IEEE, Aug. 2011, pp. 465–468. ISBN: 978-1-4244-8622-9.

[72] Bin Liu, Shi Cheng, and Yuhui Shi. "Particle Filter Optimization: A Brief Introduction". In: *Advances in Swarm Intelligence.* Ed. by Ying Tan, Yuhui Shi, and Ben Niu. Lecture Notes in Computer Science. Springer International Publishing, 2016, pp. 95–104. ISBN: 978-3-319-41000-5.

[73] Ryan S. McGinnis and Noel C. Perkins. "A Highly Miniaturized, Wireless Inertial Measurement Unit for Characterizing the Dynamics of Pitched Baseballs and Softballs". In: *Sensors* 12.9 (Aug. 29, 2012), pp. 11933–11945. ISSN: 1424-8220.

[74] Charles Norman MacLeod. "Considerations for Automated NDE Applications". University of Strathclyde.

[75] Manuel F. Silva, Ramiro S. Barbosa, and António L. C. Oliveira. "Climbing Robot for Ferromagnetic Surfaces with Dynamic Adjustment of the Adhesion System". In: *Journal of Robotics* 2012 (2012), pp. 1–16. ISSN: 1687-9600, 1687-9619.

[76] Wolfgang Fischer, Fabien Tâche, and Roland Siegwart. "Magnetic Wall Climbing Robot for Thin Surfaces with Specific Obstacles". In: *Field and Service Robotics.* Ed. by Christian Laugier and Roland Siegwart. Vol. 42. Springer Tracts in Advanced Robotics. Berlin, Heidelberg: Springer Berlin Heidelberg, 2008, pp. 551–561. ISBN: 978-3-540-75403-9 978-3-540-75404-6.

[77]   Markus Eich and Thomas Vogele. "Design and Control of a Lightweight Magnetic Climbing Robot for Vessel Inspection". In: *2011 19th Mediterranean Conference on Control & Automation (MED)*. Automation (MED 2011). Corfu, Greece: IEEE, June 2011, pp. 1200–1205. ISBN: 978-1-4577-0124-5.

[78]   Sangdeok Park, Hee Don Jeong, and Zhong Soo Lim. "Design of a Mobile Robot System for Automatic Integrity Evaluation of Large Size Reservoirs and Pipelines in Industrial Fields". In: *Proceedings 2003 IEEE/RSJ International Conference on Intelligent Robots and Systems (IROS 2003) (Cat. No.03CH37453)*. Proceedings 2003 IEEE/RSJ International Conference on Intelligent Robots and Systems (IROS 2003) (Cat. No.03CH37453). Vol. 3. Oct. 2003, 2618–2623 vol.3.

[79]   Olivier Kermorgant. "A Magnetic Climbing Robot to Perform Autonomous Welding in the Shipbuilding Industry". In: *Robotics and Computer-Integrated Manufacturing* 53 (Oct. 2018), pp. 178–186. ISSN: 07365845.

[80]   Haocai Huang et al. "Design and Performance Analysis of a Tracked Wall-Climbing Robot for Ship Inspection in Shipbuilding". In: *Ocean Engineering* 131 (Feb. 2017), pp. 224–230. ISSN: 00298018.

[81]   Giuk Lee et al. "High-Payload Climbing and Transitioning by Compliant Locomotion with Magnetic Adhesion". In: *Robotics and Autonomous Systems* 60.10 (Oct. 2012), pp. 1308–1316. ISSN: 09218890.

[82]   *Pulsed Eddy Current (PEC)*. URL: `https://www.eddyfi.com/en/technology/pulsed-eddy-current-pec` (visited on 06/24/2021).

[83]   *Scorpion 2 Ultrasonic Tank Shell Inspection — UT Thickness Readings*. URL: `https://www.eddyfi.com/en/product/scorpion-2` (visited on 11/25/2020).

[84]   *High Resolution, High Speed Phased Array Corrosion Mapping — RMS PA*. URL: `https://www.eddyfi.com/en/product/rms-pa-phased-array-corrosion-mapping` (visited on 11/25/2020).

[85]   *MaggHD Magnetic Crawler — High Definition Remote Visual Inspection*. URL: `https://www.eddyfi.com/en/product/magghd` (visited on 11/25/2020).

[86]   *Versatrax 50*. URL: `https://www.eddyfi.com/en/product/versatrax-50-pipe-inspection-crawler` (visited on 11/25/2020).

[87] *Versatrax 100.* URL: https://www.eddyfi.com/en/product/versatrax-100-pipe-inspection-crawler (visited on 11/25/2020).

[88] *Versatrax 150.* URL: https://www.eddyfi.com/en/product/versatrax-150-pipe-inspection-crawler (visited on 11/25/2020).

[89] viktor. *BIKE – Inspection Robotics.* URL: https://inspection-robotics.com/bike/ (visited on 11/10/2020).

[90] air. *FAST RVI HD – Inspection Robotics.* URL: https://inspection-robotics.com/fast-rvi/ (visited on 11/25/2020).

[91] *SAIR – Arabian Robotics Company.* URL: http://arabianbots.com/sair/ (visited on 11/16/2020).

[92] *NAVIC 2 - Base Crawler.* JIREH Industries. URL: //www.jireh.com/products/navic-2-base-crawler/ (visited on 11/26/2020).

[93] M. Bibuli et al. "The MINOAS Project: Marine INspection rObotic Assistant System". In: *2011 19th Mediterranean Conference on Control Automation (MED).* 2011 19th Mediterranean Conference on Control Automation (MED). June 2011, pp. 1188–1193.

[94] Morteza Tabatabaeipour et al. "A Feasibility Study on Guided Wave- Based Robotic Mapping". In: *2019 IEEE International Ultrasonics Symposium (IUS).* 2019 IEEE International Ultrasonics Symposium (IUS). Glasgow, United Kingdom: IEEE, Oct. 2019, pp. 1567–1570. ISBN: 978-1-72814-596-9.

[95] Oksana Trushkevych et al. "Towards Guided Wave Robotic NDT Inspection: EMAT Size Matters". In: *2019 IEEE International Ultrasonics Symposium (IUS).* 2019 IEEE International Ultrasonics Symposium (IUS). Glasgow, United Kingdom: IEEE, Oct. 2019, pp. 104–107. ISBN: 978-1-72814-596-9.

[96] Morteza Tabatabaeipour et al. "Application of Ultrasonic Guided Waves to Robotic Occupancy Grid Mapping". In: *Mechanical Systems and Signal Processing* 163 (Jan. 15, 2022), p. 108151. ISSN: 0888-3270.

[97] Charles Norman Macleod et al. "Machining-Based Coverage Path Planning for Automated Structural Inspection". In: *IEEE Transactions on Automation*

Science and Engineering 15.1 (Jan. 2018), pp. 202–213. ISSN: 1545-5955, 1558-3783.

[98]   R. Summan et al. "Spatial Calibration of Large Volume Photogrammetry Based Metrology Systems". In: *Measurement* 68 (May 2015–5), pp. 189–200. ISSN: 02632241.

[99]   Dayi Zhang et al. "Autonomous Ultrasonic Inspection Using Unmanned Aerial Vehicle". In: *2018 IEEE International Ultrasonics Symposium (IUS)*. 2018 IEEE International Ultrasonics Symposium (IUS). Kobe: IEEE, Oct. 2018, pp. 1–4. ISBN: 978-1-5386-3425-7.

[100]   Ágoston Sipos and Péter Salvi. "Creating Good Quality Meshes from Smooth Implicit Surfaces". Workshop. Workshop. Budapest, 2021.

[101]   Steve Marschner. "Triangle Meshes". Lecture Slides (University of California San Diego). 2018.

[102]   Herbert Edelsbrunner. "Triangulations Adn Meshes in Computational Geometry". In: *Acta Numerica* (2000), pp. 1–81.

[103]   Eric W. Weisstein. *Sphere*.

[104]   P. Schatte. "Computing the Angle between Vectors". In: *Computing* 63.1 (7 1999-07-01), pp. 93–96. ISSN: 0010-485X, 1436-5057.

[105]   E Piña. "Rotations with Rodrigues' Vector". In: *European Journal of Physics* 32.5 (9 2011-09-01), pp. 1171–1178. ISSN: 0143-0807, 1361-6404.

[106]   Alexander McGregor et al. "Determining Position and Orientation of a 3-Wheel Robot on a Pipe Using an Accelerometer". In: *IEEE Sensors Journal* 20.9 (May 2020), pp. 5061–5071. ISSN: 1558-1748.

[107]   Manolis I A Lourakis. "A Brief Description of the Levenberg-Marquardt Algorithm Implemened by Levmar". Jan. 2005.

[108]   Donald W. Marquardt. "An Algorithm for Least-Squares Estimation of Nonlinear Parameters". In: *Journal of the Society for Industrial and Applied Mathematics* 11.2 (1963), pp. 431–441. ISSN: 0368-4245. JSTOR: 2098941.

[109]   Huishi Li. "CHAPTER III: Gröbner Bases and Basic Algebraic-Algorithmic Structures". In: *Noncommutative Gröbner Bases and Filtered-Graded Transfer.*

Ed. by Huishi Li. Berlin, Heidelberg: Springer Berlin Heidelberg, 2002, pp. 67–90. ISBN: 978-3-540-45765-7.

[110] Xsens. *MTi 100-Series*. URL: `https://www.xsens.com/products/mti-100-series` (visited on 10/05/2020).

[111] Charles N. MacLeod et al. "Quantifying and Improving Laser Range Data When Scanning Industrial Materials". In: *IEEE Sensors Journal* 16.22 (Nov. 2016–11), pp. 7999–8009. ISSN: 1530-437X, 1558-1748, 2379-9153.

[112] Rahul Summan. "Positioning for Mobile NDE Inspection Robots". PhD thesis. University of Strathclyde.

[113] *API 5L: Specification for Line Pipe*. Mar. 2004.

[114] Hugh H S Liu and Grantham K H Pang. "Accelerometer for Mobile Robot Positioning". In: *IEEE TRANSACTIONS ON INDUSTRY APPLICATIONS* 37.3 (2001), p. 8.

[115] V. Fox et al. "Bayesian Filtering for Location Estimation". In: *IEEE Pervasive Computing* 2.3 (July 2003), pp. 24–33. ISSN: 1558-2590.

[116] Ahmed Abdelgawad and Magdy A. Bayoumi. *Resource-Aware Data Fusion Algorithms for Wireless Sensor Networks*. Lecture Notes in Electrical Engineering v. 118. New York: Springer, 2012. 107 pp. ISBN: 978-1-4614-1349-3.

[117] *Pozyx Knowledge Center*. URL: `https://docs.pozyx.io/` (visited on 05/27/2021).

[118] Bruce Townsend. "Symmetric Triaxial Seismometers". In: *Encyclopedia of Earthquake Engineering*. Ed. by Michael Beer et al. Berlin, Heidelberg: Springer Berlin Heidelberg, 2014, pp. 1–19. ISBN: 978-3-642-36197-5.

[119] V. Graizer. "The Response to Complex Ground Motions of Seismometers with Galperin Sensor Configuration". In: *Bulletin of the Seismological Society of America* 99 (2B May 1, 2009), pp. 1366–1377. ISSN: 0037-1106.

[120] Maarten Lorenz and Stefan Lewandowski. "Ultrasonic Multi-Skip Inspection at Clamped Saddle Supports". In: 18th World Conference on Nondestructive Testing. Durban, South Africa, Apr. 2012, p. 10.

[121] T. Yano, S. Numao, and Y. Kitamura. "Development of a Self-Contained Wall Climbing Robot with Scanning Type Suction Cups". In: *Proceedings. 1998 IEEE/RSJ*

International Conference on Intelligent Robots and Systems. Innovations in Theory, Practice and Applications (Cat. No.98CH36190). Proceedings. 1998 IEEE/RSJ International Conference on Intelligent Robots and Systems. Innovations in Theory, Practice and Applications (Cat. No.98CH36190). Vol. 1. Oct. 1998, 249–254 vol.1.

[122]   A. Nishi. "A Wall Climbing Robot Using Propulsive Force of Propeller". In: *Fifth International Conference on Advanced Robotics 'Robots in Unstructured Environments.* Fifth International Conference on Advanced Robotics 'Robots in Unstructured Environments. June 1991, 320–325 vol.1.

[123]   Qiang Zhou and Xin Li. "Experimental Investigation on Climbing Robot Using Rotation-Flow Adsorption Unit". In: *Robotics and Autonomous Systems* 105 (July 2018), pp. 112–120. ISSN: 09218890.

[124]   O. Unver et al. "Geckobot: A Gecko Inspired Climbing Robot Using Elastomer Adhesives". In: *Proceedings 2006 IEEE International Conference on Robotics and Automation, 2006. ICRA 2006.* Proceedings 2006 IEEE International Conference on Robotics and Automation, 2006. ICRA 2006. May 2006, pp. 2329–2335.

[125]   Ozgur Unver and Metin Sitti. "Tankbot: A Palm-size, Tank-like Climbing Robot Using Soft Elastomer Adhesive Treads". In: *The International Journal of Robotics Research* 29.14 (Dec. 1, 2010), pp. 1761–1777. ISSN: 0278-3649.